KU Leuven

Biomedical Sciences Group

Faculty of Medicine

Department of Oncology

VUB

Department of Bioscience Engineering

Faculty of Science and Bioscience Engineering

INVESTIGATING THE ROLE OF FATTY ACID DESATURATION IN CANCER

SWETA PARIK

Supervisor KU Leuven: Prof. Sarah-Maria Fendt

Supervisor VUB: Prof. Jo Van Ginderachter

Chair public defence: Prof. Baki Topal

Jury members: Prof. Patrizia Agostinis
Prof. Massimiliano Mazzone
Prof. Olivier Feron
Prof. Nils Halberg
Prof. Joris Messens
Prof. Kiavash Movahedi

Dissertation presented in partial fulfilment of the requirements for the joint/double degree of Doctor of Biomedical Sciences (KU Leuven) and Doctor of Bioengineering Sciences (VUB)

Contents

Summary **8**

Chapter 1: Introduction **11**

1.1 Fatty acids are crucial regulators of cancer cell physiology *12*

1.2 Fatty acid uptake in cancer *15*

1.3 De novo fatty acid synthesis in cancer *17*

1.4 Fatty acid desaturation in cancer *19*

1.4.1 Fatty acid desaturation prevents SFA-induced lipotoxicity 22

1.4.2 Fatty acid desaturation dictates sensitivity to ferroptosis 25

2.0 Glioblastoma is a highly unfavorable prognosis *28*

2.1 Molecular characterization of gliomas is important for glioblastoma diagnosis *30*

2.2 Glioblastoma tumors are highly heterogeneous *32*

2.2.1 Molecular heterogeneity 32

2.2.2 Cellular heterogeneity 34

2.3 Glioblastoma tumors display a uniquely altered metabolism *37*

Chapter 2: Objectives **40**

Chapter 3: Evidence for an alternative fatty acid desaturation pathway increasing cancer cell plasticity **42**

3.1 Abstract *42*

3.2 Methods *42*

3.3 Main *58*

Chapter 4: GBM tumors are heterogeneous in their fatty acid metabolism and modulating fatty acid metabolism sensitizes cancer cells derived from recurring GBM tumors to temozolomide **75**

4.1 Abstract *75*

4.2 Introduction *75*

4.3 Methods *77*

4.4 Results *87*

4.5 Discussion *113*

Chapter 5: Conclusion and Discussion **116**

Acknowledgements, personal contribution and conflict of interest statements **121**

Author list *121*

Author Contributions *124*

Conflict of interest *125*

Scientific acknowledgements *126*

References **128**

Addendum **147**

List of Abbreviations

FA	Fatty acid
FASN	Fatty acid synthase
SCD1/5	Stearoyl coA desaturase 1/5
FADS1/2	Fatty acid desaturase 1/2
GBM	Glioblastoma
TMZ	Temozolomide
SFA	Saturated fatty acid
UFA	Unsaturated fatty acid
MUFA	Monounsaturated fatty acid
PUFA	Polyunsaturated fatty acid
EMT	Epithelial-to-mesenchymal transition
EGFR	Epidermal growth factor receptor
LPCAT	Lysophosphatidylcholine acyltransferase
PA	Phosphatidic acid
LPA	Lysophosphatidic acid
DAG	Diacylglycerol
PIP2	Phosphatidylinositol (4,5)-bisphosphate
PIP3	Phosphatidylinositol (3,4,5)-trisphosphate
PTEN	Phosphatase and tensin homolog
NAFLD	Non-alcoholic fatty liver disease
HCC	Hepatocellular carcinoma
FAO	Fatty acid oxidation
YAP	Yes Associated Protein

CPT	Carnitine palmitoyl transferase
MAGL	Monoacylglycerol lipase
FATP	Fatty acid transport protein
FABP	Fatty-acid binding protein
PGE2	Prostaglandin E2
MDSC	Myeloid-derived suppressor cell
SOAT1	Sterol-O-acyltransfearse1
PDX	Patient-derived xenograft
DNL	De novo lipogenesis
ACLY	ATP citrate lyase
ACSS	Acetyl coA synthetase
ACC	Acetyl coA carboxylase
ELOVL	Fatty acid elongase
CSC	Cancer stem cell
GSC	Glioma stem cell
MITF	Microphthalmia-associated transcription factor
COX	Cyclooxygenase
ER	Endoplasmic reticulum
UPR	Unfolded protein response
ROS	Reactive oxygen species
IRE1α	Inositol-requiring enzyme 1α
PERK	Protein kinase-like eukaryotic initiation factor 2α kinase
ATF6α	Activating transcription factor 6α
DSGL	Di-saturated glycerolipid

GPAT	Glycerol-3-phosphate acyltransferase
LXR	Liver-X receptor
CR	Calorie restriction
KD	Ketogenic diet
LD	Lipid droplet
DGAT	Diacylglycerol-O-acyltransferase
LOX	Lipoxygenase
ACSL	Acyl coA synthetase
GPX	Glutathione peroxidase
TET	Ten eleven translocation enzymes
IDH	Isocitrate dehydrogenase
2-HG	2-hydroxyglutarate
G-CIMP	Glioma CpG-island methylator phenotype
MGMT	6-O-methylguanine-DNA methyltransferase
HGG	High grade glioma
CL	Classical
MES	Mesenchymal
PN	Proneural
RTK	Receptor tyrosine kinase
OXPHOS	Oxidative phosphorylation
TME	Tumour microenvironment
SREBP	Sterol-response element binding protein
SCAP	SREBP-cleavage activating protein
BCAT	Branched chain amino acid transaminase

BCAA	Branched chain amino acid
GLS	Glutaminase
NAPRT	Nicotinate phosphoribosyltransferase
NAMPT	Nicotinamide phosphoribosyltransferase
ND	Newly diagnosed
RC	Recurrent

Summary (ENG)

Cancer is a global health concern, therefore, studies over several years have intensively investigated the specific characteristics of cancer cells, outlining several hallmarks of cancer. Metabolic reprogramming, a cellular response that aids cancer cell growth has emerged as one of these hallmarks. One aspect of metabolic reprogramming is rewiring of the fatty acid (FA) metabolic pathway in cancer cells so as to fulfill the biological requirements of the rapidly proliferating cancer cells. FAs are biological molecules composed of a carboxy terminal and a hydrocarbon chain, and aid cancer cell growth by impacting various aspects of cell physiology. Cancer cells often display elevated FA levels facilitated by an increase in *de novo* synthesis from glucose or glutamine by FA synthase (FASN) and/or uptake by FA transport proteins. Indeed, abrogation of FASN or specific FA uptake proteins limits growth of certain tumors. Intracellular saturated FAs may subsequently be elongated to longer chain FAs or desaturated by stearoyl coA desaturase (SCD), the canonical monodesaturase that converts the 16-carbon saturated FA, palmitate (16:0) to palmitoleate (16:1 n-7). Indeed, pre-clinical studies have demonstrated benefits of SCD inhibition in cancer. However, a major hindrance to their clinical translation has been that not all cancers respond to SCD targeting.

In this thesis, we uncovered that this can be attributed to an alternative palmitate monodesaturation pathway catalyzed by fatty acid desaturase 2 (FADS2) and leading to the production of the unusual FA, sapienate (16:1 n-10). We then showed that FADS2 silencing sensitized previously insensitive cells to an SCD inhibitor and markedly curbed the growth of liver tumours. Next, we extended these findings in glioblastoma (GBM), a particularly hard to treat cancer displaying high sapienate production. Current standard of care for GBM is radiation with temozolomide (TMZ) chemotherapy, despite which tumours always recur and median survival is ~17 months. We investigated the metabolic heterogeneity in GBMs and found that FASN, SCD and FADS2 expression shows intra-tumoral heterogeneity, reflecting this characteristic feature of GBM. Further, we found that intracellular palmitate accumulation synergizes with TMZ and markedly induces lipotoxic cell death in newly diagnosed and recurrent GBM cells cultured *in vitro* under physiological conditions.

Altogether, in this thesis we have uncovered a novel player in FA desaturation and our findings strongly suggest that clinical targeting of SCD and FADS2 has therapeutic potential in several cancers.

Summary (NL)

Kanker is een wereldwijd gezondheidsprobleem, daarom hebben studies over meerdere jaren intensief de specifieke kenmerken van kankercellen onderzocht, waarbij verschillende kenmerken van kanker worden geschetst. Metabole herprogrammering, een cellulaire respons die de groei van kankercellen bevordert, is naar voren gekomen als een van deze kenmerken. Een aspect van metabole herprogrammering is herbedrading van de vetzuur (FA) metabole route in kankercellen om te voldoen aan de biologische behoeften van de snel prolifererende kankercellen. VA's zijn biologische moleculen die bestaan uit een carboxyterminal en een koolwaterstofketen en helpen de groei van kankercellen door verschillende aspecten van de celfysiologie te beïnvloeden. Kankercellen vertonen vaak verhoogde FA-niveaus die worden vergemakkelijkt door een toename van de novo synthese uit glucose of glutamine door FA-synthase (FASN) en / of opname door FA-transporteiwitten. Inderdaad, abrogatie van FASN of specifieke FA-opname-eiwitten beperkt de groei van bepaalde tumoren. Intracellulair verzadigde VA's kunnen vervolgens worden verlengd tot FAs met een langere keten of worden gedesatureerd door stearoyl coA-desaturase (SCD), het canonieke monodesaturase dat de 16-koolstofverzadigde FA, palmitaat (16:0) omzet in palmitoleaat (16:1 n-7). Inderdaad, preklinische studies hebben voordelen van SCD-remming bij kanker aangetoond. Een belangrijke belemmering voor hun klinische vertaling is echter dat niet alle kankers reageren op SCD-targeting.

In dit proefschrift ontdekten we dat dit kan worden toegeschreven aan een alternatieve palmitaatmonodesaturatieroute gekatalyseerd door vetzuurdesaturase 2 (FADS2) en leidt tot de productie van de ongewone FA, sapienate (16:1 n-10). Vervolgens toonden we aan dat FADS2-uitschakeling eerder ongevoelige cellen sensibiliseerde voor een SCD-remmer en de groei van

levertumoren aanzienlijk remde. Vervolgens hebben we deze bevindingen uitgebreid in glioblastoom (GBM), een bijzonder moeilijk te behandelen kanker met een hoge sapienateproductie. De huidige zorgstandaard voor GBM is bestraling met temozolomide (TMZ) chemotherapie, ondanks dat tumoren altijd terugkeren en de mediane overleving ~ 17 maanden is. We onderzochten de metabole heterogeniteit in GBM's en vonden dat FASN-, SCD- en FADS2-expressie intra-tumorale heterogeniteit vertoont, wat dit karakteristieke kenmerk van GBM weerspiegelt. Verder vonden we dat intracellulaire palmitaataccumulatie synergetisch samenwerkt met TMZ en duidelijk lipotoxische celdood induceert in nieuw gediagnosticeerde en terugkerende GBM-cellen die in vitro onder fysiologische omstandigheden worden gekweekt.

Al met al hebben we in dit proefschrift een nieuwe speler in FA-desaturatie ontdekt en onze bevindingen suggereren sterk dat klinische targeting van SCD en FADS2 therapeutisch potentieel heeft bij verschillende kankers.

Chapter 1: Introduction

It has become abundantly clear that cancer cells rewire their metabolism, allowing them to thrive, despite major hindrances such as an unfavorable microenvironment, hypoxia, nutrient limitation and immune challenge, to name a few. FA metabolism, due to its tremendous impact on cell physiology has emerged as a crucial mediator of cancer cell survival[1]. Therefore, with our first objective, we aimed at identifying metabolic vulnerabilities in the cancer cell FA metabolic pathway.

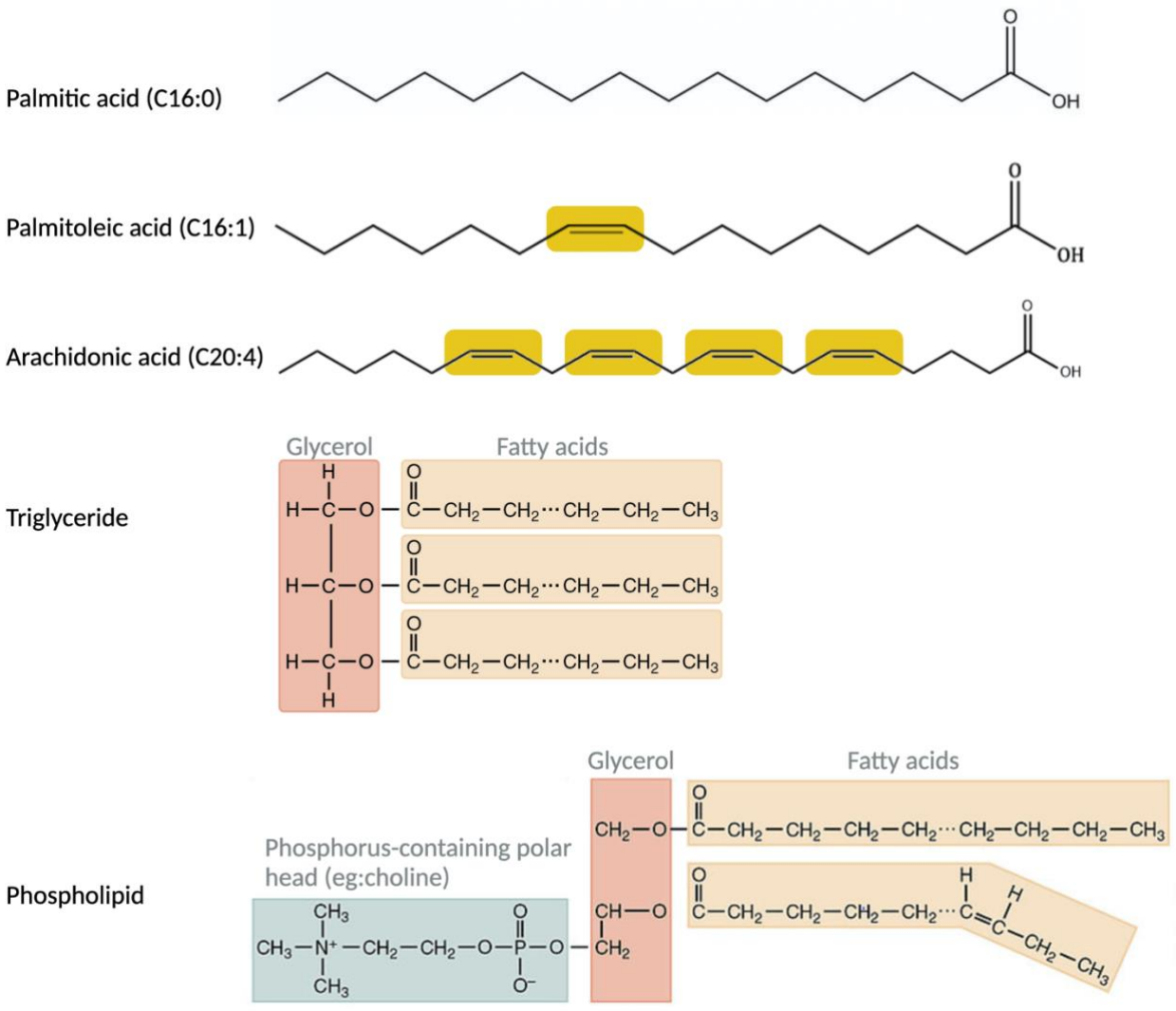

Figure 1.1: Structures of saturated and unsaturated fatty acids, triglycerides and phospholipids

1.1 Fatty acids are crucial regulators of cancer cell physiology

Fatty acids (FAs) are biological molecules composed of a terminal carboxyl group and a hydrocarbon chain and serve an extensive range of functions. Decades of research has made it clear that one cannot overstate the importance of FAs in cancer cells. The cellular fatty acid pool is comprised of saturated FAs (SFAs), monounsaturated FAs (MUFAs) and polyunsaturated FAs (PUFAs), with the main classes displayed in Figure 1.1. SFAs and MUFAs can either be taken up from the extracellular environment or be synthesized *de novo* by the concerted action of synthases, desaturases and elongases. Humans are incapable of synthesizing PUFAs, making us reliant on diet for deriving the precursors linoleic acid (18:2 n-6) and α-linolenic acid (18:2 n-3). These precursors can then be converted to multiple PUFA species by desaturases and elongases (Figure 1.2). FA chain lengths and degrees of saturation directly impact their function and the tremendous diversity in FA species makes them ideal biological regulators of cell physiology.

Research over the past several decades has highlighted several major roles of FAs, broadly classified into four critical functions. **Firstly**, fatty acids are precursors of lipids that form biological membranes, crucial for rapidly proliferating cancer cells[2]. Membrane lipids, including phospholipids, sphingolipids and sterols, are derived from fatty acids. The cancer cell membrane is far from static and is subject to constant remodeling *via* the competing action of phospholipases and acyltransferases[3]. Membrane remodeling regulates fluidity, surface protein stability and cell death pathways. In breast cancer cells, cholesterol efflux by the transmembrane efflux channel ABCA1 reduces its membrane incorporation, consequently increasing membrane fluidity. This was found to be imperative for promoting epithelial-to-mesenchymal transition (EMT) of these cells, which eventually enables metastasis[4]. In colon cancer cells, lower membrane fluidity promotes drug efflux and induces drug resistance[5]. Glioblastoma cells with epidermal growth factor receptor (EGFR) amplification display enhanced lysophosphatidylcholine acyltransferase (LPCAT1)-mediated saturated FA incorporation into the membrane, which stabilizes EGFR on the membrane[6]. Membrane lipid composition also determines cellular oxidative stress, as unsaturated FAs are prone to oxidation[7]. This crucial function will be discussed at length in later sections. **Secondly**, FAs form bioactive lipids such as phosphatidic acids (PAs),

lysophosphatidic acids (LPAs) and diacylglycerols (DAGs); that act as secondary messengers in signaling pathways[2]. Phosphorylation of membrane-bound phosphatidylinositol (4,5)-bisphosphate (PIP2) to phosphatidylinositol (3,4,5)-trisphosphate (PIP3) via PI3 kinase (PI3K) activates Akt and mTORC2 signaling, leading to downstream induction of growth and mitogenic signaling. Conversely, dephosphorylation of PIP3 to PIP2 by phosphatase and tensin homolog (PTEN) is the primary inhibitory mechanism for Akt signaling[2]. Indeed, the tumor suppressor function of PTEN has been well-described and several cancers, such as gliomas, prominently display PTEN deletions[8]. Non-alcoholic fatty liver disease (NAFLD) predisposes individuals to hepatocellular carcinoma (HCC) and is accompanied with hepatic FA accumulation[9]. Ma and colleagues showed that linoleic acid accumulates several times more than other FAs, is released by NAFLD hepatocytes and is taken up by intrahepatic CD4+ T-cells, where it induces oxidative stress, depletes CD4+ T-cells and promotes hepatocarcinogenesis[9]. Eicosanoids like prostaglandins, leukotrienes and thromboxanes are produced from the n-6 FA arachidonic acid and promote inflammation, tumorigenesis, and immune evasion[10]. **Thirdly**, fatty acids serve as post-translational protein modifiers, thereby impinging on signaling pathways that are often dysregulated in cancers. HRAS, KRAS-4A and NRAS are palmitoylated and farnesylated, the dual lipidation being necessary for proper membrane localization and downstream signaling[11]. In lung and prostate cancer cells, EGFR palmitoylation promotes membrane localization and ligand-independent signaling. *In vitro* inhibition of palmitoylation in these cells re-sensitized them to EGFR inhibitors[12]. **Finally**, FAs serve as energy storage molecules given that their oxidation in mitochondria is very energy efficient. Paradoxically, several cancers simultaneously carry out FAO and synthesis, a seemingly futile cycle that has been described to aid cancer growth[13]. Fatty acid oxidation (FAO) has been shown to support growth of prostate cancer, gliomas and triple-negative breast cancer and its inhibition reduced growth of several cancers as well as metastases[14–16]. In a recent study, Lee and colleagues demonstrated that lymph node metastasis is facilitated by Yes Associated Protein (YAP)-dependent elevation of FAO and pharmacological inhibition of FAO using the carnitine palmitoyl transferase (CPT) inhibitor, etomoxir, prevented lymph node metastases in mice[17]. Further, monoacylglycerol lipase (MAGL), that mobilizes

stored FA esters, is upregulated in several cancers and its pharmacological inhibition suppressed the growth of ovarian cancer and melanoma in pre-clinical models[18].

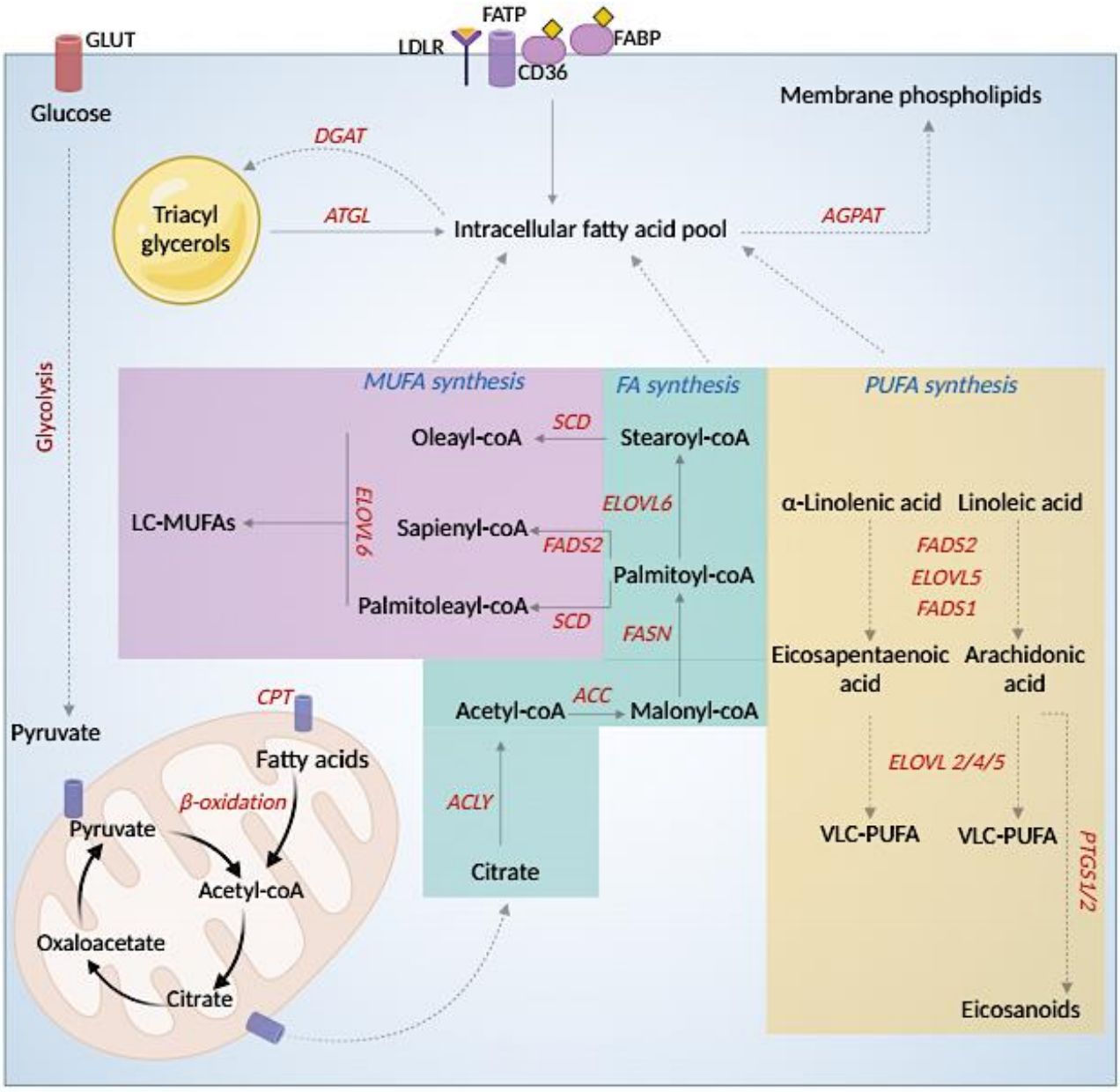

Figure 1.2: Brief overview of FA metabolism pathway

The intracellular FA pool is composed of saturated, monounsaturated and polyunsaturated FAs. Saturated and monounsaturated FAs may either be taken up from the extracellular environment by fatty acid transport proteins or synthesized *de novo* from glucose or glutamine derived citrate. Mitochondrial citrate

may be shuttled to the cytosol where ACLY regenerates acetyl coA, which is carboxylated to malonyl coA via ACC. Serial condensation of malonyl coA and acetyl coA via FASN produces the 16-carbon saturated FA, palmitate. Palmitate can then either be elongated to stearate by ELOVL6 or desaturated to palmitoleate by SCD, or sapienate by FADS2. Palmitoleate and sapienate may further be elongated to long chain-MUFAs via ELOV6. n-3 and n-6 PUFAs are synthesized by the concerted action of FADS2, FADS1 and multiple elongases from exogenously derived linoleic and α-linolenic acids. FADS2 downstream product ω-6 arachidonic acid is a precursor for eicosanoid synthesis. In periods of abundance, FAs may be incorporated into membrane phospholipids or stored in lipid droplets as triacyclglycerols (TAGs). Conversely, metabolic stress induces breakdown of TAGS via ATGL and their eventual oxidation in mitochondria to produce ATP.

FA- fatty acid, MUFA-monounsaturated fatty acid, PUFA-polyunsaturated fatty acid, ACLY- ATP citrate lyase, ACC- acetyl coA carboxylase, FASN- fatty acid synthase, ELOVL 2/4/5/6-elongase 2/4/5/6, SCD-stearoyl coA desaturase, FADS 1/2-fatty acid desaturase 1/2, PTGS 1/2- prostaglandin-endoperoxide synthase 1/2, ATGL- adipose triglyceride lipase, DGAT- diacylglycerol acyltransferase, AGPAT- acylglycerol-3-phosphate O-acyltransferase, LDLR- low-density lipoprotein receptor, FATP- fatty acid transport protein, FABP- fatty acid binding protein.

These findings have made it clear that FAs are crucial regulators of cancer growth by impinging on multiple aspects of cell physiology. FAs can be derived either by uptake from the extracellular environment and/or synthesized *de novo* from glucose or glutamine[3]. Both uptake and synthesis pathways have been found to be dysregulated in cancers and impact cancer growth as discussed in detail below.

1.2 Fatty acid uptake in cancer

The extracellular pool of FAs consists of free FAs and FA esters derived from diet, adipose tissue and liver in healthy individuals. FAs esters can be liberated by the action of membrane-bound lipoprotein lipases or soluble phospholipase A, releasing free FAs that can then be taken up by cancer cells[3]. Cancer cells may also take up FAs released by surrounding stromal cells as has been

displayed in numerous studies[19–21]. Free FA uptake is facilitated by fatty acid translocase, CD36; fatty acid transport proteins (FATPs) and fatty-acid binding proteins (FABPs), all of which have been shown to be upregulated in cancer cells. Several large studies have focused on the role of CD36 in growth of primary tumors and metastases. CD36 promotes fatty acid uptake and growth of several cancers like HCC, gastric cancer, prostate cancer and breast cancer[22]. Watt and colleagues showed that deletion of CD36 or its blocking *via* monoclonal antibodies drastically reduces tumor growth in highly aggressive PTEN-/- prostate cancer[23]. Pascual and colleagues demonstrated that CD36-mediated FA uptake is essential for the metastasis-initiating properties of a small niche of oral carcinoma cells. Blocking CD36 significantly reduced the metastatic potential in a xenograft model of oral cancer, while high fat diet augmented it[24]. CD36 expression was further found to be associated with poor prognosis and higher metastases in many human tumors[24]. Ovarian cancer cells preferentially metastasize to the adipose-rich peritoneal activity, wherein CD36-dependent FA uptake promotes tumor growth. CD36 deletion or blocking markedly reduced ovarian cancer omental metastases in mice[25]. Further, CD36 promotes gastric and colorectal cancer metastases[26,27]. With the pre-clinical benefits of CD36 blocking antibodies, increased stress is being put on exploring these as a potential therapeutic option[28]. One must, however, keep in mind that several cancers may indeed rely on FATPs or FABPs for FA uptake, as is being highlighted by recent studies. In prostate cancer cells, FAs taken up by FABP5 activate the ligand-dependent transcription factor, PPARγ, which in turn directly induces VEGF expression and increases tumor angiogenesis[29]. Metastasizing melanoma cells uptake adipocyte-derived FAs *via* FATP1 and a pharmacological FATP inhibitor, lipofermata, reduces melanoma growth and invasion[30]. Lipofermata administration was further shown to delay growth in syngeneic models of lung carcinoma, lymphoma, colon carcinoma and pancreatic cancer. It has been shown that FATP2-mediated arachidonic acid uptake and synthesis of its downstream product prostaglandin E2 (PGE2) is essential for the immune-suppressive effect of myeloid-derived suppressor cells (MDSCs). Consequently, combinatorial treatment with lipofermata and anti-CTLA-4 antibody dramatically reduced tumor growth[31]. Further, FA transport as well as transporter preference is subject to alteration by the tumor microenvironment. In GBM tumors, hypoxia induces FABP3 and FABP7-mediated FA uptake, which are stored in lipid droplets and are mobilized upon cellular

stress. Consequently, tumors derived *via* subcutaneous injection of FABP3/7 knockdown GBM cells grew dramatically slower than those from control cells[32]. Tan and colleagues showed that resistance to platinum-based drugs in ovarian cancer cells is mediated by an increase in FABP5 and FABP (PM) mediated FA uptake. β-oxidation of these FAs produces reducing equivalents that overcome ROS stress induced by these drugs. Interestingly, combinatorial treatment of carboplatin and etomoxir (β-oxidation inhibitor) substantially reduced tumor volume in a patient-derived xenograft (PDX) ovarian cancer model, without affecting animal weight[33]. Finally, in aggressive prostate cancers, essential FA uptake and their esterification into cholesterol esters is important for growth, mediated *via* an increase in sterol-O-acyltransfearse1 (SOAT1). Knockdown of SOAT1 indeed curbs growth of prostate cancers as well as GBM[34,35].

Together, these studies have highlighted that FA uptake is a relevant regulator of tumor growth as well as metastases. This role, however, does seem to be context-dependent with different cancers showing varied preference for FA uptake proteins. Moreover, cancer cell metabolic flexibility may hinder therapeutic targeting of FA uptake. Indeed, Watt and colleagues found that CD36 depletion led to a compensatory increase in FA synthesis[23].

1.3 *De novo* fatty acid synthesis in cancer

The demonstration of FA synthesis in cancer cells in 1953 opened an entire area of investigation, which has now been extensively studied. As illustrated in Figure 1.1, DNL is initiated from cytosolic acetyl coA derived from citrate or acetate. Carbons from glucose or glutamine contribute to citrate production in the mitochondria. Mitochondrial citrate may then be exported to the cytosol where ATP citrate lyase (ACLY) re-generates acetyl coA. In some cases, acetate taken up from the microenvironment can be converted to acetyl coA *via* the action of acetyl coA synthetases 1/2 (ACSS1/2). Cytosolic acetyl coA is carboxylated to malonyl coA by the rate-limiting enzymes acetyl coA carboxylases (ACCs). Next, serial condensation of 7 molecules of malonyl coA and 1 acetyl coA *via* the multi-functional enzyme fatty acid synthase (FASN) produces the SFA, palmitate (16:0). Palmitate may then be either elongated or desaturated to produce a huge diversity of fatty acids with varied chain length and degrees of saturation[36,37].

Critical enzymes in the DNL pathway have been shown to be dysregulated in cancer. Several cancers upregulate ACLY and ACC expression, and their knockdown dramatically improves survival in tumor-bearing mice[38–44]. ACLY inhibitors are in fact highly proposed for treating hyperlipidemia and hypercholesterolemia[40], are well tolerated and their therapeutic role in cancers continues to be explored[45]. However, a growing body of literature suggests that individual treatment with an ACLY inhibitor might not be viable given that ACLY-deficient cells upregulate expression of ACSS2, affording metabolic flexibility in acetyl coA production[46]. In addition, ACSS2 or ACLY-derived acetyl coA can also be used for histone acetylation[47,48], which translates into widespread gene expression changes. More recently, pharmacological inhibitors of ACC are being explored and have been shown to reduce the growth of hepatocellular carcinoma and non-small cell lung carcinoma (NSCLC) when administered alone or in combination with standard of care chemotherapy[49,50].

Fatty acid synthase (FASN) is upregulated in several cancers and increased expression is prognostic of poor survival[51]. In prostate cancer, FASN-derived palmitate post-translationally modifies Wnt by palmitoylation, leading to activation of this pathway and aiding growth of cancer cells[52]. FASN also protects cancer cells from genotoxic stress by promoting DNA repair mechanism[53]. FASN inhibitors reduce growth of several cancers and have long been proposed as a therapeutic option. Early stage FASN inhibitors orlistat, C75 and cerulenin curbed tumor growth in several studies. However, their clinical implementation is hindered due to side effects such as poor bio-availability, low metabolic stability and dramatic weight loss[37,54]. New generation inhibitors have now been developed and are being studied[2,55]. TVB-2640, has shown prolonged stable disease[56] and is under phase 2 clinical trial in combination with trastuzumab and paclitaxel, in late stage HER2+ breast cancers (NCT03179904). Cancer cell metabolic flexibility, however, may impinge on the therapeutic targeting of FASN. Treatment with the FASN inhibitor, TVB-3664, increases CD36 levels and fatty acid uptake in colorectal cancer. Interestingly, dual targeting of FASN and CD36 promoted a further reduction in tumor growth[57], highlighting the importance of combinatorial treatment strategies. Additionally, FASN knockdown was shown to promote epithelial to mesenchymal transformation in cancer cells and increase distant lung metastases[58].

These findings should be considered when proposing the use of FASN inhibitors as cancer therapy.

1.4 Fatty acid desaturation in cancer

Cytosolic palmitate can either be directly utilized, elongated *via* FA elongase 6 (ELOVL6) to stearate or desaturated to palmitoleate or sapienate by ER-localized desaturases (Figure 1.2). FA desaturases introduce a double bond in the FA acyl chains to produce either monounsaturated FAs (single C=C) or polyunsaturated FAs (multiple C=C). Desaturation reactions require oxygen as a hydrogen acceptor, cytochrome b5 as an electron carrier and NADH-dependent cytochrome b5 reductase[59] (Figure 1.2). In humans, monodesaturation reactions are catalyzed by the canonical stearoyl coA desaturase 1/5 (SCD1/5) or fatty acid destaurase2 (FADS2). SCD is an ER-bound protein that introduces a double bond between carbons 9 and 10 of palmitic and stearic acids, producing palmitoleic acid (16:1 n-7) and oleic acid (18:1 n-9), respectively. Further, FADS2 may also carry out monodesaturation of palmitate to sapienate (16:1 n-10). This pathway is crucial in human sebocytes as sapienate is a major component of human sebum and was largely thought to be exclusive for sebocytes. Findings described in my thesis show that FADS2 monodesaturation activity is prevalent in several cancers and this finding has already been corroborated by other groups[60]. In humans, polydesaturation reactions are mainly catalyzed either by Δ-5 desaturase, Fatty acid destaurase1 (FADS1) that introduces a double bond between positions 5 and 6 (from the carboxy terminal) of FAs or Δ-6 desaturase, fatty acid destaurase2 (FADS2) that introduces a double bond between positions 6 and 7 (from the carboxy terminal) of FAs. The concerted action of these enzymes produces the diversity of n-3 and n-6 PUFA (Figure 1.2).

SCD expression and activity is elevated in several cancers and increased SCD expression is associated with reduced survival and increased aggressiveness[61]. Genetic and/or pharmacological depletion of SCD reduces tumor growth in clear cell renal carcinoma[62], colon cancer[63], endometrial cancer[64], prostate cancer[65] and gliomas[66,67] in pre-clinical models. SCD elevation aids several aspects of tumor growth and proliferation. MUFAs produced by SCD play a crucial role in membrane remodeling in cancer cells and its deletion reduces incorporation of

de novo synthesized MUFAs into phospholipids and increases incorporation of exogenous MUFAs as well as PUFAs into membrane[68,69]. In breast and prostate cancer cells, depleting SCD reduced MUFA-cardiolipin (a unique phospholipid localized to the inner mitochondrial membrane), leading to the release of cytochrome c and apoptosis. This effect was reversed by exogenous supplementation of oleic acid[70]. Indeed, inducible knockdown of SCD in orthotopic prostate tumors reduced tumor growth and markedly prolonged survival in mice[71]. In lung cancer cells, SCD downregulation perturbs the plasma membrane mobility and reduces EGFR signaling[72]. More recently, SCD downregulation and increased levels of saturated membrane phospholipids have been shown to be important for the therapeutic effect of the EGFR inhibitor, gefitinib, in NSCLC[73].

Further, SCD regulates cancer cell growth by interacting with diverse growth signaling pathways, that are dysregulated in cancer[74]. SCD inhibition downregulates EGFR signaling, PI3k/Akt signaling, Notch signaling, GSK-3β signaling and TORC1 signaling [74–76]. Wnt proteins, which play a crucial role in cell growth, are post-translationally modified by the SCD product palmitoleate by porcupine acyltransferase and this is required for activation of Wnt signaling[77]. In HCC stem cells, SCD inhibition reduced Wnt signaling, attenuated stem cell self-renewal and prolonged tumorigenesis in mice[78]. The implications of this in other cancers is yet to be studied.

In several cancers, increased SCD has also been found in cancer stem cells where it maintains their properties of self-renewal and proliferation[79–85]. Ovarian cancer stem cells display increased levels of unsaturated lipids. Inhibition of SCD or FADS2 in these cells reduces stemness and tumorigenic potential of ovarian CSCs, an effect that is dependent on activation of the NF-kB pathway[86]. A screen of 141 compounds in glioma stem cells (GSCs) identified that SCD inhibition has a huge negative impact on GSC proliferation[87]. In a follow up study, the authors went on to show that shRNA-mediated knockdown of SCD in GSCs hampers tumor initiation *in vivo*. Further, administration of an SCD inhibitor dramatically reduced tumor size and prolonged survival[66]. Using *in vitro* GSC culture, it was then shown that upregulation of SCD in GSCs is required to prevent accumulation of toxic saturated fatty acids. In its absence, this protective effect is lost, and cells acquire ER stress and DNA damage[66].

Further, elevation of SCD has also been implicated in metastasis[74,88,89] and is often linked with the tumor microenvironment. Cathepsin B, secreted by lung fibroblasts, induces SCD expression in melanoma cells metastasizing to the lungs, accompanied by an increase in MUFA-to-SFA ratio[90]. SCD inhibition in mice significantly reduced metastasis and lower SCD expression is correlated with higher disease-free survival in skin cutaneous melanoma, uveal melanoma, kidney renal clear cell carcinoma, pancreatic adenocarcinoma and thymoma[89]. On the contrary, SCD inhibition was shown to promote melanoma lung metastases. Microphthalmia-associated transcription factor (MITF) is a hallmark of the proliferative phenotype in melanoma. Recently, it was shown that MITF directly increases SCD expression in proliferative melanoma cells. $MITF^{low}$ cells, on the other hand, have reduced SCD levels and better invasive potential. Pharmacological inhibition of SCD *in vivo* reduced growth of primary melanoma tumors but potentiated lung metastases[91]. Therefore, more examination is required to address the role of SCD in metastases, which may very likely be cancer-specific.

Based on these studies, targeted inhibition of SCD has been explored as a therapeutic option[61,74]. Targeted SCD inhibitors, CAY10566, A939572, and MF-438 have shown significant benefits in pre-clinical models, but human studies are lacking[92]. MK-8245, an SCD inhibitor proposed for dyslipidemia, has shown no adverse effects in a phase I clinical trial[93]. Perhaps such compounds can be translated and utilized for targeting cancers. A main concern with SCD inhibition in murine models is that it causes eye dryness, hair loss, and skin dryness, leading to cold-induced hypothermia[92]. Recently, metabolically activated prodrugs have been shown to hamper tumor growth while circumventing these effects[61,94]. However, it is known that while palmitoleate is the major component of sebum in mice, sapienate is rather enriched in human sebum[95]. It is, therefore, conceivable that these effects might be murine-specific. A bigger hindrance in its therapeutic targeting is the observation that not all cancers are sensitive to SCD inhibition[96], exposing a metabolic flexibility in cancers. Findings described in this thesis show that insensitivity to SCD inhibition can be attributed to FADS2-mediated sapienate production and dual targeting of SCD and FADS2 dramatically curbed tumor growth.

Unlike SCD, there are far fewer studies addressing the role of FADS2 in cancers and the few existing studies have not determined whether the observed effects can be owed to decreased

sapienate or PUFA production. Nevertheless, pharmacological FADS2 inhibition with SC26196 has been shown to reduce growth of colon cancer xenografts[97], melanoma and lung cancer[98] and glioblastoma[99]. Further, Wang and colleagues reported that FADS2 inhibition synergized with radiotherapy to reduce growth of GBM xenografts[100]. A subsequent study showed that MITF-low invasive melanoma cells show elevated FADS2-mediated sapienate production which influences membrane fluidity to control invasion. FADS2 inhibition in melanoma cells was shown to reduce melanoma metastases[101]. In combination with the SCD study described prior, it seems that phenotype switching from proliferation to invasion in melanoma is accompanied by a switch from palmitoleate to sapienate production, with MITF being a potential master regulator. Future studies addressing these opposing roles will certainly be very interesting.

Finally, PUFAs produced by FADS2 activity also have a major role in cancers. Eicosanoids, including prostaglandins, leukotrienes and thromboxanes are produced from the FADS2 product arachidonic acid and promote an immune-suppressive inflammatory microenvironment[102]. The rate-limiting step in eicosanoid synthesis is catalyzed by cyclooxygenase 1 (COX1)/PTGS1 and cyclooxygenase2 (COX2)/PTGS2, which are elevated in several cancers. Mice with a genetic deficiency of *Cox2* show abrogated growth of K-ras-induced lung cancers[103], HER2/neu-induced mammary tumorigenesis[104] and intestinal tumors[105]. Further, PGE2 administration itself accelerates intestinal and colon tumor growth *via* activating Ras-MAPK and β-catenin signaling, respectively[106,107]. Finally, PUFAs, when incorporated into biological membranes, modulate membrane fluidity and are uniquely susceptible to oxidative damage[7].

Together, the findings described above illustrate that SCD and FADS2 both play an undeniably critical function in cancers. Emerging studies indicate that cells exert consistent efforts to maintain a saturated-to-unsaturated FA balance that allows cell survival and is discussed in detail below.

1.4.1 Fatty acid desaturation prevents SFA-induced lipotoxicity

It has long been known that accumulation of saturated FAs (SFAs) such as palmitate induces cellular stress and apoptosis. This toxic accumulation of free fatty acids in cells which occurs when they are in excess and cannot be mobilized for an alternative fate is termed lipotoxicity. (Figure

1.3). In healthy individuals, excess fatty acids are stored in and mobilized from adipose tissue, while obesity may lead to lipotoxic FA accumulation in tissues such as pancreatic beta-cells, hepatocytes, skeletal muscle cells and cardiomyocytes[108]. Indeed, plasma free FAs are elevated in obese individuals and markedly accumulate in pancreatic β-cells, impairing insulin secretion and promoting metabolic dysfunction. Further, ectopic accumulation of free FAs in heart and liver promotes obesity-associated organ dysfunction. Failure to adapt to the FA overload ultimately induces cell death and is characterized by severe cellular dysfunctions such as: ER stress, ROS accumulation, inflammation and autophagy[109].

A major pathway that brings about this cytotoxic effect is ER stress, which in turn elicits the unfolded protein response (UPR). The ER stress response involves downstream activation of three transmembrane sensors: inositol-requiring enzyme 1α (IRE1α), protein kinase-like eukaryotic initiation factor 2α kinase (PERK) and activating transcription factor 6α (ATF6α)[108]. Intracellular accumulation of SFAs does indeed induce activation of these pathways and their downstream signaling. Importantly, the lipotoxic effects of SFAs can be rescued by supplementation of unsaturated FAs (UFAs), while further increase in SFAs exacerbate the effect[108,110,111]. This asserts that a balance of SFA/UFA, rather than absolute FA amounts, dictates lipotoxicity.

However, the cellular response to SFA-induced lipotoxicity in cancer cells is not fully understood. A global lipidome and transcriptome profiling study has shed further light on this. The authors reported that the major lipidomic effect of palmitate supplementation in leukemic cells is the accumulation of di-saturated glycerolipids (DSGLs)[112]. Knockdown of glycerol-3-phosphate acyltransferase4 (GPAT4), involved in the production of DSGLs from palmitate, prevented lipotoxicity. They then went on to describe that deletion of RNF213, an understudied E3 ubiquitin ligase, was also able to rescue palmitate-induced lipotoxicity *via* the downregulation of NF-κB downstream genes[112]. This implies that lipotoxicity may rather be a global response, impinging on several cellular pathways to induce cell death in a concerted manner.

As discussed previously, cancer cells actively acquire and synthesize FAs which could potentially induce lipotoxicity, unless sequestered within lipid droplets or desaturated[108]. One may propose

that an essential requirement for SCD and FADS2 elevation in cancer cells is to ensure that toxic SFAs are quickly channeled towards the production of non-toxic UFAs. Inhibition of SCD or FADS2 may thus lead to accumulation of SFAs, substrates for these enzymes, in cancer cells and induce lipotoxic cell death. Two recent studies have reinforced this concept and revealed the therapeutic potential of lipotoxicity. Rudalska and colleagues propose induced lipotoxicity, a novel therapeutic regimen composed of combinatorial treatment with a Liver-X receptor (LXR) agonist and Raf1 inhibitor, for hepatocellular carcinoma (HCC)[113]. LXR, a nuclear receptor and transcription factor, is well known as a lipogenic activator [114] and the authors found that Raf1, a key kinase in the Ras–MEK–ERK pathway, binds and stabilizes SCD. Pharmacological LXR agonist and Raf1 inhibitor administration thus leads to increased FA synthesis that cannot be countered by desaturation, consequently increasing the SFA-to-MUFA ratio[113]. This "induced lipotoxicity" regimen was able to overcome sorafenib (multi-kinase inhibitor) resistance and improved survival in multiple pre-clinical HCC models, without significant side effects[113]. Another study by Lien and colleagues demonstrated that the anti-tumor effect of low glycemic diet regimens, namely calorie restriction (CR) and ketogenic diet (KD), is dictated by the UFA-to-MUFA balance[115]. In a PDAC allograft model, only CR and not KD reduced tumor growth. The authors discovered that while both diets inhibit SCD activity in tumors, only CR reduces extracellular fatty acid levels, mainly PUFAs. Consequently, a UFA deficit in cells cannot be compensated for by uptake and the resultant increase in the SFA-to-UFA ratio causes lipotoxicity. The authors also showed that feeding a high fat-CR diet (palm oil-CR) or ectopic SCD expression in tumors of CR-fed mice partially negated the beneficial effects of CR[115]. These studies provide evidence that lipotoxicity induction can have tremendous benefits in many cancers. Further, they suggest that both pharmacological intervention and dietary manipulation may be a plausible method of clinical application of this regimen. One may argue, however, that therapeutic benefits of such regimens might be circumvented owing to cancer cell metabolic flexibility. Toxic effects of excess fatty acids can be avoided by storing the surplus in lipid droplets as triglycerides. Several cancers indeed show increased accumulation of FA esters in lipid droplets (LDs). Abrogation of diacylglycerol-O-acyltransferase1 (DGAT1), which is required for triglyceride synthesis, has been shown to promote cancer cell lipotoxicity[116–118]. Thus, it would be interesting to explore if a

combination of lipotoxicity inducers and DGAT1 inhibition has an additive repressive effect on tumor growth.

1.4.2 Fatty acid desaturation dictates sensitivity to ferroptosis

Ferroptosis is an iron-mediated cell death that was identified in 2012 and is now recognized in several cancers. Novel aspects of this unique cell death mechanism continue to be exposed[7]. A recent study identified that IFN-γ, secreted by immunotherapy-activated cytotoxic CD8+ T-cells, induces ferroptosis in cancer cells and thus plays a crucial role in cancer immunotherapy[119]. Ferroptosis is initiated by an overabundance of reactive oxygen species (ROS) that then oxidize membrane-associated lipids *via* lipoxygenases (LOXs) (Figure 1.3). Importantly, oxidation can take place only at double bonds, making unsaturated fatty acids selectively sensitive to peroxidation. While theoretically both MUFAs and PUFAs may undergo such oxidation, MS-based analyses demonstrated that only phospholipid-bound PUFAs, most often adrenic (22:4) and arachidonic (20:4) acids, are oxidized upon induction of ferroptosis[120]. Indeed, acyl coA synthetase 4 (ACLS4), an enzyme that selectively incorporates PUFAs into membrane lipids, is an important regulator of ferroptosis and its genetic ablation markedly hampers ferroptosis[120,121]. Conversely, lipid ROS can be scavenged by glutathione peroxidase 4 (GPX4) and its genetic ablation or pharmacological inhibition *via* RSL3 treatment dramatically induces ferroptosis. Finally, system Xc-, a cystine/glutamine antiporter that provides cysteine for glutathione synthesis is an important scavenger of lipid ROS, in turn regulating ferroptosis. Erastin, later identified as a system Xc- inhibitor, was initially identified in a screen of 23,550 compounds to induce death in RAS^{V12} (an oncogenic allele of HRAS) overexpressing cells but not wild type isogeneic counterparts[122]. While PUFA abundance promotes ferroptosis, MUFAs have the opposite effect, mainly due to the fact that their availability reduces PUFA incorporation into membranes. Magtanong and colleagues showed that exogenous supplementation of the MUFAs oleic acid and palmitoleic acid rescued membrane lipid peroxidation by increasing the incorporation of MUFAs in the plasma membrane, thereby preventing ferroptotic cell death in cancer cells[123]. Further, *in vivo* SCD inhibition in ovarian cancer, breast cancer and prostate cancer induces ferroptosis, which can be rescued by MUFAs or the ectopic expression of SCD[124,125]. It is more complicated to unravel the role of FADS2 in ferroptosis, owing to its role in both MUFA and

PUFA production. A few reports have shown that, similar to SCD, FADS2 inhibition promotes ferroptosis in cancer cells[126,127]. Perhaps this is context-dependent and is dictated by the relative engagement of FADS2 in MUFA versus PUFA desaturation pathways. We have observed that cancer cells display a wide range of FADS2-mediated sapienate production[60,128]. It is conceivable that in cancers with high levels of sapienate, FADS2 may indeed have a protective role in ferroptosis while the converse may be true when PUFA production is favored. Nevertheless, it cannot be contested that the cellular MUFA/PUFA balance directly regulates ferroptosis sensitivity in cancer cells.

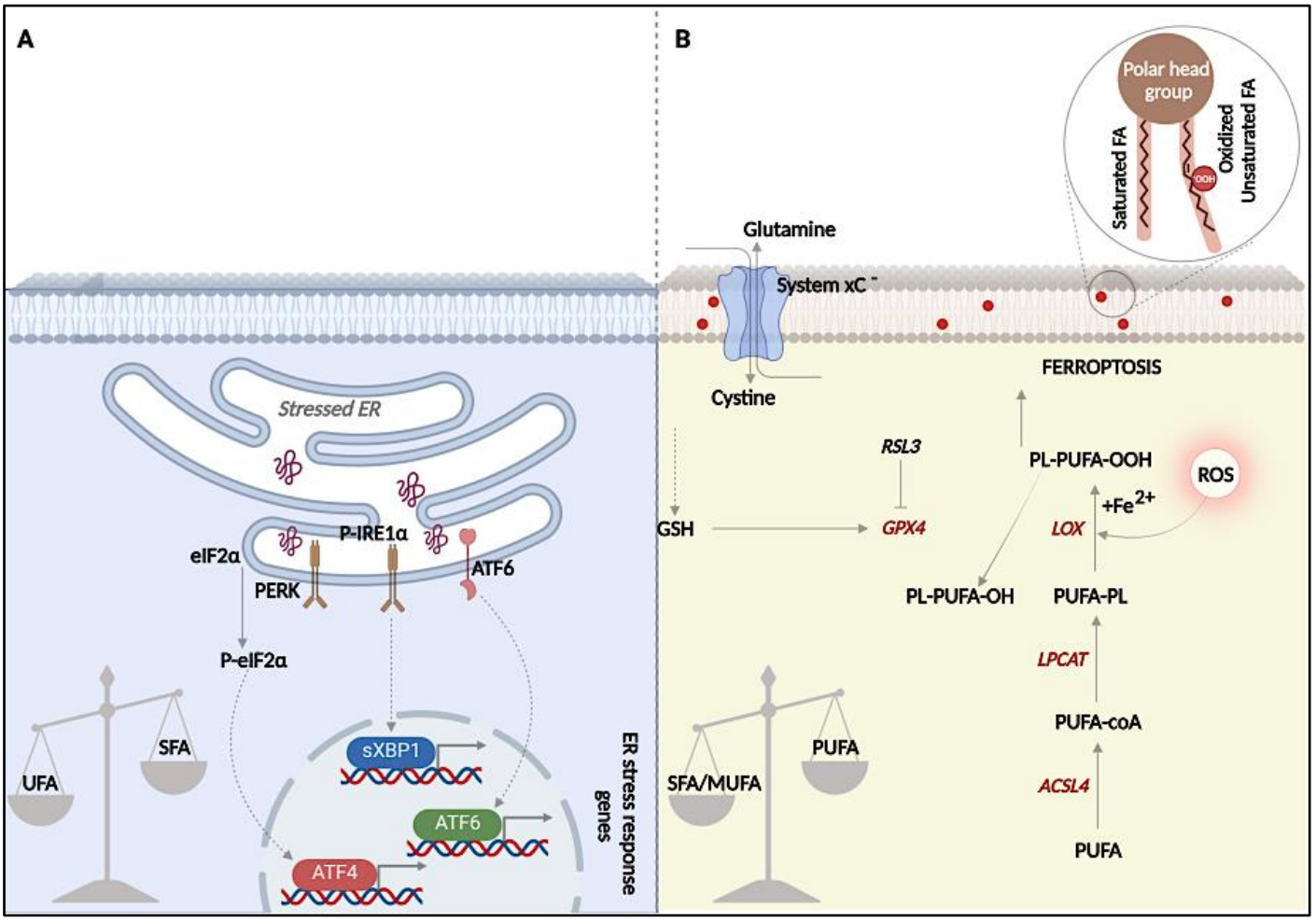

Figure 1.3: Cellular SFA-to-UFA balance regulates cell death

(A) Increased SFA-to-UFA ratio induces lipotoxic cell death. Accumulation of misfolded proteins in the ER or SFA accumulation activates the ER stress response pathway elicited by the activation of PERK, IRE1α

and ATF6α signaling. PERK phosphorylates eIF2α which stops protein translation and selectively induces transcription of ATF4 downstream genes. IRE1α promotes alternative splicing of XBP-1 and the variant sXBP1 localizes to the nucleus and also ATF6 localizes to the nucleus after undergoing Golgi processing. Together, this leads to transcription of genes that restore ER homeostasis. **(B)** Increased PUFA-to-SFA/MUFA ratio induces ferroptotic cell death. ROS induces oxidation of phospholipid-associated PUFAs mediated by LOX enzymes in an iron-catalyzed reaction. Membrane peroxidation can be scavenged by GPX4, the synthesis of which is dependent on glutathione derived from cystine taken up by the glutamine/cystine antiporter system Xc^-.

UFA-unsaturated fatty acid, SFA-saturated fatty acid, PUFA- polyunsaturated fatty acid, MUFA-monounsaturated fatty acid, eIF2α- eukaryotic translation initiation factor 2α, IRE1α- inositol-requiring enzyme 1α, PERK- protein kinase-like eukaryotic initiation factor 2α kinase, ATF6 α - activating transcription factor 6α, ATF4- activating transcription factor 4, XBP1- X-box binding protein 1, ROS-reactive oxygen species, GPX4- Glutathione peroxidase 4, ACSL4- acyl-CoA synthetase long chain family member 4, LPCAT- Lysophosphatidylcholine acyltransferase, LOX-lipoxygenase.

Interestingly, a PUFA-rich fish oil-based diet was shown to promote ferroptosis and curb hypoxic tumor growth in mice[129], highlighting the potential application of dietary interventions to induce ferroptosis. However, it must be considered that dietary supplementation of excess PUFAs can have negative effects. Excess extracellular PUFAs can, for instance, be taken up by the CD36 translocase on CD8+ T-cells, which induces ferroptosis and impairs their cytotoxic function[130–132]. Further research is thus required to unravel the systemic effect of PUFA-rich diets in the context of cancer.

In the context of these findings and our identification of sapienate production in several cancers, the clinical benefit of targeting FA desaturation is clear. Most importantly, our study demonstrated the promise of dual targeting of SCD and FADS2 in cancers that show high sapienate production, mainly liver and lung cancer. In a subsequent study from the Fendt lab, it was observed that glioblastomas display FADS2 activity[128]. In light of this, we proceeded with our next goal of addressing whether targeting FA desaturation could be potentially beneficial in the difficult to treat glioblastoma.

2.0 Glioblastoma has a highly unfavorable prognosis

Glioblastoma is the most malignant brain tumor and accounts for ~60% of all brain tumors in adults. With a median survival of 15-16 months and a 5-year survival rate of ~5%, it is an especially dismal prognosis. Despite low global incidence of 3.2/100,000 people, GBM is most devastating in terms of "years of life lost" with 20.11 years compared to 6.1 years for prostate cancer and 11.8 years for lung cancer[133]. These tumors arise from astrocytes and oligodendrocytes and may occur in patients as primary tumors arising *de novo* or develop as secondary tumors from a lower grade glioma. On diagnosis, the conventional standard of care involves maximal surgical resection, followed by concomitant chemotherapy and radiotherapy and 6 cycles of adjuvant chemotherapy. This treatment regimen, referred to as the "Stupp Protocol", remains the global standard of care for newly diagnosed GBM and utilizes temozolomide as a chemotherapeutic drug[134]. Temozolomide (TMZ) is an orally administered DNA alkylating agent that methylates purine bases at O6, N3 and N7 positions, which when unrepaired lead to DNA damage and, ultimately, cell death. Although Stupp and colleagues established that this regimen extends survival by ~2 months compared to radiotherapy alone, the median survival was still a mere 14.6 months. This can be attributed to the fact that GBMs eventually always recur within 6 months of the initial diagnosis.

Although maximal surgical resection is performed, the GBM tumor is highly aggressive, infiltrative, and vascularized, making it impossible to resect the entire tumor, therefore enabling recurrence. There is currently no standard of care for recurrent GBM and patients eventually succumb to the disease, making it urgent to explore therapeutic options for recurrent GBMs. Indeed, increased stress is now being put on the study of recurrent GBMs as previous studies have mostly focused on newly diagnosed GBMs. Only 20-30% of recurrent tumors are surgically excised and the obtained tissue is often low quality due to widespread necrosis, therefore, causing a deficit of patient samples for large-scale studies. Approximately two-thirds of recurrent GBM tumors arise within 2 cm of the initial tumor margin, indicating that GBM cells invading the tumor periphery into surrounding brain originate these tumors. One-third of the tumors occur at a distant site, far away from the initial tumor mass[135]. Initially, it was proposed that these distant recurrences were new primary GBMs, arising independent of the first tumor. This was based on

the observation that there is very little genetic similarity between these tumors. By performing clonal analysis in 22 paired newly diagnosed and recurrent GBMs, Kim and colleagues identified that distant recurrences share early-event mutations with initial tumors suggesting that they arise from GBM cells dispersed at the initial stages of disease[136]. Analysis of exome sequencing data from 10 paired newly diagnosed and recurrent GBM samples further showed a pattern of subclonal diversity upon recurrence: (i) dominant subclones that disappeared upon recurrence (ii) dominant subclones that remain dominant upon recurrence and (iii) smaller subclones that become dominant upon recurrence[137]. These studies have highlighted considerable genetic differences between paired newly diagnosed and recurrent GBM tissue, emphasizing that previous studies cannot be reliably directly translated to recurrent GBMs. Further, they highlight the need of re-sampling and re-assessing recurrent GBMs, especially those arising at a distant site.

Although there is undeniable inter-patient variation, several commonly altered genes have now been identified upon GBM recurrence. DNA-repair proteins MLH1 and MSH2 are lower expressed in recurrent GBM. Further, TMZ itself induces GBM evolution, resulting in a distinct clonal profile of recurrent GBM. A study of 114 GBM tissues showed the presence of common driver mutations as well as newly occurring mutations in recurrent GBM arising post TMZ[138].

In fact, TMZ-induced mutagenesis (via DNA alkylation) directly induces a hypermutator phenotype upon recurrence when administered in patients with low grade gliomas[139]. In contrast, in their study of 38 pair-matched newly diagnosed and recurrent gliomas, Kim *et al* identified that while low grade gliomas showed a hypermutator phenotype on recurrence, GBMs did not.

Regardless of these discrepancies, recurrence is a major hindrance in GBM treatment and there is a tremendous need for studying its therapeutic targeting.

2.1 Molecular characterization of gliomas is important for glioblastoma diagnosis

Historically, gliomas have been identified based on histopathological features of nuclear atypia, mitosis, microvascular proliferation, and necrosis and classified on a four-tier grade, Grade I-IV as per WHO 2007 guidelines. In this classification, grade IV, the most aggressive tumor with dismal prognosis was classified as glioblastoma multiforme. Several studies then identified molecular differences in gliomas that could be used as stratification and prognostic markers. As a result, 2016 WHO guidelines incorporated molecular and genomic criteria in adult diffuse glioma diagnosis. Under this classification, GBMs comprised of *IDH*-wt GBM which is highly aggressive and represents 90% of diagnosed GBMs, and *IDH*-mutated GBM that displays mutations in isocitrate dehydrogenase (IDH) genes (mostly *IDH1 R132H* point mutation) and have much better prognosis[140]. The latest revision to these guidelines in 2021 now classifies GBM as strictly IDH-wt tumors while IDH-mutated tumors are now classified as grade IV astrocytoma[141]. The updated 2021 classification scheme is displayed in Figure 1.4.

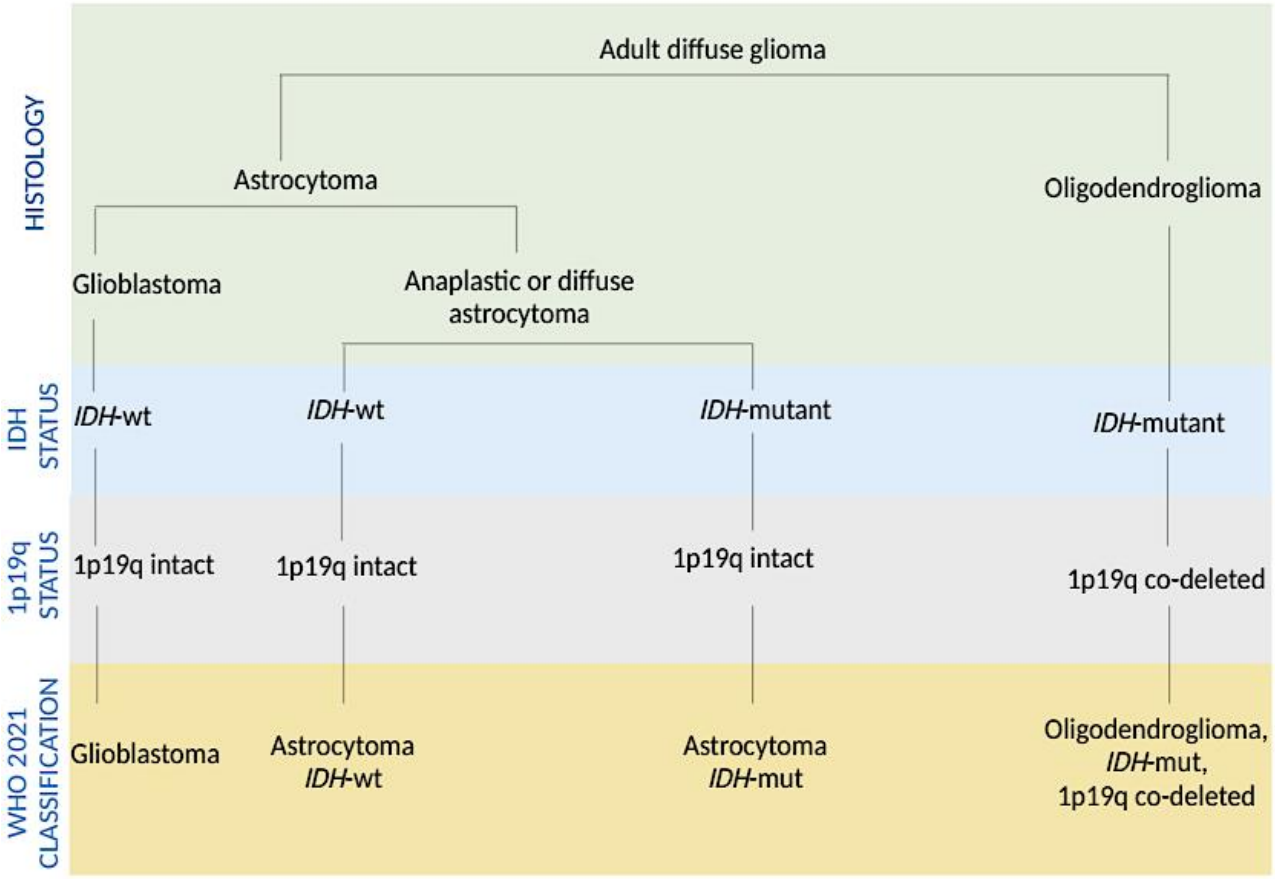

Figure 1.4: WHO 2021 classification of adult diffuse glioma

In addition to diagnosis and classification, molecular characterization has emerged as an important prognostic tool. Perhaps the most reliable marker of high-grade glioma prognosis is the IDH mutation status[140]. IDH is a TCA cycle enzyme that converts isocitrate to α-ketoglutarate (α-KG), while generating NADH. Several cancers display mutations in *IDH* genes, with *IDH1* point mutations, particularly *IDH1 R132H,* being the most prevalent in glioma[140,142], which will be referred to as IDH-mut subsequently. IDH-mut tumors produce the oncometabolite 2-hydroxyglutarate (2-HG), consuming NADPH in the process. This has major implications on cell physiology and will be discussed in detail in later sections. Clinically, patients with IDH-mut tumors have a much better prognosis[143]. Part of this can be attributed to the fact that IDH-mut tumors display a hypermethylation phenotype. α-KG acts as a co-factor for the activity of DNA methylating ten eleven translocation enzymes (TETs) and histone lysine demethylases (KDMs). In its absence, cells acquire widespread hypermethylation of CpG islands, a phenomenon called "glioma CpG-island methylator phenotype (G-CIMP). Therefore, estimation of DNA methylation has become a crucial prognostic factor as well[140]. Ceccarelli and colleagues analyzed methylation and gene expression data from 1100 glioma tissues deposited in TCGA and identified 6 distinct methylation and transcription phenotypes, LGm1-LGm6[144]. LGm1-LGm3 consist of IDH-mut tumors with LGm3 showing markedly improved survival. LGm4-LGm6 consist of IDH-wt GBMs that have the worst prognosis[144]. DNA methylation profiling is routinely performed in clinics and is a robust method for classifying tumors[145]. In particular, 6-O-methylguanine-DNA methyltransferase (MGMT) promoter methylation is a crucial prognostic marker and informs clinical decisions. MGMT is a suicide enzyme capable of directly removing the methyl group introduced by TMZ[140]. Unsurprisingly, it has been reported that MGMT expression is negatively correlated with TMZ sensitivity[146]. MGMT expression itself is dependent on CpG island methylation at its promoter with increased methylation repressing gene expression. Multiple studies have now proven that patients with higher methylation at the MGMT promoter respond better to TMZ and show a longer survival[147–150]. MGMT methylation testing has been quickly

incorporated in the clinical setting. Elderly patients (>60-65 years old) with high MGMT promoter methylation may be treated with TMZ alone, given the toxicity associated with combined TMZ and radiation. Similarly, patients presenting with low MGMT promoter methylation may be treated with radiotherapy alone[151,152].

Together, these findings have indicated that while molecular classifiers may predict prognosis and the identification of gliomas, patient prospects remain bleak. Therefore, research has been focused on identifying targetable populations and mechanisms in GBM, but no improvement in treatment regimen has been seen since the 1970s[153]. It has now become evident that the major cause of failure of targeted therapies is that the GBM tumor is extremely heterogeneous[154,155]. This makes it impossible to target all cancer cells, eventually causing recurrence.

2.2 Glioblastoma tumors are highly heterogeneous

Based on histological features and cellular organization, GBMs have long been identified as very heterogeneous tumors and referred to as glioblastoma "multiforme"[154]. Inter-patient genomic variability is widely recognized, and recurring genomic alterations are clinically assessed to classify gliomas and to enable prognosis. GBMs often carry TERT promoter mutations and copy number changes at chromosomes 7 and 10 (+7/-10)[140]. The advent of sequencing technologies enabled to take this a step further and to address molecular differences at the inter- and intra-tumoral level, as discussed below in detail.

2.2.1 Molecular heterogeneity

Using bulk gene expression analysis, early studies were restricted to addressing inter-tumoral heterogeneity. Phillips *et al*[156] and Verhaak *et* al[157] analyzed TCGA bulk gene expression data from high grade glioma (HGG) and from 200 GBM specimens, respectively, and identified 3 distinct molecular subtypes: Classical (CL), Mesenchymal (MES) and Proneural (PN). CL prominently displayed EGFR amplification, *CDKN2A* deletion and expression of stemness markers. MES samples displayed increased inflammatory markers (expression of TNF and NF-κB genes), mesenchymal markers and *NF1* deletion. PN expressed oligodendrocytic markers, increased

PDGFRA expression, *TP53* mutation and loss of heterozygosity and finally *IDH1* point mutation (primarily *IDH1R132H*). Patients with PN GBM showed most prolonged survival which can be attributed to the less aggressive IDH-mut tumors[158]. Interestingly, however, Verhaak and colleagues found that all subtypes, except PN, show improved survival in patients undergoing more intensive therapy than those undergoing less intensive therapy[157]. This hints that the PN subtype, despite having longer median survival, does not show much improvement with intensive therapy, a trend the 3 other subtypes prominently show, emphasizing the simultaneous need to study IDH-mut tumors.

Transcriptomic studies have been accompanied by DNA profiling in GBMs that highlighted common GBM-associated genomic alterations. Receptor tyrosine kinases (RTKs) are often dysregulated in glioma, with high-level amplification observed in RTKs such as EGFR (60%–70%), PDGFRA (12%–15%), and MET (5%)[159]. The identification of these alterations instigated the development of targeted therapies against these RTKs. EGFR in particular drew interest as ~30% of GBM patients express EGFRvIII, an EGFR variant with constitutively active ligand-independent activity. Unfortunately, rindopepimut, a peptide vaccine targeting this variant, did not show any benefits in a phase 3 clinical trial study (NCT01480479)[160]. It is now being revealed that the most likely cause of failure of targeted therapies in GBM is intra-tumoral heterogeneity. Snuderl *et al* analyzed the expression of three RTK genes; *MET*, *EGFR* and *PDGFRA* in primary GBM tissues and identified a mosaic expression, forming separate subsets in the tumor. Interestingly, cell subsets arising from the same parental clones displayed differential expression of these genes[161]. Subsequent studies have confirmed that EGFR and PDGFRA are indeed variably expressed within the same tumor sample[162,163]. These studies were facilitated by the advent of single-cell sequencing techniques, which also propelled deeper investigation into GBM intra-tumor heterogeneity.

Neftel and colleagues analyzed single-cell RNA sequencing (scRNA-seq) data and identified 4 GBM cell states, driving heterogeneity. These states, namely, Astrocyte (AC)-like, Neural progenitor cell (NPC)-like, Oligodendrocyte progenitor cell (OPC)-like and Mesenchymal (MES)-like resemble neurodevelopmental stages (except MES-like) with some cells existing in intermediary stages, indicating phenotypic switching within tumors[164]. More recently, Garafano

and colleagues identified 4 GBM subtypes distinguished on neurodevelopmental and metabolic parameters: neuronal, proliferative, glycolytic (GPM) and mitochondrial (MTC). GPM cells showed higher expression of glycolysis and lipid biosynthesis genes and were predominantly reliant on glycolysis, while MTC cells preferred mitochondrial OXPHOS. MTC GBMs were associated with prolonged survival, displayed higher sensitivity to radiotherapy and were selectively sensitive to OXPHOS inhibitors, hinting the usefulness of this criterium for stratification as well as identifying novel therapeutic targets. Additionally, multi-sample studies have demonstrated considerable TCGA subtype intra-tumor heterogeneity as well, with more than 1 subtype existing in the same tumor[165–167]. In fact, 63% patients show a subtype switch upon recurrence, displaying temporal heterogeneity[168]. Finally, GBMs also display epigenomic heterogeneity as shown in a recent study by Wenger and colleagues. They demonstrated that the DNA methylation pattern, a clinically relevant parameter, is highly variable within the same GBM tumor, while lower grade gliomas were more homogeneous[169,170].

These findings definitively demonstrate that GBM tumors are molecularly heterogenous at the inter- as well as intra-tumoral level. Rightly so, tumor heterogeneity is a hallmark of GBM and the biggest hurdle in its therapeutic targeting.

2.2.2 Cellular heterogeneity

GBM tumors feature a population of glioma stem cells (GSCs) that display self-renewal and tumor initiation[171,172]. GSCs showed higher tolerance to radiation and chemotherapy and increased invasive potential compared to non-stem cells[173–179]. Initial studies used CD133 as a GSC marker and showed that the proportion of CD133+ cells in tumors was correlated with poor survival in GBM patients[180,181]. Chen and colleagues generated a genetically engineered mouse glioma model by breeding *Nes-ΔTK-GFP* transgenic mice (showing GFP labelling in quiescent stem-like/nestin-positive cells) with glioma Mut7 model (*hGFAP-Cre;Nf1fl/+;P53fl/fl;Ptenfl/+*). *Mut7; Nes-ΔTK-GFP* mice developed primary GBMs, showing a population of GFP+/Ki67- quiescent cells and one of GFP-/Ki67+ cells. TMZ treatment of these mice led to the specific depletion of GFP- cells. The authors then analyzed the recurrent tumors and, using endogenous lineage tracing, demonstrated that GFP+ cells originated the recurrent tumor. Targeted deletion of these cells

prolonged survival and reduced tumor size in *Mut7; Nes-ΔTK-GFP* mice[182]. These findings proposed a model wherein apically located stem cells terminally differentiate into GBM cancer cells, leading to many efforts to target this specialized niche. This notion has now been challenged by newer studies, showing that GSCs do not resemble a specific subset of cancer cells. Chen and colleagues demonstrated that CD133- cells also displayed tumor-initiation, albeit slower than CD133+ cells, and that GBM cells exist in a spectrum of GSC properties[183]. This finding was corroborated by further studies showing that CD133- cells implanted in nude rats are capable of regenerating GBM tumors that reflect characteristic GBM heterogeneity[184]. FACS-sorted $EGFR^{High}$ and $EGFR^{low}$ GBM cells, when transplanted into separate mice, gave rise to tumors with EGFR expression heterogeneity reminiscent of the original tumor. This indicates that GBM cells exist in a dynamic state and are capable of transitioning between these states[185]. These studies challenged the original GSC model and indicated that, rather than a stable population lying at the apex of differentiation hierarchy, GSCs represent a highly dynamic cell state (Figure 1.4). Further, standard of care GBM therapy itself affects stemness. Temozolomide and radiation treatment not only selects for pre-existing GSCs, but they also lead to acquisition of GSC properties and stemness markers CD133, SOX2, Oct4, and nestin in GBMs, further exposing GSC plasticity[186,187].

Lineage tracing analysis in more recent studies has allowed the direct observation of GSC plasticity. Dirkse *et al* showed that GSCs are plastic and capable of switching between stem-like and differentiated states, subject to the tumor microenvironment[188]. scRNA sequencing analysis of GSCs from 26 patients classified these cells into 2 distinct categories: “development” and “injury-response”. “Developmental” GSCs expressed genes encoding for glial, astrocytic and neuronal precursors (*OLIG2, SOX2, ASCL1*) while “injury-response” GSCs expressed markers of inflammation and integrin signaling (*ITGB1, ILK*). Importantly, a fraction of cells lay in between the 2 states and cells showed transitions from one state to another. Wang and colleagues identified that GBM cells broadly exist in a single axis of variation developing from mesenchymal to proneural subtypes. Importantly, they demonstrated that the full spectrum of GBM heterogeneity can be explained by varying proportion of GSCs in these subtypes, their proliferation potential and their interaction with the TME[189]. A recent study by Castellan and colleagues identified YAP/TAZ as master transcriptional regulators of the GSC-state. YAP/TAZ is

upregulated in the early stages of gliomagenesis where it maintains a stem-like state and prevents differentiation to the neuronal lineage. Remarkably, YAP/TAZ KO cells remain stuck in a differentiated state *in vitro* and intracranial tumors derived from these failed to form any outgrowth[190].

These studies have reshaped our understanding of stem cells and demonstrated that phenotypic switching underlies GBM heterogeneity. An accurate visualization of this redefined model can be made in the context of Waddigton's proposition of cellular epigenetic remodeling. This conventional model that applies to embryonic stem cells visualizes differentiating stem cells as marbles rolling down a hill, where every intersection represents a cell fate determinant, and the marble eventually settles at the valley representing terminally differentiated cells (as displayed in Figure 1.5A). In the context of GSCs, rather than such a linear differentiation hierarchy, cells interchange cell states making reversible cell fate decisions.

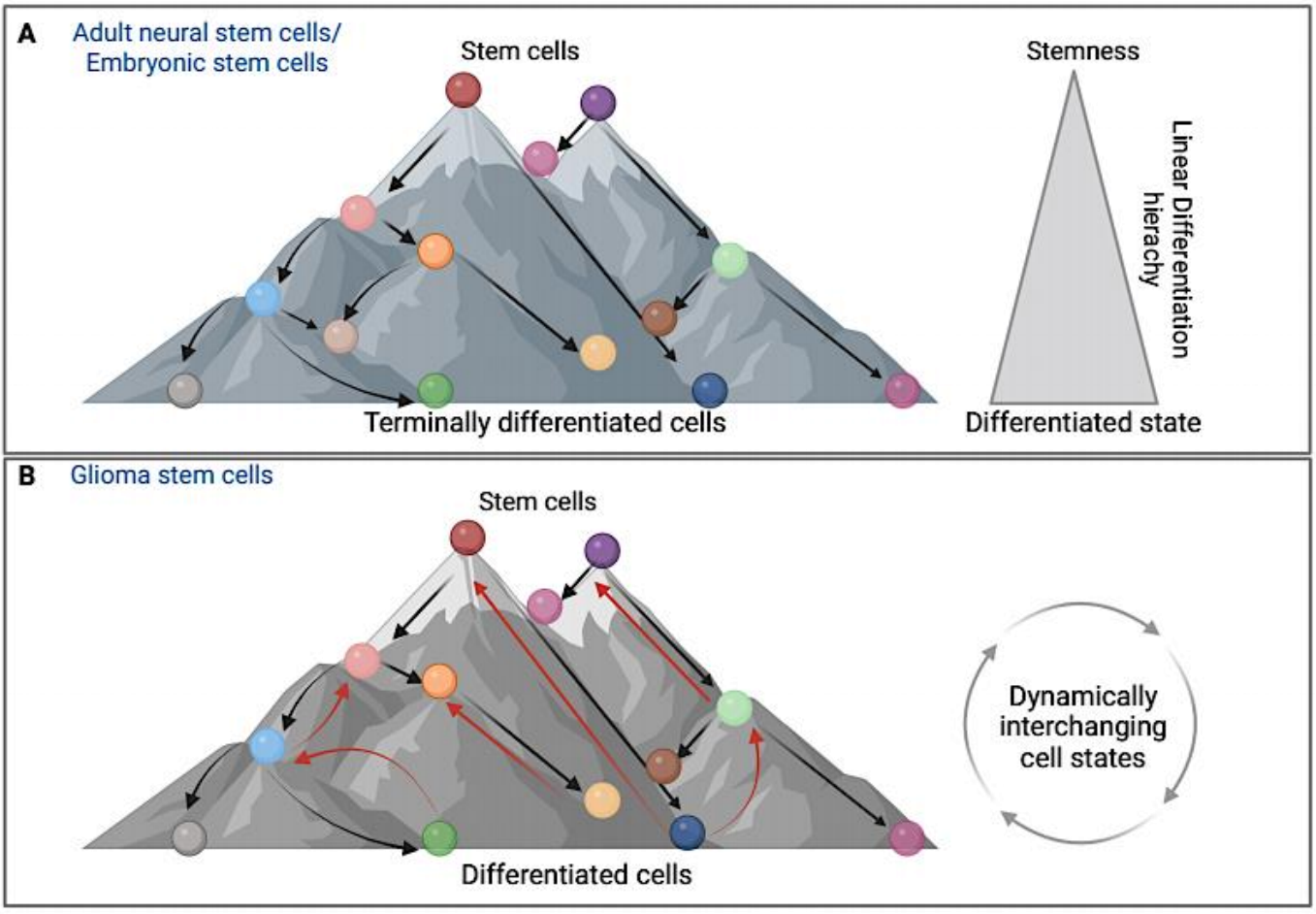

Figure 1.5: Visualization of the early and revised glioma stem cell model

(A) The early GSC differentiation model proposed a linear differentiation where apically located pluripotent stem cells differentiate into differentiated progenitors, generating distinct terminally differentiated cells.

(B) The revised GSC differentiation model proposes dynamically interchanging cell states with reversals to stem-like state from differentiated state. Red arrows represent reversal from more differentiated to more stem-like state, state alterations exhibited by glioma stem cells.

Clinically, this revised model implicates that targeted therapies may not be beneficial in GBMs and new treatment options must always be proposed while keeping in mind the circumventing of tumor heterogeneity.

2.3 Glioblastoma tumors display a uniquely altered metabolism

20% of the body's glucose is utilized by the brain, despite representing only 2% of the body's weight. GBM cells, therefore, invariably display a great reliance on glucose and upregulate the expression of glucose transporters (GLUT1/3) and several glycolytic genes. Consequently, glycolysis inhibition curbs GBM growth. Hexokinase 2 (Hk2), which commits glucose to glycolysis, is elevated in GBM and its depletion reduces growth of intracranial GBM xenografts but does increase invasion[191]. One must, however, consider the clinical translatability of targeting glycolysis, as metabolically active tissues like skeletal muscles, liver and adipose tissue rely on it as well. This is further confounded by metabolic adaptation in cancer cells. Maher *et al* transfused patients undergoing surgical resection with $^{13}C_6$-labelled glucose and identified that less than 50% of the acetyl coA in GBM tumors is derived from glucose[192]. In a subsequent study, the authors then showed that acetate, simultaneously with glucose, can be converted into acetyl-coA in GBM tumors as well as brain metastases. This is facilitated by acetyl coA synthetase2 (ACSS2)- and ACSS2 expression correlates with glioma aggressiveness and lower survival in GBM patients[193].

Regardless of origin, cytosolic acetyl coA may be channeled towards *de novo* fatty acid synthesis or cholesterol synthesis. Indeed, fatty acid metabolism plays a crucial role in brain physiology. 50% of the brain dry weight is composed of lipids, second only to adipose tissues. However, while

adipose tissues store fatty acids in the form of triglycerides for subsequent usage by peripheral tissues, FAs in brain tissues are mostly acylated and incorporated into membranes. Most of these include acylated long chain PUFAs which are derived from systemic circulation as they cannot be synthesized *de novo.* Uptake of these PUFAs by neurons is essential for maintaining cognitive function. Mice with KO of *FABP7*, the predominant FA uptake protein in brain, show symptoms of schizophrenia and neuronal dysfunction. Interestingly, transplantation of WT astrocytes in the brains of *FABP7* KO mice partially restores cognitive function, highlighting the importance of astrocyte-neuron crosstalk in maintain lipid homeostasis within the brain[194]. Indeed, neurons do not store lipid and rather rely on astrocytes which have large amounts of lipid droplets that can be oxidized during periods of nutrient stress and mobilized to neurons. Therefore, inter-cellular crosstalk forms a crucial basis of brain lipid homeostasis.

As opposed to neurons, GBM cancer cells retain the ability to synthesize and store fatty acids. FASN expression is correlated with glioma grade[195,196] and its inhibition *via* orlistat induces GBM cell apoptosis[196]. Hyperactivation of EGFR further augments this lipogenic phenotype. Guo and colleagues reported that EGFR amplification in GBMs activates SREBP-mediated lipogenesis and intracellular accumulation of fatty acids[197]. Further, lipogenesis inhibition in EGFRvIII expressing GBM cells via inhibiting ACC1/2 or AMPK activation inhibits proliferation of GBM cells[198,199]. Additionally, FASN expression is elevated in glioma stem cells (GSCs) and its inhibition reduces stem-like properties[200]. Elevated lipogenesis can be attributed to elevated SREBP activity in GBMs. EGF-mediated N-glycosylation of SREBP-cleavage activating protein (SCAP) promotes SREBP activation and lipogenesis in GBMs. Inhibition of SREBP signaling in EGFR amplified GBM tumors drastically reduced growth of GBM intracranial xenografts[201]. In GBMs, fatty acid levels are kept in check by a feedback regulation, whereby SREBP activates mir-29 transcription, which in turn inhibits SREBP signaling[202]. Fatty acid uptake is also relevant in GBM stem cells. GSCs display elevated FABP7 expression and its inhibition curbs growth of GBM xenografts *in vivo*[203–205]. One may propose that in GBMs, a large part of cytosolic acetyl coA is directed towards fatty acid synthesis. This is corroborated by the observation that GBM cells heavily rely on extracellular cholesterol uptake[206,207]. This is necessitated given peripheral cholesterol is unable to cross the blood-brain barrier (BBB), making brain cells reliant on *de novo* cholesterol production, most of

which is done by astrocytes[208]. Invariably, this means that GBM cells are very dependent on cholesterol uptake. This is mediated by reduced levels of LXR ligands (oxysterols-cholesterol derivatives), which in turn leads to increased expression of the cholesterol uptake receptor LDLR and reduced expression of the cholesterol efflux proteins ABCA1/ABCG1[206,207]. Treatment with a BBB-permeant LXR agonist, LXR-623, curbed the growth of GBM cells and prolonged survival in mice bearing patient-derived GBM orthotopic xenografts, while leaving normal brain cells unaffected[206]. GBM cells with EGFRvIII display a further EGF-dependent increase in cholesterol uptake[207]. Indeed, an EGFR/SCR/ERK1/2 signaling pathway reduces LXR mRNA levels and promotes cholesterol uptake in GBM cells[209]. These findings indicate that *de novo* lipogenesis is an important and prevalent pathway in GBMs.

Further, genomic alterations prevalent in GBM tissues also disrupt cellular metabolism and exposes metabolic vulnerabilities of these tumors. α-ketoglutarate acts as a co-factor for branched chain amino acid transaminases (BCAT1/2), which produce glutamate from branched chain amino acids (BCAAs). Consequently, IDH-mutated GBM cells rely on glutaminase (GLS), which deaminates glutamine to glutamate, making them preferentially sensitive to GLS inhibition[210]. Further, IDH-mutated GBMs have reduced activity of the NAD+ salvage pathway enzyme, nicotinate phosphoribosyltransferase (NAPRT). This makes them reliant on alternative NAD synthesis pathways and makes them especially sensitive to nicotinamide phosphoribosyltransferase (NAMPT) inhibition[211]. These findings suggest that metabolic targeting must be placed in the context of genotypes in GBM.

Chapter 2: Objectives

Despite a wealth of literature addressing the many roles of FA metabolism in cancers, many cancers evade targeting and continued investigation is essential to expose cancer-specific metabolic targets. Often, this evasion to targeted therapies can be attributed to cancer cell metabolic plasticity, wherein, cancer cells may depend on alternative route for metabolic processing. Thus, the overarching goal of this thesis was to identify novel metabolic vulnerabilities in cancer, particularly focusing on the fatty acid desaturation pathway. We have addressed this question in two published articles.

In the first study, described in Chapter 3, we identified an alternative FA monodesturation pathway that is novel to cancer cells. In this study, we specifically addressed two main questions:

- What renders several cancers capable of evading SCD inhibition?
- What is the effect of abrogating fatty acid monodesaturation on cancer growth?

By screening a panel of cancer cell lines of various tissue origins, we found that they displayed a range of SCD inhibitor sensitivity *in vitro*. To identify the metabolic contributors to this, we carried out FA profiling and observed that SCD inhibitor-insensitive cells, such as hepatocellular carcinoma (HCCs) and adenocarcinoma (ADC), produce the unusual MUFA sapienate, mediated *via* FADS2. We found that dual silencing of SCD and FADS2 induced complete cell death in HCC and ADC cells. Finally, we determined that SCD inhibition markedly reduced growth of HCCs derived *via* orthotopic transplantation of FADS2 silenced human HCC cells in nude mice.

Subsequent to this study, findings from the Fendt Lab by Triki and colleagues indicated that GBM tumors produce high amounts of sapienate[128]. This, in combination with previous reports showing the importance of SCD in GBMs, suggested to us that FA monodesturation is potentially prevalent and targetable in GBMs.

We therefore set out to investigate the role of FA desaturation in GBMs as described in Chapter 4. In this study, we wanted to investigate the following main questions:

- What is the status of FA synthetic genes in GBMs and do they display the GBM hallmark, intra-tumor heterogeneity?
- Does standard of care chemotherapy affect FA metabolism in newly diagnosed and recurrent GBMs?
- Does perturbation of FA saturation affect effectiveness of chemotherapy in GBM?

To address these questions, we started with analyzing single-cell gene expression data from GBM tissues and identified that *FASN*, *SCD* and *FADS2* display heterogeneous expression across cancer cell clusters and that the expression of these genes is correlated with cell fate. Next, we used an *in vitro* model of pair-matched newly diagnosed (ND) and recurrent (RC) patient-derived GBM cells cultured in lipid-depleted conditions, reminiscent of the brain microenvironment. We found that treatment with the chemotherapeutic agent temozolomide reduced gene expression and activities of FASN, SCD and FADS2 in ND but not RC cells, indicating that the TMZ response is blunted in RC GBM cells. Finally, we found that accumulation of intracellular palmitate *via* external supplementation or SCD and/or FADS2 inhibition in both ND and RC cells synergized with TMZ and dramatically induced cell death.

Chapter 3: Evidence for an alternative fatty acid desaturation pathway increasing cancer cell plasticity

3.1 Abstract

Most tumours have an aberrantly activated lipid metabolism[37,212] that enables them to synthesize, elongate and desaturate fatty acids to support proliferation. However, only particular subsets of cancer cells are sensitive to approaches that target fatty acid metabolism and, in particular, fatty acid desaturation[96]. This suggests that many cancer cells contain an unexplored plasticity in their fatty acid metabolism. Here we show that some cancer cells can exploit an alternative fatty acid desaturation pathway. We identify various cancer cell lines, mouse hepatocellular carcinomas, and primary human liver and lung carcinomas that desaturate palmitate to the unusual fatty acid sapienate to support membrane biosynthesis during proliferation. Accordingly, we found that sapienate biosynthesis enables cancer cells to bypass the known fatty acid desaturation pathway that is dependent on stearoyl-CoA desaturase. Thus, only by targeting both desaturation pathways is the in vitro and in vivo proliferation of cancer cells that synthesize sapienate impaired. Our discovery explains metabolic plasticity in fatty acid desaturation and constitutes an unexplored metabolic rewiring in cancers.

3.2 Methods

Cell lines, cell culture and chemicals

All cell lines were confirmed to be mycoplasma free, based on the MycoAlert Mycoplasma Detection Kit (Lonza). Human HEK293T epithelial cells, RWPE-1 prostate cells, MCFl0A breast cells, A549 and H460 lung carcinoma, MDA-MB-468 and T47D breast adenocarcinoma, and DU145 prostate carcinoma cell lines were obtained from ATCC. The HUH7 liver carcinoma cell line was obtained from the Japanese Collection of Research Bioresources (JCRB) Cell Bank. Cell lines have not been authenticated, with the exception of MDA-MB-468 cells, which were authenticated by fingerprinting. RWPE-1 cells were cultured in keratinocyte serum-free medium (K-SFM), supplemented with 0.05 mg per ml bovine pituitary extract, 5 ng per ml epidermal growth factor, 1% penicillin (50 U per ml) and 1% streptomycin (50 µg per ml) (Life Technologies).

MCF10A cells were cultured in Dulbecco's modified Eagle's medium-F12 (DMEM-F12) (Life Technologies), supplemented with 5% horse serum (Life Technologies), 1% penicillin (50 U per ml) (Life Technologies), 1% streptomycin (50 μg per ml) (Life Technologies), 0.5 μg per ml hydrocortisone (Sigma-Aldrich), 100 ng per ml cholera toxin (Sigma-Aldrich), 10 μg per ml insulin (Sigma-Aldrich), and 20 ng per ml recombinant human epidermal growth factor (PeproTech EC). Other cells were cultured in high glucose (4.5 g per l) Dulbecco's modified Eagle's medium (DMEM) (Life Technologies) supplemented with 10% heat-inactivated fetal bovine serum (Invitrogen), 1% penicillin (50 U per ml) (Life Technologies) and 1% streptomycin (50 μg per ml) (Life Technologies). For growth and labelling experiments, low serum conditions (0.5–1% FBS) were applied. $^{13}C_6$-glucose (CLM-1396 Cambridge Isotope Laboratories) was used for labelling experiments. Hygromycin B and puromycin dihydrochloride (Life Technologies) were added to the growth medium for selection of overexpression and knockdown cell lines, respectively. Merck Frosst compound 3j[213] was used as an SCD inhibitor, as described in the patent application WO2006/130986. The fatty acids palmitoleate (16:1), sapienate (16:1) and oleate (18:1) were purchased from Sigma-Aldrich. *cis*-8-octadecenoate (18:1) was purchased from Larodan. Solvents for metabolite extraction and mass spectrometry were HPLC-grade from Sigma-Aldrich.

Knockdown and overexpression strategies

FADS2 knockdown cell lines were generated using the shRNA-expressing lentiviral pLKO1-puro vector with a puromycin selection cassette (Plasmid 8453; Addgene). Clone identities for shRNAs were as follows: shFADS2-1 (TRCN0000064755; sequence: CCGGCCACGGCAAG-AACTCAAAGATCTCGAGATCTTTGAGTTCTTGCCGTGGTTTTTG) and shFADS2-2 (TRCN0000064757; sequence: CCGGC CACCTGTCTGTCTACAGAAACTCGAGTTTCTGTAGA-CAGACAGGTGGT TTTTG) (Sigma-Aldrich). A scrambled shRNA (*TRC1* sequence: AACAAGATG AAGAGCACCAA) was used as a negative control for *FADS2* knockdown cells. *FADS2* overexpression cell lines were generated using the pLVX-IRES-Hyg vector with a hygromycin selection cassette (Clontech Laboratories). An empty pLVX-IRES-Hyg vector served as a negative control for *FADS2* overexpression. Lentiviruses were produced by transfection of HEK293T cells. Transduction of cells was performed overnight and the medium was replaced the next day. Poly-clonal cells were selected for 1–2 weeks with puromycin (in the case of knockdown cells) or with hygromycin (in the case of overexpression),

before experiments were performed. All knockdown and overexpression cell lines were validated by quantitative real-time PCR (qRT–PCR) and protein analysis. Primers for *FADS2* were designed to amplify a cDNA segment in the sequence as follows: forward primer 5′-gaccacggcaagaactcaaag-3′ and reverse primer 5′-gagggtaggaatccagccatt-3′. For *SCD1*, the forward and reverse primers used were 5′-tctctgctacacttgggagc-3′ and 5′-gagctttgtaagagcggtgg-3′, respectively. Relative gene transcript levels were compared to the control gene *RPL19*, with 5′-attggtctcattggggtctaac-3′ and 5′-agtatgctcaggcttcagaaga-3′ as forward and reverse primer, respectively. Real-time PCR reactions were performed on a 7,500 Fast Real-Time PCR System (Applied Biosystems, Life Technologies). Amplification was performed at 95 °C for 10 min, followed by 40 cycles of 15 s at 95 °C and 1 min at 60 °C. Samples were assayed in triplicates.

Quantification of *FADS2* gene expression in primary tumours

Human HCC and adjacent normal liver tissue samples were retrieved from the archive of the Institute of Pathology of the LMU Munich with approval of the ethics committee of LMU Munich (approval no. 307-16 UE). Representative tumour and normal tissue areas were reviewed by a resident pathologist in representative tissue slides stained with haematoxylin and eosin (H & E). Corresponding areas were micro-dissected from paraffin blocks using biopsy punches (2-mm diameter). Deparaffinization of the tissue and RNA isolation was carried out using the Formapure Total Kit (Beckman Coulter). cDNA synthesis was performed using 1 µg of RNA with the MultiScribe Reverse Transcription kit (Applied Biosystems). Analysis of the gene expression of *FADS2* was performed by qRT–PCR using SYBR-Green Master Mix (Applied Biosystems) in a CFX Connect Real-Time System (Bio-Rad). Primers were used at a concentration of 0.5 µM in a final reaction volume of 15 µl. Three technical replicates were analysed per sample. *RPLP0* expression was used as a control for normalization. Primer sequences were as follows: *FADS2* forward primer 5′-gaccacggcaagaactcaaag-3′ and reverse primer 5′-gagggtaggaatccagccatt-3′; *RPLP0* forward primer 5′- gaaactctgcattctcgcttc-3′ and reverse primer 5′- ggtgtaatccgtctccacag-3′.

Human non-small-cell lung cancer and adjacent normal lung samples were retrieved from patients enrolled in an IRB-approved protocol, after obtaining informed consent (ClinicalTrials.gov identifier, NCT02095808). On the basis of pre-operative imaging and gross

inspection at resection, viable fragments of tumour and lung were sampled. RNA isolation was carried out using the Trizol reagent (Thermo Fisher Scientific) and FastPrep-24 (MPbio). cDNA synthesis was performed using 1 μg of RNA with the qScript cDNA Synthesis Kit (QuantaBio). Analysis of *FADS2* gene expression was performed by qRT–PCR using Platinum SYBR Green qPCR SuperMix-UDG (Thermo Fisher Scientific) on a Viia7 Real Time PCR system (Applied Biosystems, Life Technologies). Amplification was performed at 95 °C for 10 min, followed by 40 cycles of 15 s at 95 °C and 1 min at 60 °C. Primers for *FADS2* were designed to amplify a cDNA segment in the sequence as follows: forward primer 5′-gaccacggcaagaactcaaag-3′ and reverse primer 5′-gagggtaggaatccagccatt-3′. Relative gene transcript levels were compared to the control gene *RPL19*, with 5′-attggtctcattggggtctaac-3′ and 5′-agtatgctcaggcttcagaaga-3′ as forward and reverse primer, respectively. Samples were assayed in triplicates.

Growth and labelling experiments

Cancer cells were seeded in the wells of 12-well plates (Corning) at either 7×10^4 cells per well (HUH7, A549, H460 and DU145), 1.5×10^5 cells per well (MDA-MB-468) or 2×10^5 cells per well (T47D) in low FBS DMEM (1.5 ml per well) and grown in a humidified environment at 37 °C with 5% CO_2. For HUH7, 1% FBS was considered low FBS DMEM; for all other cell lines, 0.5% FBS was used. Low FBS (0.5–1%) DMEM contains a total of 4.31–8.62 μM fatty acids, with palmitate, oleate and stearate being the most abundant fatty acids. After 24 h, the medium was aspirated, cells were washed with DPBS and low FBS DMEM (4.5 g per l glucose for growth experiments or 4.5 g per l $^{13}C_6$-glucose for labelling experiments, including fatty acid synthesis assessment), supplemented with 0.1% DMSO (control) or Merck Frosst compound 3j (either at 0.5 nM, 1 nM or 2 nM concentration dissolved in DMSO) added to the wells (1.5 ml per well). Treatment was carried out for 72 h, during which cells were grown in a humidified environment at 37 °C with 5% CO_2. For growth experiments, cells were counted before treatment (initial count) and 72 h after treatment (final count) using a Moxi Z Mini Automated Cell Counter (Orflo Technologies) or a Countess II Automated Cell Counter (Thermo Fisher Scientific) following trypsinization. Cell number change was calculated by subtracting the initial count from the final count, and was subsequently normalized to the control condition, unless stated otherwise. For labelling experiments, cells were washed with saline solution after treatment and metabolism was

quenched by flash-freezing the plates in liquid nitrogen. Plates were stored at –80 °C until metabolite extraction. All experiments were performed in triplicates. Key experiments were confirmed in medium with glucose and amino acid concentrations similar to blood (BLM)[214,215] in low FBS.

For rescue experiments, cells were seeded and grown as described above. After 24 h, the medium was replaced by medium containing 0.1% DMSO (control) or Merck Frosst compound 3j (0.5 nM, 1 nM or 2 nM), supplemented with either 1% ethanol (control) or 20 µM palmitoleate (*cis*-9-16:1), sapienate (*cis*-6-16:1), oleate (*cis*-9-18:1) or *cis*-8-octadecenoate (*cis*-8-C18:1) dissolved in ethanol. Cells were counted before treatment and 72 h after treatment using a Moxi Z Mini Automated Cell Counter (Orflo Technologies) or a Countess II Automated Cell Counter (Thermo Fisher Scientific) following trypsinization, and relative cell number changes were calculated as described above. All experiments were performed in triplicates. Changes in intracellular fatty acid abundance upon supplementation were confirmed by mass spectrometry.

Primary hepatocytes of one donor were obtained from the Hepatocytes and Liver Stem Cell Bank, Cliniques Universitaires St Luc. Cells were thawed using the Corning Gentest High Viability CryoHepatocyte Recovery Kit (Corning). Cells were then plated on collagen-I-coated 6-well plates at a density of 1.4×10^6 cells per well, and left to attach for 8 h in Corning Plating Medium (Corning).

Reverse labelling experiments

HUH7 and A549 cells were seeded at 1×10^6 cells per flask in T75 flasks in low FBS (1% FBS, HUH7) or 10% FBS (A549) DMEM and grown as described above. After 24 h, the medium was aspirated, cells were washed with DPBS and 1% (HUH7) or 10% (A549) dialysed FBS DMEM (4.5 g per l $^{13}C_6$-glucose) was added to the cells. Cells were cultured for 1 week (medium was replaced every 3 days) to fully label all cellular metabolites. Next, cells were trypsinized, washed and seeded in the wells of a 12-well plate at 7×10^4 cells per well in low FBS DMEM containing 4.5 g per l $^{13}C_6$-glucose (1% FBS for HUH7 and 0.5% FBS for A549). After 24 h, the medium was aspirated, cells were washed with DPBS and low FBS DMEM containing 4.5 g per l $^{13}C_6$-glucose (1% FBS for HUH7 and 0.5% FBS for A549) supplemented with either 1% ethanol (control) or 20 µM ^{12}C-sapienate

(*cis*-6-16:1) dissolved in ethanol was added to the cells (1.5 ml per well). Treatment was carried out for 72 h. After treatment, cells were washed with saline solution and metabolism was quenched by flash-freezing the plates in liquid nitrogen. Plates were stored at –80 °C until metabolite extraction. All experiments were performed in triplicates.

If fully labelled cells use ^{12}C-sapienate, a decrease in the ^{13}C enrichment will be observed in the metabolites into which sapienate is incorporated, such as *cis*-8-octadecenoate. Because our gas chromatography–mass spectrometry (GC–MS) setup does not allow for separation of *cis*-8- and *cis*-9-octadecenoate, and our gas chromatography–flame ionization detector (GC–FID) setup does not allow for assessment of ^{13}C enrichment, we opted to assess the ^{13}C enrichment in the pool of octadecenoate (consisting of *cis*-8- and *cis*-9-octadecenoate) via GC–MS. Note that only *cis*-8-octadecenoate, and not *cis*-9-octadecenoate, can result from sapienate metabolism. Therefore, a decrease in ^{13}C enrichment in the octadecenoate pool indicates the incorporation of ^{12}C-sapienate into *cis*-8-octadecenoate.

Metabolite extraction and metabolite measurement

Metabolite extractions were performed using previously described methods[216,217]. In brief, for 12-well cell culture plates containing 1–5 × 10^5 cells per well, the medium was aspirated, cells were washed with blood bank saline, and cell metabolism was quenched by flash-freezing the plates in liquid nitrogen. Next, 400 µl of –20 °C cold 65% methanol was added to the wells, cells were scraped with a pipette tip and suspensions were transferred to Eppendorf tubes. Next, 250 µl of –20 °C cold chloroform was added and samples were vortexed at 4 °C for 10 min to extract metabolites. Phase separation was achieved by centrifugation at 4 °C for 10 min, after which the chloroform phase (containing the total fatty acid content) was separated and dried by vacuum centrifugation. For tissue samples, tissues were weighed (5–10 mg) and pulverized (Cryomill, Retsch) under liquid nitrogen conditions. For plasma samples, 10 µl (mouse) or 50 µl (human) of cold plasma was transferred to an Eppendorf tube. Next, 800 µl of –20 °C cold 65% methanol was added to the samples, followed by 500 µl of –20 °C cold chloroform. Samples were then handled as described above. Dried fatty acid samples were immediately processed to fatty acid methyl esters as described below, thereby avoiding degradation.

Total fatty acid samples were esterified with 500 µl 2% sulfuric acid in methanol for 180 min at 60 °C or overnight at 50 °C and extracted by addition of 600 µl hexane and 100 µl saturated aqueous NaCl. Samples were centrifuged for 5 min and the hexane phase was separated and dried by vacuum centrifugation. Samples were resuspended in hexane, after which isotopologue distributions of fatty acids were measured with a 7890A GC system (Agilent Technologies) combined with a 5975C or a 7000 inert MSD system (Agilent Technologies). One microlitre of each sample was injected in splitless (5975C) or 5:1 split (7000) mode with an inlet temperature of 270 °C onto a DB35MS column (Agilent Technologies). Helium was used as a carrier gas with a flowrate of 1 ml per min. The oven was held at 80 °C for 1 min and ramped with 5 °C per min to 300 °C. The mass spectrometry system was operated under electron impact ionization at 70 eV and a mass range of 100–650 amu was scanned. Isotopologue distributions were extracted from the raw chromatograms using an in-house MATLAB script. Correction for naturally occurring isotopologues was achieved using Isocor software. Palmitate, palmitoleate and sapienate synthesis were calculated on the basis of isotopologue distributions of the according fatty acid, using isotopomer spectral analysis[218] and an in-house MATLAB script. For determination of relative metabolite abundances, the total ion counts were normalized to an internal standard (pentadecanoate or heptadecanoate) and the cell number or protein content for cell extracts. For tissue extracts, the total ion counts were normalized to the internal standard (pentadecanoate or heptadecanoate) and tissue weight. The desaturation activity from palmitate to sapienate or palmitoleate was calculated by dividing the normalized total ion count of sapienate or palmitoleate by the normalized total ion count of palmitate.

cis-8-Octadecenoate abundances were measured with a GC–FID system (TRACE GC ULTRA, Thermo Fisher Scientific). One microlitre of each sample was injected onto a SLB-IL111 capillary column (100 m × 0.25 mm ID, 0.20-µm thickness, Supelco) with an inlet temperature of 250 °C. Helium was used as a carrier gas at 1.2 ml per min and the oven temperature was maintained isothermally at 140 °C. *cis*-C18:1 isomers (Δ8,9,11) were synthesized as previously described[219], processed to fatty acid methyl esters, and used for validation of the separation of *cis*-C18:1 isomers and confirmation of the retention times of respective *cis*-C18:1 fatty acid methyl esters. For determination of relative *cis*-8-octadecenoate abundances, the total ion counts were

normalized to the internal standard (pentadecanoate or heptadecanoate). For cell extracts, total ion counts were further normalized to the protein content or to the total fatty acid abundance. Total ion counts in tissue samples were further normalized to tissue weight.

FADS2 protein analysis

Human cell pellets (1–4 × 10^7 cells per pellet) in triplicate were lysed in a urea lysis buffer containing 8 M urea and 20 mM HEPES pH 8.0. Cell pellets were homogenized by sonication on a Diagenode Bioruptor Plus instrument using the following settings: high intensity power output, 10 cycles of 30-s on/30-s off pulses, 4 °C water bath. The protein concentration in each lysate was measured by Bradford (Bio-Rad Laboratories) and aliquots containing 100 µg of protein were used for further analysis. Proteins were reduced by addition of DTT to a concentration of 5 mM and incubation for 30 min at 55 °C. Next, proteins were alkylated by addition of iodoacetamide to a concentration of 10 mM for 15 min at room temperature in the dark. Samples were diluted with 20 mM HEPES pH 8.0 to a urea concentration of 4 M and proteins were digested with 1 µg lysyl endopeptidase (Wako Chemicals) (1/100, w/w) for 4 h at 37 °C. Samples were further diluted with 20 mM HEPES pH 8.0 to a final urea concentration of 2 M and proteins were digested with 1 µg trypsin (Promega) (1/100, w/w) overnight at 37 °C. The resulting peptide mixture was purified using OMIX C18 pipette tips (Agilent Technologies) or SampliQ SPE C18 cartridges (Agilent Technologies) and 100 µg of peptides of each sample were dried completely by vacuum drying and stored at –20 °C until further use.

Peptides were re-suspended in loading solvent (0.1% TFA in water/acetonitrile, 98/2 (v/v)) and 3 µg was injected for liquid chromatography with tandem mass spectrometry (LC–MS/MS) analysis on an Ultimate 3000 RSLC nano LC (Thermo Fisher Scientific) in-line-coupled to a Q Exactive HF mass spectrometer (Thermo Fisher Scientific). The peptides were first loaded on a trapping column (made in-house, 100-µm internal diameter (I.D.) × 20 mm, 5-µm beads C18 Reprosil-HD, Dr. Maisch) and after flushing from the trapping column, peptides were separated on an analytical column in the needle (made in-house, 75 µm I.D. × 400 mm, 1.9-µm beads C18 Reprosil-HD, Dr. Maisch) using a nonlinear 150 min gradient of 2 to 56% solvent B (0.1% formic acid in water/acetonitrile, 20/80 (v/v)) at a constant flow rate of 250 nl per min and at a constant

temperature of 50 °C (CoControl 3.3.05, Sonation). Following a 10-min wash reaching 99% solvent B, the column was re-equilibrated with solvent A (0.1% formic acid in water).

The mass spectrometer was operated in data-dependent, positive ionization mode, automatically switching between mass spectra and tandem mass spectra acquisition for the 16 most abundant peaks in a given mass spectrum. The source voltage was set to 2.5 kV and the capillary temperature was 250 °C. One MS1 scan (*m*/*z* 375–1,500, AGC target 3×10^6 ions, maximum ion injection time of 60 ms), acquired at a resolution of 60,000 (at 200 *m*/*z*) was followed by up to 16 tandem mass spectrometry scans, acquired at a resolution of 15,000 (at 200 *m*/*z*) of the most intense ions fulfilling predefined selection criteria: AGC target 1×10^5 ions, maximum ion injection time of 80 ms, isolation window of 1.5 *m*/*z*, fixed first mass of 145 *m*/*z*, spectrum data type: centroid, under fill ratio 2%, intensity threshold 1.3×10^4, exclusion of unassigned and singly charged precursors, peptide match preferred, exclude isotopes on, dynamic exclusion time of 12 s. The normalized collision energy was set to 28% and the polydimethylcyclosiloxane background ion at 445.12003 Da was used for internal calibration (lock mass).

Data analysis was performed by MaxQuant (version 1.6.1.0) using the Andromeda search engine with default search settings, including a false discovery rate set at 1% on both the peptide and protein level. Spectra were searched against the human proteins in the Swiss-Prot database (database release version of December 2017, containing 20,243 human protein sequences; downloaded from www.uniprot.org). The mass tolerance for precursor and fragment ions was set to 4.5 and 20 p.p.m., respectively, during the main search. Enzyme specificity was set as C-terminal to arginine and lysine (trypsin), also allowing cleavage at arginine–proline or lysine–proline bonds with a maximum of two missed cleavages. Carbamidomethylation of cysteine residues was set as a fixed modification and variable modifications were set to oxidation of methionine residues (to sulfoxides) and acetylation of protein N termini. Proteins were quantified by the MaxLFQ algorithm integrated in the MaxQuant software. Only proteins with at least one unique or razor peptide were retained for identification, and a minimum ratio count of two unique peptides was required for quantification. The obtained label-free quantification intensity

values of FADS2 were used to quantify the protein, and to compare levels of FADS2 between different samples.

Analysis of phospholipid-bound sapienate and palmitoleate

HUH7 cells carrying a non-targeting shRNA or a shRNA targeting *FADS2* (shFADS2-2) were seeded in T75 flasks, allowed to attach for 24 h and subsequently grown for 72 h in 1% FBS DMEM. Cells were trypsinized, washed with blood bank saline and re-suspended in TAG lysis buffer (1% IGEPAL CA-630 (Nonidet P-40), 50 mM Trizma hydrochloride and 150 mM sodium chloride). Lipids were extracted from cell lysate according to the Folch method[220]. An internal standard containing a known concentration of 1,2-diheptanoyl-*sn*-glycero-3-phosphocholine (17:0) was added to samples before extraction to allow the quantification of total phospholipids. Lipid fractions were separated by thin-layer chromatography and fatty acid methyl esters were prepared as previously described[221,222]. Separation and detection of total phospholipid fatty acid methyl esters was achieved using a 6890N Network GC System (Agilent Technologies) with flame ionization detection. Fatty acid methyl esters were identified by their retention times compared to a standard containing 31 known fatty acids and quantified in micromoles from the peak area based on their molecular mass. The micromole quantities were then totalled and each fatty acid was expressed as a percentage of this value (molar percentage (mol%)), or as micrograms of fatty acids normalized to cellular protein amount.

Analysis of phospholipid species

HUH7 and A549 cells carrying a non-targeting shRNA or one of two shRNAs targeting *FADS2* (shFADS2-1 or shFADS2-2) were seeded in T75 flasks, allowed to attach for 24 h and subsequently grown for 72 h in low FBS DMEM (1% FBS for HUH7; 0.5% FBS for A549). Cells were trypsinized, washed three times with cold DPBS and cell pellets were re-suspended in 0.8 ml DPBS. Lipid extraction and multiple reaction monitoring (MRM)-based phospholipid (semi)quantification analysis was performed as previously described[223]. In brief, 0.7 ml of homogenized cells were mixed with 0.9 ml MeOH:HCl (1 M) (8:1), 0.8 ml $CHCl_3$ and 200 µg per ml of the antioxidant 2,6-di-*tert*-butyl-4-methylphenol (Sigma). The organic fractions were evaporated under vacuum using a Savant Speedvac spd111v (Thermo Fisher Scientific) at room temperature and the remaining lipid pellet was stored at –20 °C under argon. Before mass

spectrometry analysis, lipid pellets were reconstituted in running solution (CH_3OH:$CHCl_3$:NH_4OH; 90:10:1.25; v/v/v). The lipid standards phosphatidylcholine (PC)25:0, PC43:6, sphingomyelin (SM)30:1, phosphatidylethanolamine (PE)25:0, PE43:6, phosphatidylinositol (PI)25:0, PI31:1, PI43:6, phosphatidylserine (PS)25:0, PS31:1 and PS37:4 (Avanti Polar Lipids) were added based on the amount of DNA of the original sample. Phospholipids were analysed by electrospray ionization tandem mass spectrometry (ESI-MS/MS) on a hybrid quadrupole linear ion trap mass spectrometer (4000 QTRAP system, AB SCIEX) equipped with a TriVersa NanoMate robotic nanosource (Advion Biosciences) for automated sample injection and spraying as previously described[224]. Phospholipid profiling was executed by (positive or negative) precursor ion or neutral loss scanning at a collision energy of 50 eV or 45 eV, 35 eV, −35 eV and −60 eV for precursor 184 (SM or PC), neutral loss 141 (PE), neutral loss 87 (PS) and precursor 241 (PI), respectively. Phospholipid quantification was performed by MRM, the transitions being based on the neutral losses or the typical product ions as described above. Typically, a 3-min period of signal averaging was used for each spectrum. The data were corrected for carbon isotope effects and chain length, and analysed using in-house-developed software (RALP). As a background, the intensities of species detected in the 'internal standards only' spectra were considered after being divided by the ion suppression factor of each sample. The ion suppression factor was calculated for each sample separately by dividing the intensity of the standards in the 'internal standards only' spectrum by the intensity of the standards in the sample spectrum. Only the phospholipid species displaying an intensity of at least 5 times the blank value were taken into account. To quantify the total amount of phospholipids in a phospholipid class, the abundances of individually measured species within the phospholipid class were totalled. Data were normalized on the basis of DNA amount. MRM-based analysis of the C16:1-containing phospholipids was based a previous method[225].

Analysis of lipid peroxidation sensitivity

HUH7 control and *FADS2* knockdown cells (3×10^7 cells each) were seeded in 15-cm Petri dishes in 1% FBS DMEM. After 24 h, cells were treated with control or 5 µM RSL3 (the latter inhibits glutathione peroxidase 4 and induces lipid peroxidation). Lipid peroxidation was quantified using the MDA assay kit (Sigma) according to manufacturer's instructions with some exceptions. In

brief, 3×10^7 cells were collected in BHT-supplemented PBS. TBA-acetic acid solution was buffered to pH 3.5. Plates were read using an EnSpire Multimode Plate Reader (PerkinElmer). Signal was normalized to total amount of sample DNA.

Analysis of membrane fluidity

HUH7 and A549 control and *FADS2* knockdown cells were grown on glass coverslips (n = 4) in low FBS DMEM (1% FBS for HUH7; 0.5% FBS for A549) for 3 days and subsequently fixed for 15–30 min in 4% PFA at room temperature. For lipid phase analysis, cells were stained with di-4-ANEPPDHQ (Thermo Fisher Scientific) according to the manufacturer's specifications. For imaging, a Nikon A1R confocal microscope attached to Ti eclipse outfitted with a Plan Apo VC 60× lens oil immersion lens with a numerical aperture of 1.4 was used (Nikon Instruments). The spectral detector was set to 530–590 and 590–650 nm to image the spectral shift of the dye from lipid ordered to disordered phases. Resulting images were analysed with NIS software (Nikon Instruments), thereby segmenting the cells in the images and calculating the ordered-to-disordered ratio[226]. The higher the ordered-to-disordered ratio, the more saturated lipids are present in the membrane. Ten fields of view were imaged per coverslip.

Mouse models

All mouse experiments were approved by the local authorities in compliance with all relevant ethical regulations (including, but not limited to, tumour size). For injection models, mice were randomized before injection of cancer cells. All samples were analysed blinded. Sample size was determined using power calculations with $\beta = 0.8$ and $P < 0.05$ based on preliminary data and in compliance with the 3R system (replacement, reduction, refinement).

Subcutaneous HUH7 xenograft model

Mice were fed ad libitum a CRM (E) expanded low-fat diet (Special Diets Services 801730) one week before the start of the experiments until they were killed. HUH7 cells (1×10^6) were subcutaneously injected in 50% Matrigel, (BD Biosciences), 50% cell culture medium without FCS into 8–9-week old female immunocompromised $NMRI^{nu/nu}$ mice (Taconic M&B A/S). Tumours were allowed to grow up to a mean tumour size of 30 mm^2 (length × width), before mice were allocated to treatment and control group by stratified randomization based on their primary

tumour size (8 mice per group). Tumour-bearing mice were either treated with vehicle (10% v/v ethanol, 40% v/v solutol) alone or with 1.5 mg per kg SCD inhibitor Merck Frosst compound 3j for six consecutive days twice daily p.o. After the last treatment, mice were euthanized and tumours were collected and snap-frozen for further analyses. Humane endpoints were determined as a tumour size of 225 mm^2. Additionally, the following symptoms were monitored and upon detection of one of the symptoms the mouse was euthanized: ulcerated tumours, loss of 20% body weight, self-mutilation, constant circling, constant curved posture, blood attachment at body openings, bloody diarrhoea, abnormal breathing, constant eye and nasal discharge, apathic, constantly cramps, constant tremble, crouching posture and self-isolation. All mouse experiments were conducted in accordance with the European Union directives and the German animal welfare act and approved by the Landesamt für Gesundheit und Soziales (LAGeSo).

DEN-induced hepatocellular carcinoma model

Male C57Bl/6N mice were obtained from the KU Leuven animal facility and injected with DEN (25 mg per kg) intraperitoneally at the age of two weeks. After 4 weeks, mice were fed with a 13 kJ% fat diet (Ssniff S8655-E220) until killed and analysed at 20, 30, 31 or 32 weeks after DEN administration. Tumour and non-tumour tissues were collected and rapidly frozen for metabolomic analysis using a liquid-nitrogen-cooled Biosqueezer (Biospec Products). Tissues were weighed (5–10 mg) and pulverized (Cryomill, Retsch) under liquid nitrogen conditions. The pulverized tissues were extracted for GC–MS analysis as described above. Humane endpoints were determined as follows: liver tumours can be detected by palpation as hard masses in otherwise soft abdominal area, or by an enlarged abdomen at later stages. In mice, a 20% increase in the normal abdomen diameter was considered as a humane endpoint. Additionally, the following symptoms were monitored and upon detection of one of the symptoms the mouse was euthanized: loss of ability to ambulate, loss of skin elasticity, laboured respiration or weight loss over 20% of initial body weight. Housing and experimental mouse procedures were approved by the Institutional Animal Care and Research Advisory Committee of the KU Leuven.

Hepatocyte-specific Pten or Stk3 and Stk4 knockout hepatocellular carcinoma model

Mice were fed standard chow ad libitum throughout the procedure. C57BL/6 mice carrying *Pten* conditional knockout alleles were crossed with albumin (Alb)–Cre-transgenic mice. Control mice were *Pten*$^{loxP/loxP}$*;Alb-cre*$^{-}$, whereas the experimental mice were *Pten*$^{loxP/loxP}$*;Alb-cre*$^{+}$. For hepatocyte-specific *Stk3* and *Stk4* deletion, mice carrying *Stk3* and *Stk4* conditional knockout alleles (in a mixed background of CD1, C57BL/6 and 129) were crossed with Alb–Cre-transgenic mice. Control mice were *Stk3*$^{loxP/loxP}$*;Stk4*$^{loxP/loxP}$*;Alb-cre*$^{-}$, whereas the experimental mice were *Stk3*$^{loxP/loxP}$*;Stk4*$^{loxP/loxP}$*;Alb-cre*$^{+}$. At necropsy (approximately 12 months for *Pten* and 4–6 months for *Stk3* and *Stk4*), tumours and liver tissues were collected and snap-frozen for further analysis from male mice. Humane endpoints were determined as maximum tumour size on the basis of linear or volumetric measurements. In mice, when linear measurements are used the longest dimension of the tumour should not exceed 2.0 cm and—if multiple tumours are present—the combination of the two longest diameters may not exceed 2.0 cm. Tumour volume (TV) can also be used to evaluate tumour size using the following formula: TV = (width)2 × length/2. The maximum single tumour size or tumour burden for mice is 2,000 mm^3. All animal procedures were approved by and carried out in accordance with the policies and regulations set forth by the Institutional Animal Care and Use Committee (IACUC) at MD Anderson Cancer Center.

Hepatocyte-specific myrAKT–Nras overexpression hepatocellular carcinoma model

Wild-type FVB/N mice were obtained from Charles River and subjected to hydrodynamic injection. In brief, 10 μg of the plasmids encoding myr-AKT1 and/or Nras(V12) along with sleeping beauty transposase in a ratio of 25:1 were diluted in 2 ml saline (0.9% NaCl), filtered through a 0.22-μm filter, and injected into the lateral tail vein of 6 to 8-week-old FVB/N male mice in 5 to 7 days. After 6–9 weeks, tumours were collected and snap-frozen for further analysis. Humane endpoints were determined as follows: liver tumours can be detected by palpation as hard masses in otherwise soft abdominal area, or an enlarged abdomen at later stages. Tumours were recorded when first noticed. In mice, a 20% increase in the normal abdomen diameter was considered as a humane endpoint. Mice were housed, fed and monitored in accordance with

protocols approved by the Committee for Animal Research at the University of California, San Francisco.

Orthotopic HUH7 liver cancer model

Mice were fed ad libitum a CRM (E) expanded low-fat diet (Special Diets Services 801730) one week before the start of the experiments until they were killed. Next, 0.5×10^6 HUH7 control or shFADS2-2 cells were orthotopically injected in 100% Matrigel, (BD Biosciences) into the left liver lobe of anaesthetized (3% isoflurane, 2% oxygen) 6-week-old male immunocompromised $NMRI^{nu/nu}$ mice (Taconic M&B A/S). For analgesia, mice were given 5 mg per kg carprofen subcutaneously, before and after surgery and for the following 3 d. After 8 d, mice were either treated with vehicle (10% v/v ethanol, 40% v/v solutol) alone or with 1.5 mg per kg SCD inhibitor Merck Frosst compound 3j for six consecutive days twice daily p.o. Fourteen hours after the last treatment, mice were euthanized, the tumour nodule was resected, and blood and normal liver tissue were sampled. For metabolomic analysis, half of the tumour nodule and non-tumour tissues were rapidly frozen using a liquid-nitrogen-cooled Biosqueezer (Biospec Products). Tissues were then weighed (5–10 mg) and pulverized (Cryomill, Retsch) under liquid nitrogen conditions. The pulverized tissues were extracted for GC–MS analysis as described above. For histological quantification of the tumour area, half of the nodule was formalin-fixed and paraffin-embedded (FFPE). From these FFPE tissue blocks, 4-µm sections were cut and stained with H & E. The mean tumour area as a per cent of the total tissue area was determined in low-power magnifications by two independent physicians trained in histopathology. Humane endpoints were determined as a tumour size of 2 cm^3. Additionally, the following symptoms were monitored and upon detection of one of the symptoms the mouse was euthanized: loss of ability to ambulate, laboured respiration, surgical infection or weight loss over 10% of initial body weight. Housing and experimental mouse procedures were approved by the Institutional Animal Care and Research Advisory Committee of KU Leuven.

Collection of clinical samples

Human samples were collected upon ethical approval of local authorities. Analysis was performed blinded.

Liver

Liver and/or liver cancer samples were obtained from Indivumed GmbH, from the Laboratory of Hepatology (Commissie Medische Ethiek UZ Leuven – KU Leuven) and the archive of the Institute of Pathology of the LMU Munich with approval of the ethics committee of LMU Munich (approval no. 307-16 UE), respecting patients' rights. Blood samples from healthy volunteers and patients with HCC were collected in collaboration with the Laboratory of Hepatology (UZ Leuven – KU Leuven) after obtaining informed consent. Freshly isolated primary hepatocytes (donor F125) were obtained from the Hepatocytes and Hepatic Stem Cells Bank from the Cliniques Universitaires St Luc. An agreement from the Belgian Ministry of Health was obtained for the Hepatocytes and Hepatic Stem Cells Bank. Written and signed informed consent has been obtained for collection of the cells.

Lung

Patients with non-small-cell lung cancer were enrolled in an IRB-approved protocol after obtaining informed consent (ClinicalTrials.gov identifier, NCT02095808). Study eligibility included pulmonary masses measuring 1 cm or more in diameter. Standard surgical procedures were followed, with the majority of cases being robotic lobectomies. On the basis of pre-operative imaging and gross inspection at resection, viable fragments of tumour and lung were sampled. Plasma samples from lung cancer patients were drawn primarily from an arterial line throughout the procedure.

Statistical analysis and software

Statistical data analysis was performed using GraphPad Prism 7 (GraphPad Software) on $n \geq 3$ biological replicates. Details of statistical tests and post-tests are presented in the figure legends. Detection of mathematical outliers was performed using Grubb's test. Sample size for all in vitro experiments was chosen empirically. For in vivo experiments, sample size was determined using

power calculations with $\beta = 0.8$ and $P < 0.05$, based on preliminary data. Data are presented as mean ± s.d., or as mean ± s.e.m., as indicated in the figure legends.

3.3 Main

Cancer cells display differential usage of stearoyl-CoA desaturase (SCD)-dependent fatty acid desaturation[96] (Figure 3.2a). To illuminate this plasticity, we treated liver (HUH7), lung (A549 and H460), prostate (DU145) and breast (MDA-MB-468 and T47D) cancer cells with the SCD inhibitor Merck Frosst compound 3j[213], in conditions of low extracellular fatty acid availability. We observed that these different cell lines exhibited a broad sensitivity profile toward SCD inhibition (Fig. 3.1a). On the basis of this proliferation response, we classified these cancer cells as SCD-dependent (inhibition of proliferation, or cell death), partially SCD-dependent (less than 50% proliferation) or SCD-independent (more than 50% proliferation). Next, we excluded the possibility that the differential dependency of cancer cells on SCD activity was a result of their individual growth rate, fatty acid synthesis rate or the degree to which Merck Frosst compound 3j inhibited SCD (Fig. 3.2 b-g). We concluded on the basis of these results that some cancer cells are SCD-independent, which cannot be explained by their known fatty acid metabolism. Consequently, we hypothesized that SCD-independent and partially SCD-dependent cancer cells exploit an alternative desaturation pathway. We reasoned that the presence of such an alternative pathway must result in the synthesis of unusual monounsaturated fatty acids, and therefore measured saturated and monounsaturated C12 to C18 fatty acids. In general, the different cancer cells presented a wide range of total fatty acid abundance, which did not correlate with SCD independence (Fig. 3.2h). Yet, we discovered an elevated abundance of the unusual fatty acid sapienate (*cis*-6-C16:1) in SCD-independent and partially SCD-dependent cancer cells that increased upon SCD inhibition (Fig. 3.1b, Fig. 3.3a).

Sapienate is a major component of human sebum and is to date considered a specific marker of sebocyte metabolism in the sebaceous glands[227,228]. Because sebocytes produce sapienate from palmitate, we determined the desaturation activity from palmitate to sapienate by assessing the sapienate-to-palmitate ratio and sapienate biosynthesis. Both measures increased upon SCD

inhibition in the cell lines we tested, with the exception of SCD-dependent T47D cells (Fig.3.3b,c). Moreover, the sapienate-to-palmitate ratio correlated with SCD independence, and was higher in SCD-independent (HUH7) and partially SCD-dependent (DU145) cancer cells compared to non-transformed cells of the same tissue origin (Fig. 3.1c, Fig. 3.3d). Subsequently, we determined the desaturation activity of palmitate to sapienate in the HUH7 tumour xenografts upon SCD inhibition. Consistent with our in vitro data, we found that SCD inhibition did not significantly alter final tumour weight, but did increase the desaturation activity to sapienate (Fig. 3.1d, Fig. 3.3e). Accordingly, we observed that diethylnitrosamine- and genetically induced mouse hepatocellular carcinoma (HCC) exhibited a significantly elevated desaturation activity to sapienate, as compared to normal liver (Fig. 3.1e,f). These data collectively show that cancer cells, and in particular HCC, can produce sapienate both in vitro and in vivo.

In sebocytes, sapienate is produced by fatty acid desaturase 2 (FADS2)[228] (Fig. 3.2a). Therefore, we investigated whether cancer cells exploit FADS2 to synthesize sapienate. We found that *FADS2* gene expression was increased in SCD-independent and partially SCD-dependent cancer cells, compared to SCD-dependent cells, and in liver and prostate cancer cells upon SCD inhibition (Fig.3.3f,g). Consistently, FADS2 protein expression correlated with SCD independence and desaturation activity to sapienate in cancer cells (Fig. 3.1g,h). Moreover, FADS2 protein and gene expression was elevated in HUH7 and DU145 cancer cells compared to corresponding non-transformed cells (Fig. 3.3h). Similarly, *FADS2* gene expression was increased in matched pairs of cancer versus adjacent non-cancerous tissue of HCC (3 out of 4) and non-small-cell lung cancer (8 out of 10) from human patients (Fig. 3.1i,j). These data suggest an involvement of *FADS2* in sapienate biosynthesis. Accordingly, *FADS2* silencing resulted in a decreased desaturation activity to sapienate in vitro and in vivo (Fig. 3.1k,l and Fig. 3.3i). These findings demonstrate that some cancer cells exploit FADS2 to produce sapienate.

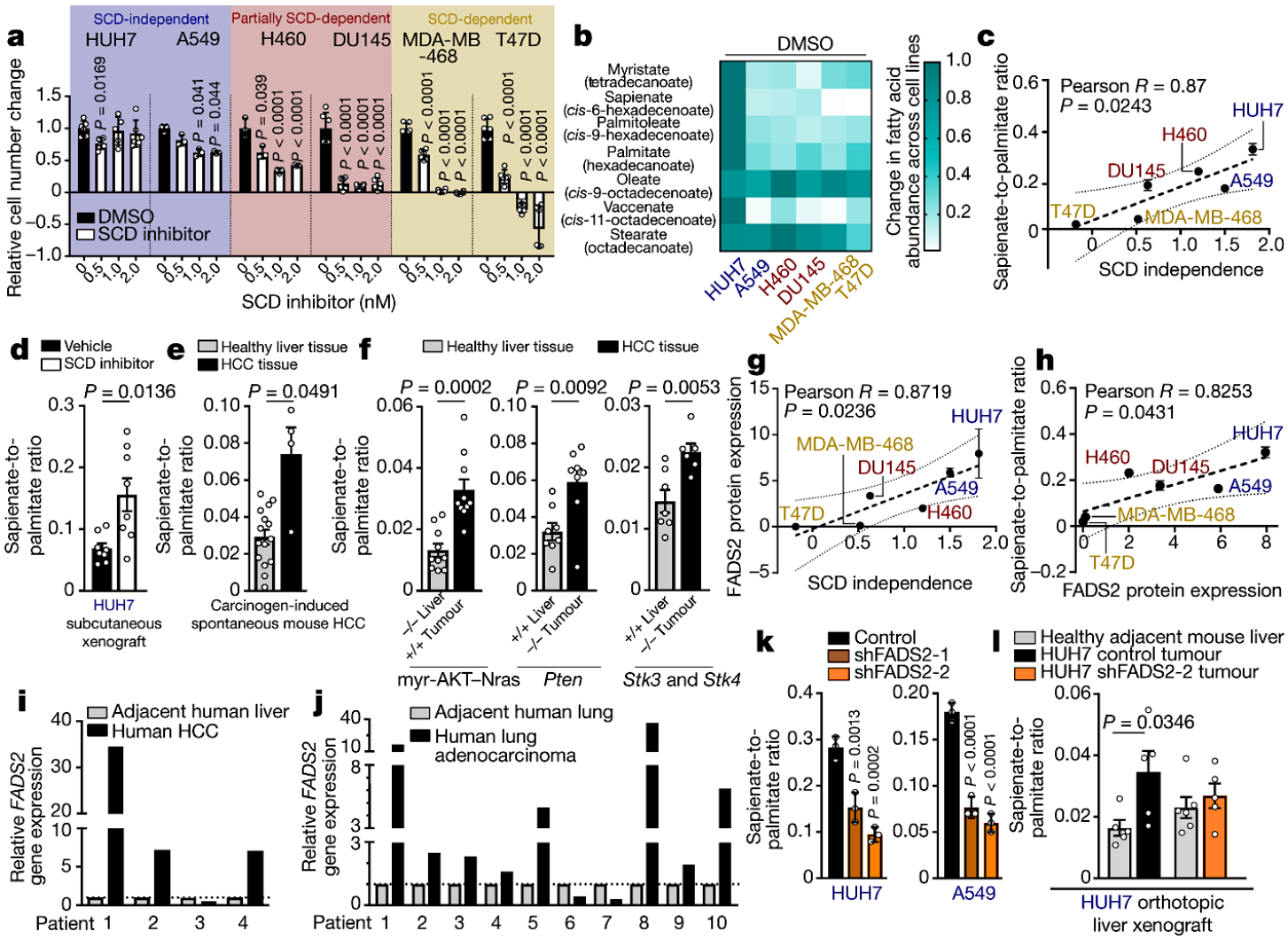

Fig. 3.1: Some cancer cells desaturate palmitate to sapienate via FADS2

a, Sensitivity profile of cancer cells treated with Merck Frosst compound 3j, normalized to control (HUH7, *n* = 6; A459, *n* = 3; H460, *n* = 3; DU145, *n* = 6; MDA-MB-468, *n* = 6; T47D, *n* = 6). Two-way ANOVA with Dunnett's multiple comparisons. **b,** Heat map representing fatty acid abundances normalized to the highest abundance of each fatty acid across all cell lines. Over 90% reduction, white; no reduction, dark green. **c**, Correlation between SCD independence, defined as area under the cell number curve of a, and desaturation activity to sapienate. Trend line (dashed line); 95% confidence intervals (dotted lines). *n* = 3. **d–f**, Sapienate-to-palmitate ratio of HUH7 subcutaneous (s.c.) xenografts in mice treated with vehicle (*n* = 8) or Merck Frosst compound 3j (*n* = 8; 1.5 mg per kg, twice daily with oral (p.o.) gavage) and of HCC in mice induced either with diethylnitrosamine (DEN) or genetically (normal *n* = 15; DEN *n* = 4); myristoylated(myr)-AKT–Nras(*n* = 10), *Pten* (*n* = 8), and *Stk3* and *Stk4* (normal *n* = 7; HCC *n* = 6). Unpaired two-sided Student's *t*-test with Welch's correction. **g, h**, Correlation between FADS2 protein expression and SCD independence or desaturation activity to sapienate. Trend line (dashed line); 95% confidence intervals (dotted lines). *n* = 3**. i, j**, *FADS2* gene expression in paired samples of human HCC (*n* = 4) and non-

small-cell lung adenocarcinoma (n = 10) versus normal adjacent tissue. **k,** Desaturation activity to sapienate in HUH7 and A549 cells with a non-targeting short hairpin RNA (shRNA) or one of two shRNAs targeting *FADS2* (shFADS2-1 and shFADS2-2) (n = 3). One-way ANOVA with Dunnett's multiple comparisons. **l,** Sapienate-to-palmitate ratio in normal adjacent liver and HUH7 orthotopic liver tumours with non-targeting shRNA or an shRNA targeting *FADS2* (shFADS2-2) (n = 5). Two-way ANOVA with Sidak's multiple comparisons. Experiments were performed in low FBS (1%, HUH7; 0.5%, other) with a treatment of 72 h. Error bars represent s.d. (in vitro) or s.e.m. (in vivo) from mean of biologically independent samples (in vitro) or mice (in vivo).

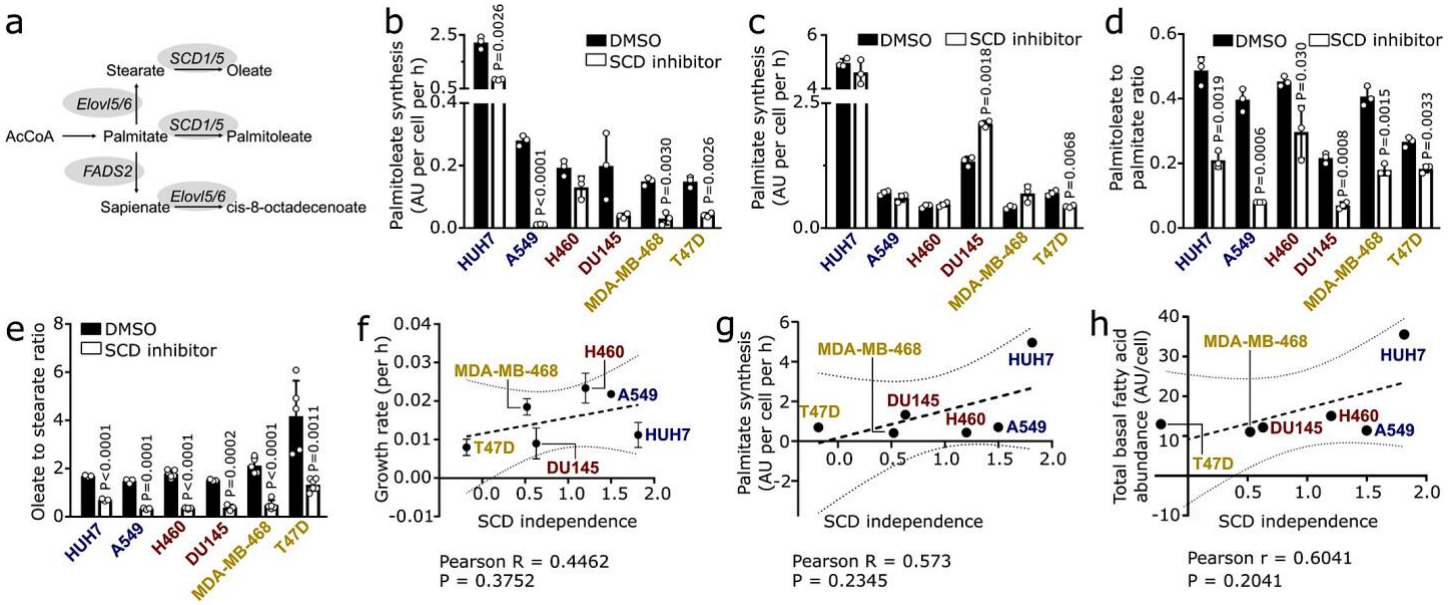

Fig. 3.2: SCD-independent cancer cells produce sapienate.

a, Schematic overview of fatty acid metabolism. AcCoA, acetyl-coenzyme A; SCD1/5, stearoyl-CoA desaturase 1 and 5; Elovl5/6, elongation of very long chain fatty acids protein 5 and 6. **b**–**e**, SCD desaturation activity based on the palmitoleate-to-palmitate ratio, oleate-to-stearate ratio, and palmitoleate and palmitate synthesis upon treatment with Merck Frosst compound 3j (HUH7 and A549, 2 nM; H460 and DU145, 1 nM; MDA-MB-468 and T47D, 0.5 nM; **b**–**d**, n = 3; **e**, HUH7, n = 3; A459, n = 3; H460, n = 6 (control) and n = 4 (SCD inhibitor); DU145, n = 3; MDA-MB-468, n = 5; T47D, n = 5 (control) and n = 6 (SCD inhibitor)). Unpaired two-sided Student's t-tests with Holm–Sidak multiple comparisons. **f**–**h**, Correlation between SCD independence and palmitate synthesis, growth rate or total fatty acid abundance (n = 3). SCD independence was defined as area under the cell number curve of Fig. 3.1a. Palmitate synthesis was derived from e. Trend line (dashed line) and 95% confidence intervals (dotted lines) are depicted. Cancer cell experiments were performed in low FBS DMEM (1%, HUH7; 0.5%, others) with a treatment of 72 h. Error bars represent mean ± s.d. from biologically independent samples.

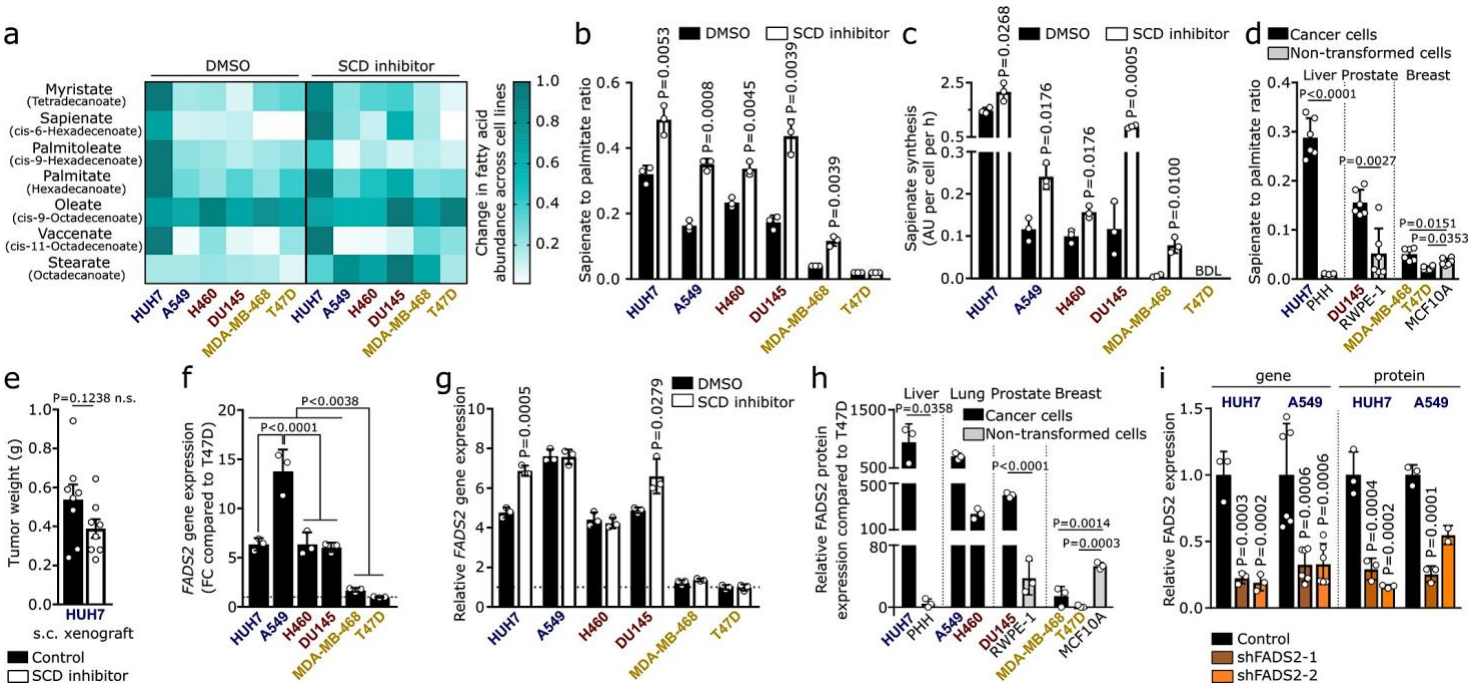

Fig. 3.3: Sapienate is produced via FADS2 in cancer cells.

a, Heat map representing fatty acid abundances with or without treatment with Merck Frosst compound 3j (HUH7 and A549, 2 nM; H460 and DU145, 1 nM; MDA-MB-468 and T47D, 0.5 nM), normalized to the highest abundance of each fatty acid across all cell lines and conditions (Fig. 3.1b). Over 90% reduction, white; no reduction, dark green. **b**, **c**, Desaturation activity to sapienate upon treatment with Merck Frosst compound 3j (HUH7 and A549, 2 nM; H460 and DU145, 1 nM; MDA-MB-468 and T47D, 0.5 nM; *n* = 3). Unpaired two-sided Student's *t*-tests with Holm–Sidak multiple comparisons. **d**, Sapienate-to-palmitate ratio in HUH7 (*n* = 6) versus freshly isolated primary human hepatocytes (PHH; *n* = 3), DU145 (*n* = 6) versus RWPE-1 (*n* = 6) prostate cells, and MDA-MB-468 (*n* = 6) and T47D (*n* = 6) versus MCF10A (*n* = 6) breast cells. Unpaired Student's *t*-tests and Welch's correction (HUH7 versus PHH and DU145 versus RWEP-1); one-way ANOVA with Dunnett's multiple comparisons (MDA-MB-468 and T47D versus MCF10A). **e**, Tumour weight of HUH7 subcutaneous xenografts treated with or without Merck Frosst compound 3j (*n* = 8, one experiment; 1.5 mg per kg twice daily p.o.). Unpaired Student's *t*-test with Welch's correction. **f**, **g**, *FADS2* gene expression in cells with or without Merck Frosst compound 3j, as described in **b** and **c**, normalized to T47D cells (*n* = 3). One-way ANOVA with Tukey's multiple comparisons (**f**); unpaired Student's *t*-tests with Holm–Sidak multiple comparisons (**g**). **h**, FADS2 protein expression in the same conditions as in **d**. Statistics as described in **d**. *n* = 3. **i**, Expression of *FADS2* gene or FADS2 protein in HUH7 and A549 cells upon *FADS2* silencing, normalized to control (gene, HUH7, *n* = 3; A549, *n* = 6; protein, *n* = 3 (except for A549 shFADS2-2, *n* = 2)). One-way ANOVA with Dunnett's multiple comparisons. Cancer cell experiments were performed in low FBS DMEM (1%, HUH7; 0.5%, others) with a treatment of 72 h. Error bars represent s.d. (in vitro) or s.e.m. (in vivo) from mean of biologically independent samples (in vitro) or mice (in vivo).

Next, we investigated whether sapienate biosynthesis causes SCD independence. Sapienate supplementation or *FADS2* overexpression in SCD-dependent MDA-MB-468 cells restored proliferation upon SCD inhibition and thus resulted in SCD independence (Fig. 3.4a,b, Fig. 3.5a). Moreover, *FADS2* silencing combined with SCD inhibition caused the inhibition of proliferation in HUH7 cells and cell death in A549 cells (Fig. 3.4c,d), whereas sole *FADS2* knockdown seemed to increase proliferation in HUH7 cells. These findings indicate that some cancer cells might rely on the metabolic plasticity provided through simultaneous SCD and FADS2 desaturation activity at the expense of maximized proliferation—a phenomenon that has previously been described[229]. Subsequently, we assessed dual inhibition of SCD- and FADS2-dependent desaturation in HUH7 orthotopic liver xenografts. We found that only dual inhibition of SCD and FADS2 resulted in a significantly smaller tumour area compared to control tumours (Fig.3.4e,f). Unlike the *in vitro* results, no full inhibition of tumour growth was achieved in vivo; this was probably due to the lower in vivo knockdown efficiency and a partial compensation through extracellular sapienate uptake (Fig. 3.5b–d). An involvement of linoleate—a known substrate of FADS2 in polydesaturation—in the observed SCD independence was excluded (Fig. 3.5e–h). Taken together, these data demonstrate that dual activity of SCD- and FADS2-dependent desaturation can provide metabolic plasticity that supports proliferation, which can be impaired in vitro and in vivo by the combined inhibition of both pathways.

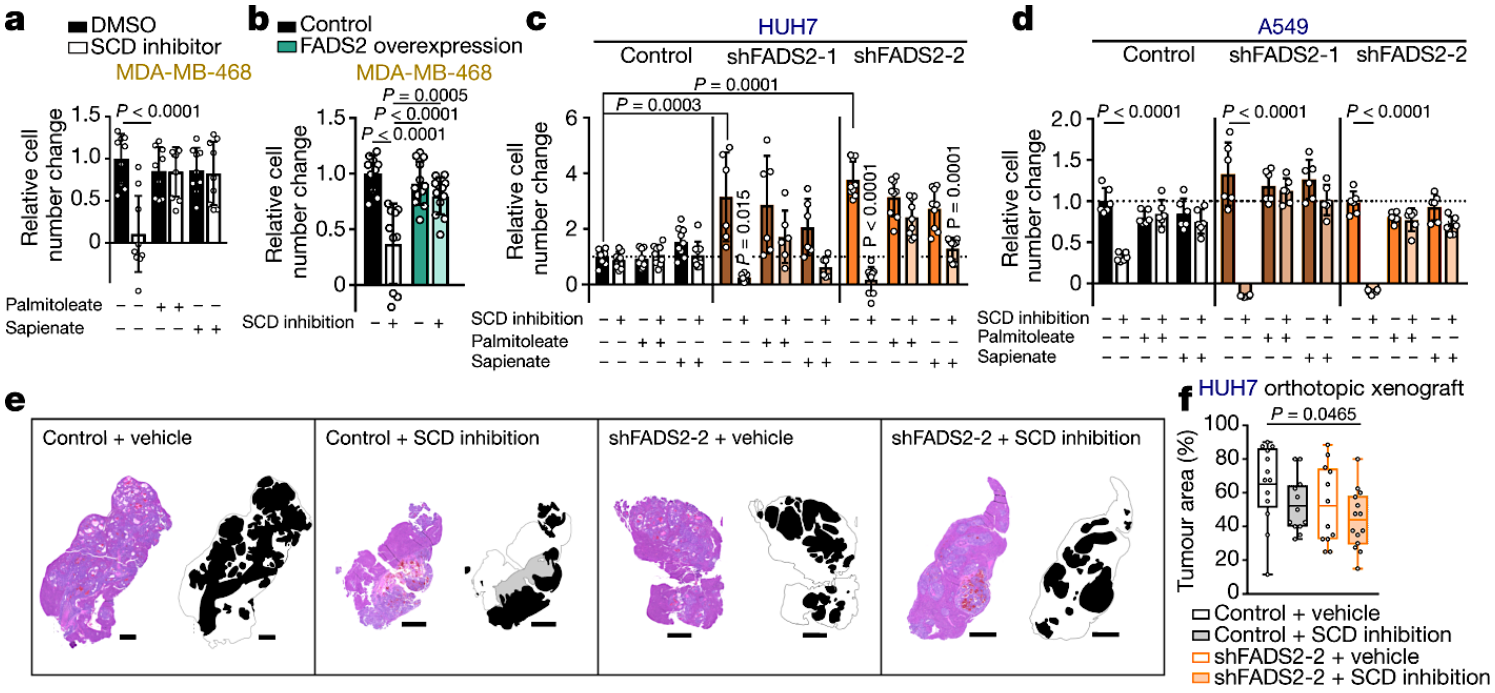

Fig. 3.4: Sapienate synthesis via FADS2 causes independence from the known SCD-catalysed fatty acid desaturation.

a, **b**, Relative proliferation of MDA-MB-468 control (with or without sapienate) and FADS2 overexpression cells upon treatment with 0.5 nM Merck Frosst compound 3j, normalized to control (**a**, *n* = 9; **b**, control *n* = 10, overexpression *n* = 12). Two-way ANOVA with Tukey's multiple comparisons. **c**, **d**, Relative proliferation of HUH7 and A549 cells (with or without sapienate) upon *FADS2* knockdown, with or without 2 nM Merck Frosst compound 3j, normalized to control (**c**, control, *n* = 9; shFADS2-1 *n* = 6; shFADS2-2, *n* = 6; **d**, *n* = 6). Two-way ANOVA with Tukey's multiple comparisons (within different cell lines); one-way ANOVA with Dunnett's multiple comparisons (across different cell lines). Only pairwise comparisons are depicted. **e**, **f**, Representative images of haematoxylin and eosin staining, and relative area of resected tumour nodules derived from HUH7 control (non-targeting shRNA) or *FADS2* knockdown (shFADS2-2) orthotopic liver xenografts in mice, treated with vehicle or Merck Frosst compound 3j (1.5 mg per kg, twice daily p.o.) (control + vehicle, *n* = 13; control + SCD inhibition, *n* = 12; shFADS2-2 + vehicle, *n* = 12, shFADS2-2 + SCD inhibition, *n* = 14 mice, in one experiment). Masks in **e** show the tissue contour, and indicate tumour (black), necrotic (grey) and liver (white) area. Scale bar, 1 mm. Box blots in **f** show box extending from the 25th to 75th percentiles, whiskers indicating the minimum and maximum, and a line indicating the mean. One-way ANOVA with Tukey's multiple comparisons. Experiments were performed in low FBS (1%, HUH7; 0.5%, others) with a treatment of 72 h. Error bars represent s.d. from mean of biologically independent samples (in vitro) or mice (in vivo), unless stated otherwise.

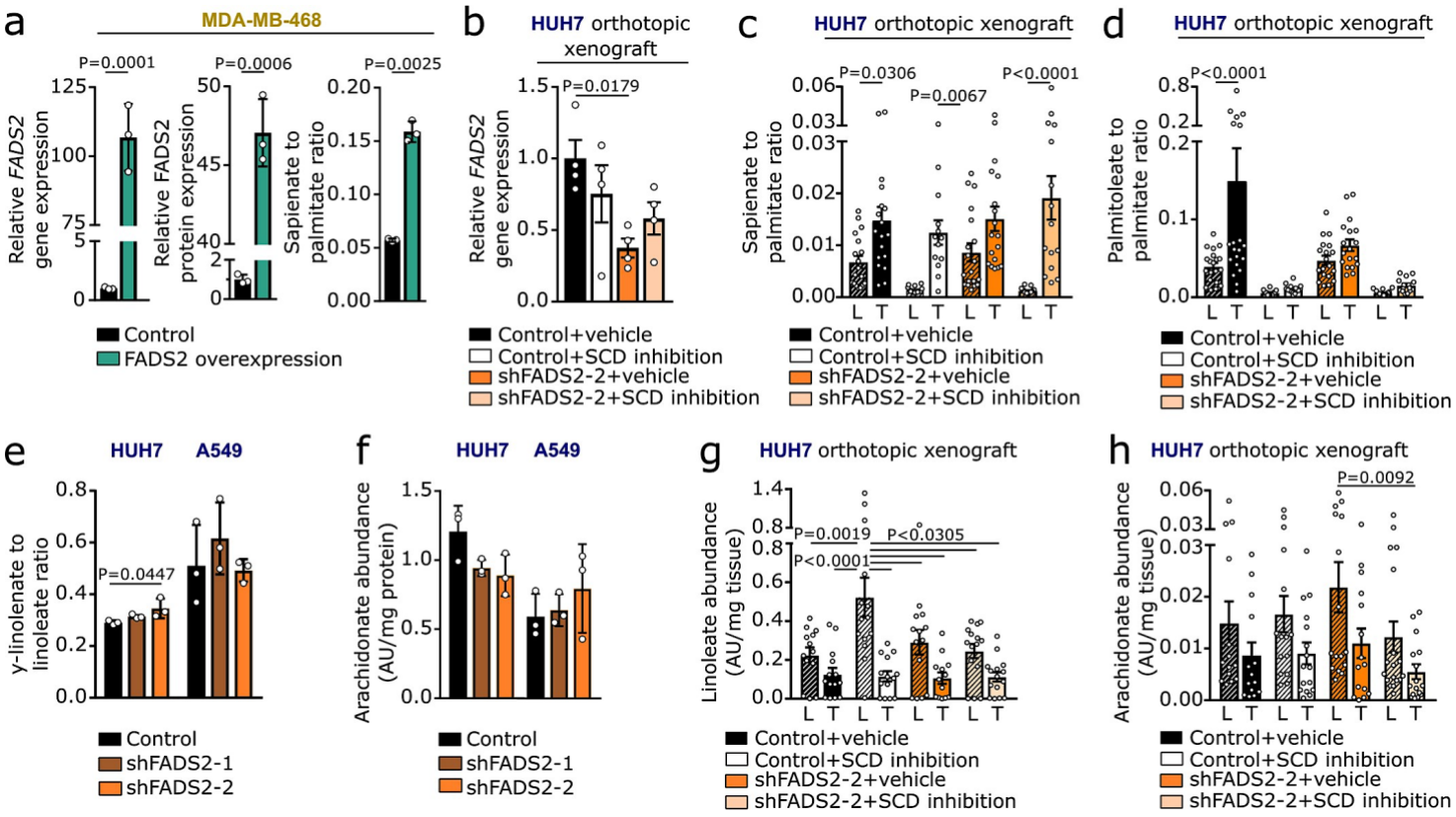

Fig. 3.5: Sapienate rather than arachidonate metabolism causes SCD independence

a, Relative *FADS2* gene or FADS2 protein expression and desaturation activity to sapienate in MDA-MB-468 control and FADS2 overexpression cells with DMSO or 0.5 nM Merck Frosst compound 3j, normalized to control (n = 3). Unpaired two-sided Student's t-test. **b**, Relative *FADS2* gene expression in tumour nodules from HUH7 control or *FADS2* knockdown orthotopic xenografts with vehicle or Merck Frosst compound 3j (1.5 mg per kg twice daily p.o.; n = 4; one experiment), normalized to control. One-way ANOVA with Tukey's multiple comparisons. **c**, **d**, Relative desaturation activity from palmitate to sapienate or palmitoleate in normal adjacent liver (L) and tumour nodules (T), in the same model as described in **f**, normalized to normal liver controls. Control + vehicle (L), n = 18 (**c**) or n = 20 (**d**); control + vehicle (T), n = 18 (**c**) or n = 20 (**d**); control + SCD inhibition (L), n = 14 (**c**, **d**); control + SCD inhibition (T), n = 13 (**c**) or n = 14 (**d**); shFADS2-2 + vehicle (L), n = 19 (**c**, **d**); shFADS2-2 + vehicle (T) n = 18 (**c**, **d**); shFADS2-2 + SCD inhibition (L), n = 15 (**c**) or n = 16 (**d**); shFADS2-2 + SCD inhibition (T), n = 15 (**c**, **d**); two experiments. Two-way ANOVA with Sidak's multiple comparisons. **e**, **f**, Desaturation activity from linoleate to γ-linolenate, on the basis of the γ-linolenate-to-linoleate ratio and arachidonate abundance in HUH7 and A549 control (non-targeting shRNA) and *FADS2* knockdown (using one of two *FADS2* shRNAs) cells (n = 3). One-way ANOVA with Dunnett's multiple comparisons. **g**, **h**, Linoleate and arachidonate abundance in normal adjacent mouse liver and tumour nodules from HUH7 control (non-targeting shRNA) or *FADS2* knockdown (shFADS2-2) orthotopic xenografts treated with vehicle or Merck Frosst compound 3j (1.5 mg per kg twice daily p.o.). Control + vehicle (L), n = 12 (**g**) or n = 14 (**h**); control + vehicle (T), n = 13

(**g**) or *n* = 14 (**h**); control + SCD inhibition (L), *n* = 14 (**g**) or *n* = 15 (**h**); control + SCD inhibition (T) *n* = 14 (**g**) or *n* = 16 (**h**); shFADS2-2 + vehicle (L), *n* = 14 (**g**) or *n* = 16 (**h**); shFADS2-2 + vehicle (T), *n* = 13 (**g**) or *n* = 15 (**h**); shFADS2-2 + SCD inhibition (L), *n* = 15 (**g**) or *n* = 18 (**h**); shFADS2-2 + SCD inhibition (T), *n* = 15 (**g**) or *n* = 16 (**h**); two experiments. Two-way ANOVA with Tukey's multiple comparisons. Cancer cell experiments were performed in low FBS DMEM (1%, HUH7; 0.5%, others) with a treatment of 72 h. Error bars represent s.d. (in vitro) or s.e.m. (in vivo) from mean of biologically independent samples (in vitro) or mice (in vivo).

An important fate of fatty acids is membrane synthesis, for which fatty acids are often elongated. Accordingly, we observed carbons of sapienate in its elongation product *cis*-8-octadecenoate (*cis*-8-C18:1; Fig. 3.7). Consistent with sapienate elongation, the abundance of *cis*-8-octadecenoate was higher in SCD-independent cells than in SCD-dependent cells, increased in HUH7 and A549 cells upon sapienate supplementation or SCD inhibition, and decreased upon *FADS2* silencing (Fig.3.6a,Fig.3.8a-c). Consistently, *cis*-8-octadecenoate supplementation rescued the proliferation of SCD-dependent MDA-MB-468 cells and *FADS2* knockdown cells (HUH7 and A549) upon SCD inhibition (Fig. 3.8d–f). We then determined whether sapienate is used for membrane synthesis. *FADS2* silencing altered the overall composition of membrane-bound phospholipids, decreased the fraction of phospholipids built from sapienate and increased phospholipids built from the SCD product palmitoleate in HUH7 and A549 cells (Fig. 3.6c, Fig.3.9a-e). The opposite change occurred upon SCD inhibition (Fig. 3.6d, e). Functionally, these changes in membrane composition resulted in a trend towards decreased membrane fluidity and increased resistance to lipid peroxidation in *FADS2* knockdown cells (Fig. 3.9f,g). Thus, these data show that some cancer cell lines elongate sapienate and use it for membrane biosynthesis.

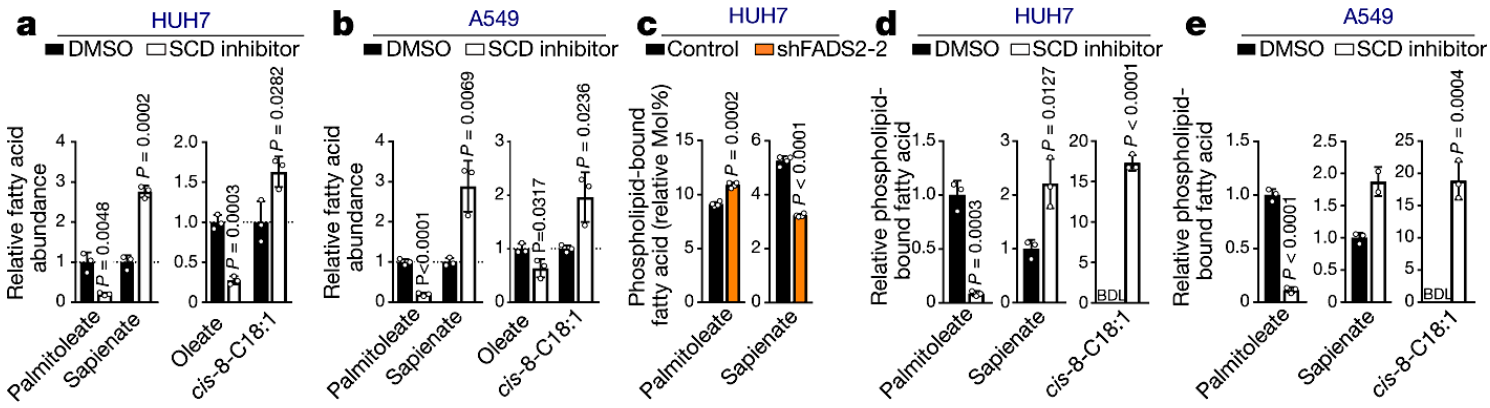

Fig. 3.6: Sapienate and its elongation product *cis*-8-octadecenoate are used in membrane synthesis.

a, **b**, Relative fatty acid abundances in HUH7 and A549 cells treated with 2 nM Merck Frosst compound 3j (*n* = 3). Data are normalized to the respective controls. **c**, Palmitoleate and sapienate abundances in membrane phospholipids in HUH7 cells with non-targeting shRNA and an shRNA targeting *FADS2* (shFADS2-2) (*n* = 4). **d**, **e**, Relative abundances of phospholipid-bound palmitoleate, sapienate and *cis*-8-octadecenoate in HUH7 and A549 cells treated with control or 2 nM Merck Frosst compound 3j, normalized to control (*n* = 2 in **e** sapienate+SCD inhibitor; *n* = 3 in all other cases). BDL, below detection limit. When the respective control was below the detection limit, the data were normalized to the total abundance of all fatty acids measured and are represented in arbitrary units. Experiments were performed in low FBS (1%, HUH7; 0.5%, others) with a treatment of 72 h. Error bars represent s.d. from mean of biologically independent samples. Unpaired two-sided Student's *t*-tests.

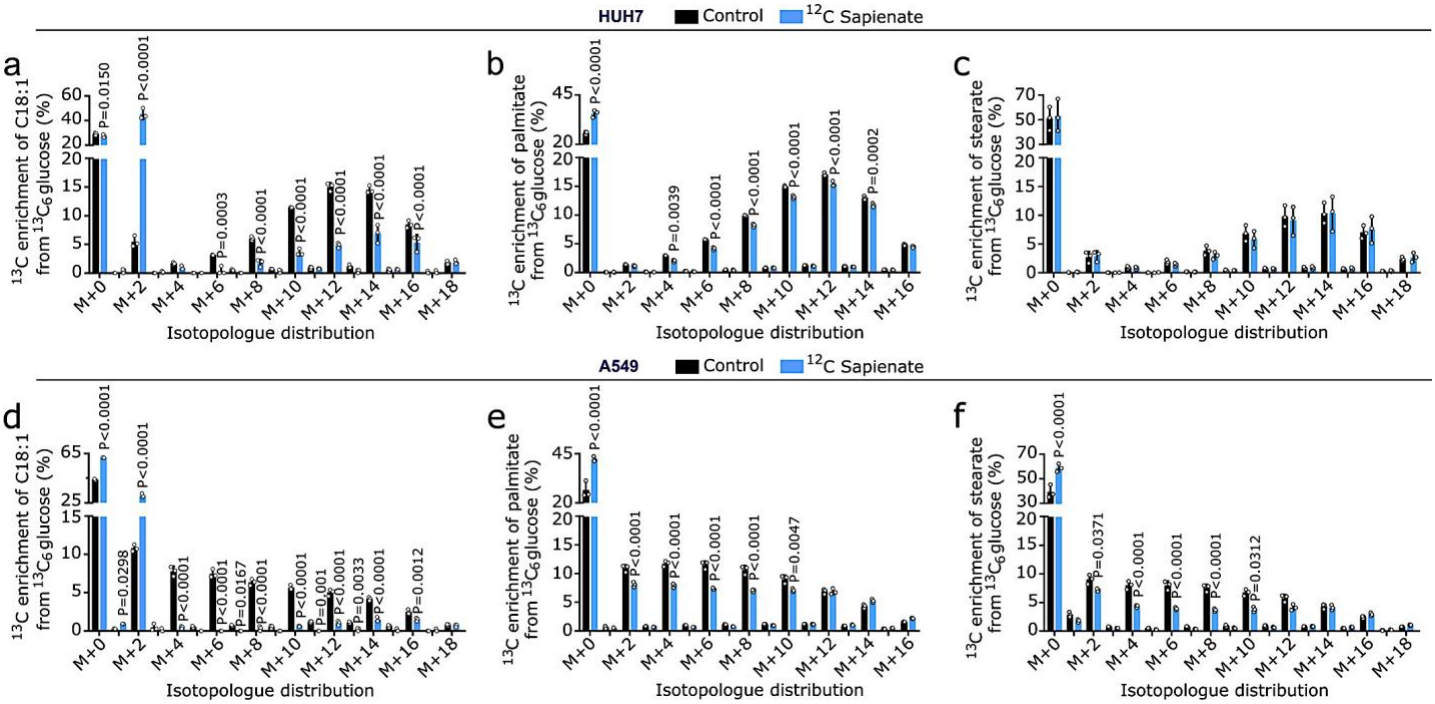

Fig. 3.7: Carbons from sapienate are detected in octadecenoate.

a–**f**, ^{13}C enrichment of palmitate or stearate from $^{13}C_6$-glucose in HUH7 or A549 cells in control conditions (ethanol, black) or upon ^{12}C-sapienate supplementation (blue). Cells were grown in 10% dialysed FBS DMEM containing 4.5 g per l $^{13}C_6$ glucose for 1 week, after which cells were grown for 72 h in 0.5% FBS DMEM containing 4.5 g per l $^{13}C_6$ glucose supplemented with ethanol or 20 µM ^{12}C-sapienate. The purpose of this experiment was to trace the incorporation of carbons from sapienate into *cis*-8-octadecenoate. Palmitate and stearate were measured as controls. Because ^{13}C-labelled sapienate is not commercially available, we performed a reverse labelling in which we pre-labelled HUH7 and A549 cells with $^{13}C_6$-glucose to enrich *cis*-8-octadecenoate with ^{13}C. Then, we supplemented these cells with unlabelled sapienate in the presence of $^{13}C_6$-glucose and determined the ^{13}C enrichment of octadecenoate. If sapienate is elongated to *cis*-8-octadecenoate, we expect a shift in the ^{13}C enrichment from higher to lower octadecenoate isotopologues. We found that supplementation of unlabelled sapienate shifted the ^{13}C enrichment accordingly (**a**, **d**). Moreover, the largest ^{13}C enrichment increase was found in the M + 2 isotopologue, which indicates the elongation of unlabelled sapienate to octadecenoate with ^{13}C-labelled acetyl-CoA. As expected, sapienate supplementation did not change (or only marginally changed) the ^{13}C enrichment of palmitate and stearate (**b**, **c**, **e**, **f**). Unpaired two-sided Student's *t*-tests; *n* = 3. Error bars represent mean ± s.d. from biologically independent samples.

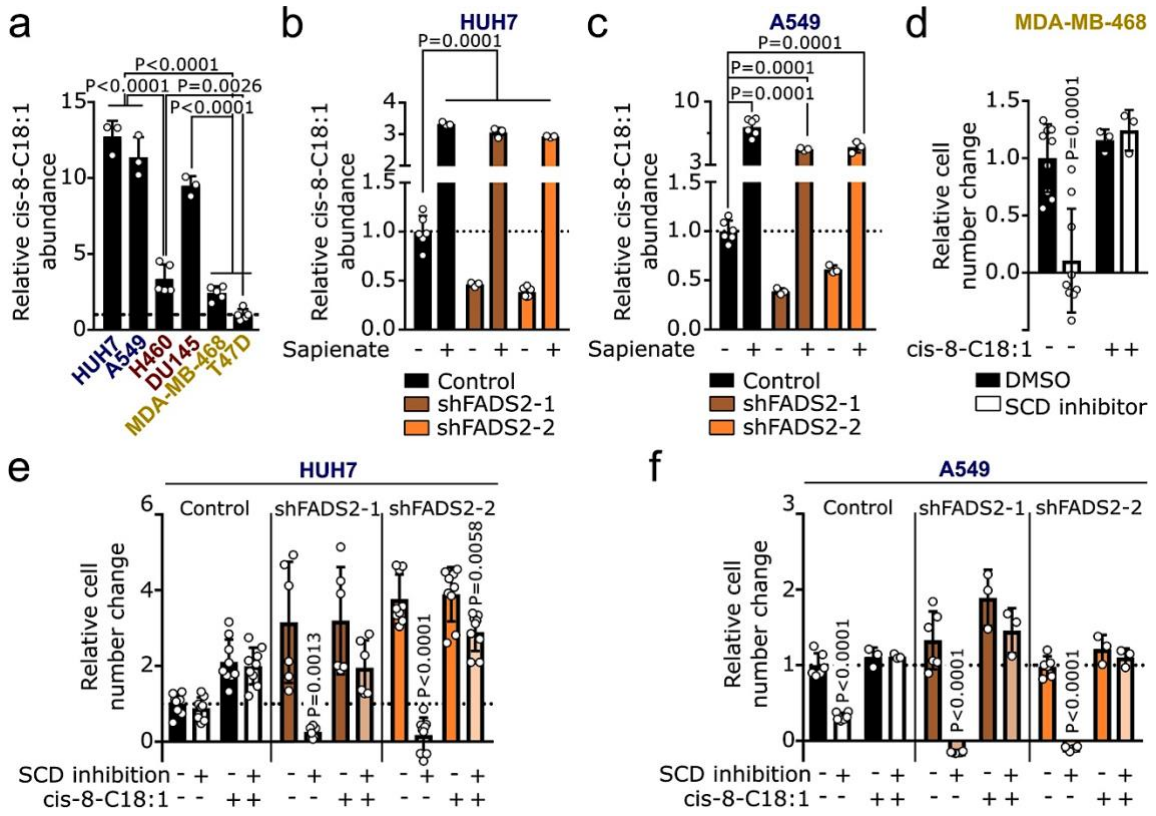

Fig. 3.8: Sapienate is elongated to *cis*-8-octadecenoate

a, Relative *cis*-8-octadecenoate abundance in cancer cells, normalized to T47D cells. HUH7, *n* = 3; A549, *n* = 3; H460, *n* = 5; DU145, *n* = 3; MDA-MB-468, *n* = 5; T47D, *n* = 5. One-way ANOVA with Tukey's multiple comparisons. **b**, **c**, Relative *cis*-8-octadecenoate abundances in HUH7 and A549 control (non-targeting shRNA) and *FADS2* knockdown (one of two *FADS2* shRNAs) cells in control condition (ethanol) or upon supplementation with 20 µM sapienate, normalized to control. HUH7, control, *n* = 6 (ethanol) or *n* = 3 (sapienate); shFADS2-1, *n* = 3; shFADS2-2, *n* = 6 (ethanol) or *n* = 3 (sapienate); A549, control, *n* = 6; shFADS2-1, *n* = 3; shFADS2-2, *n* = 3. Two-way ANOVA with Tukey's multiple comparisons. **d**, Relative proliferation of MDA-MB-468 cells with ethanol (*n* = 9) or 20 µM *cis*-8-octadecenoate (*n* = 3) upon treatment with DMSO or 0.5 nM Merck Frosst compound 3j. Data are normalized to control, with error bars representing s.e.m. Two-way ANOVA with Tukey's multiple comparisons. **e**, **f**, Relative proliferation of HUH7 and A549 control (non-targeting shRNA) and knockdown (shFADS2) cells with ethanol or 20 µM *cis*-8-octadecenoate upon treatment with DMSO or 2 nM Merck Frosst compound 3j. HUH7, control, *n* = 9; shFADS2-1, *n* = 6; shFADS2-2, *n* = 9; A549: EtOH, *n* = 6; *cis*-8-C18:1, *n* = 3. Data are normalized to control. Two-way ANOVA with Tukey's multiple comparisons. Only statistics for pairwise comparisons are depicted. Cancer cell experiments were performed in low FBS DMEM (1%, HUH7; 0.5%, all other cancer cells) with a treatment of 72 h. Error bars represent mean ± s.d. from biologically independent samples, unless otherwise noted.

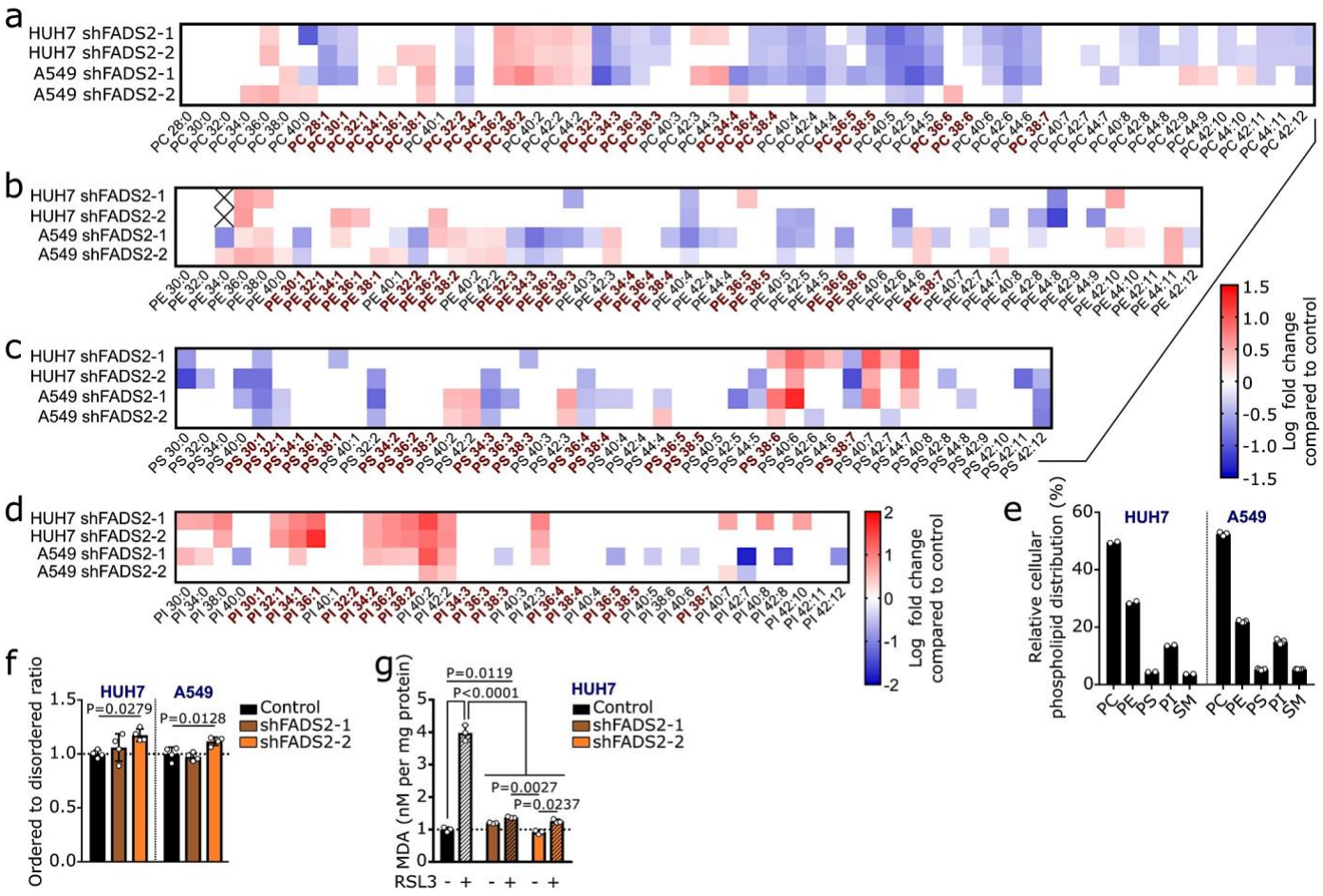

Fig. 3.9: Sapienate and *cis*-8-octadecenoate are used in membranes

a–**d**, Heat map representing abundance changes of phosphatidylcholine (**a**), phosphatidylethanolamine (**b**), phosphatidylserine (**c**) and phosphatidylinositol (**d**) species in control and *FADS2* knockdown HUH7 and A549 cells, relative to control. HUH7, control, *n* = 3; shFADS2-1, *n* = 4; shFADS2-2, *n* = 5; A549, *n* = 5. Only significant differences are depicted as fold change (log_2(change with shRNA versus control)). X, blank or excluded values. Phospholipid species carrying sapienate or palmitoleate are depicted in bold red. Two-way ANOVA with Dunnett's multiple comparisons. **e**, Relative distribution of phospholipid species in HUH7 (*n* = 2) and A549 (*n* = 5) cells with non-targeting shRNA (control). **f**, Membrane fluidity based on the ordered-to-disordered lipid ratio in HUH7 and A549 with a non-targeting shRNA (control, black) or one of two different shRNAs targeting *FADS2* (brown (shFADS2-1) and orange (shFADS2-2)), normalized to control (*n* = 4). The higher the ordered-to-disordered ratio, the more saturated lipids are present in the membrane. One-way ANOVA with Dunnett's multiple comparisons. **g**, Lipid peroxidation sensitivity via MDA assay in HUH7 with a non-targeting shRNA (control; black) or one of two different shRNAs targeting *FADS2* (brown (shFADS2-1) and orange (shFADS2-2)) normalized to control (*n* = 3). Cells were treated with vehicle or 5 µM RSL3, which inhibits glutathione peroxidase 4 and induces lipid peroxidation. Two-way ANOVA with Sidak's multiple comparisons. Cancer cell experiments were performed in low FBS DMEM (1%, HUH7; 0.5%, all other cancer cells) with a treatment of 72 h. Data are presented as mean ± s.d. from biologically independent samples.

Finally, we asked whether sapienate metabolism also occurs in primary human cancers. We measured the ratio of sapienate to palmitate in cancer and normal lung and liver tissue, as well as in blood plasma from human subjects. Blood plasma was obtained from healthy volunteers or patients with cancer, and normal lung and liver was obtained from adjacent non-cancerous tissue from patients with cancer and non-transplanted donor organs, respectively. In addition, we determined the palmitoleate-to-palmitate ratio in the same tissues and blood plasma samples as a readout of the SCD-dependent fatty acid desaturation pathway. We found that in cancer tissue, but not in normal tissue, the sapienate-to-palmitate ratio was significantly increased compared to the ratio in blood plasma (Fig.3.10a,b). Accordingly, the sapienate-to-palmitate ratio was higher in cancer tissue than in normal tissue (Fig.3.10a,b). The increase in the sapienate-to-palmitate ratio was more pronounced than the corresponding change in the palmitoleate-to-palmitate ratio when comparing cancer and normal tissue (Fig.3.10a,b). This suggests a specific increase in sapienate biosynthesis in these cancers, rather than a general increase in the synthesis of monounsaturated fatty acids. Taken together, these data provide evidence that sapienate metabolism occurs in vivo in primary lung and liver carcinomas from human patients.

The well-characterized SCD-dependent fatty acid desaturation pathway has previously been considered to be the only source of de novo-generated monounsaturated fatty acids in cancer cells[230]. Here we show that cancer cells can rewire their fatty acid metabolism and desaturate palmitate to the unusual fatty acid sapienate (Fig.3.10c). Particularly, we find evidence for sapienate metabolism in human lung and liver carcinoma. This finding can explain metabolic plasticity, and demonstrates heterogeneity in the fatty acid desaturation metabolism of cancer cells. Although we find that sapienate and *cis*-8-octadecenoate can support membrane synthesis, it is tempting to speculate that sapienate and its elongation products affect the known fatty acid and lipid signalling networks of cancer cells[231–233]. Consequently, this could provide cancer cells with a hitherto unexplored possibility to deregulate signalling networks, opening new opportunities to understand and target them. In conclusion, our discovery increases the current understanding of fatty acid metabolism in cancers and suggests sapienate biosynthesis as an alternative source of monounsaturated fatty acids.

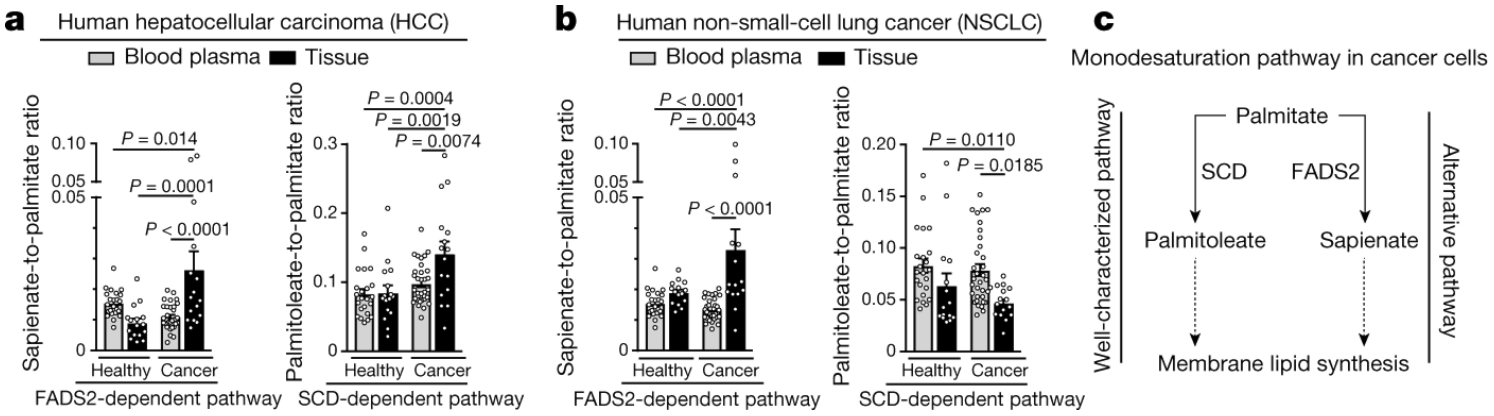

Fig. 3.10: Evidence for sapienate synthesis in primary human cancers

a, Sapienate-to-palmitate and palmitoleate-to-palmitate ratios in HCC and normal liver tissue, as well as in blood plasma from humans. Blood plasma was from healthy volunteers or patients with liver cancer, and normal liver was adjacent non-cancerous tissue from patients with liver cancer and non-transplanted donor livers (healthy, blood plasma $n = 23$ and tissue $n = 16$; cancer, blood plasma $n = 33$ and tissue $n = 16$). Notably, blood plasma ratios from healthy volunteers are the same as in b. **b**, Sapienate-to-palmitate and palmitoleate-to-palmitate ratios in lung cancers and normal lung tissue, as well as in blood plasma from humans. Blood plasma was from healthy volunteers or patients with cancer, and normal lung was adjacent non-cancerous tissue from patients with cancer (healthy, blood plasma $n = 23$ and tissue $n = 15$; cancer, blood plasma $n = 34$ and tissue $n = 15$). Notably, blood plasma ratios from healthy volunteers are the same as in **a**. **c**, Sapienate metabolism is an alternative monodesaturation pathway. Two-way ANOVA with Tukey's multiple comparisons. Error bars represent s.e.m. of mean from different individuals.

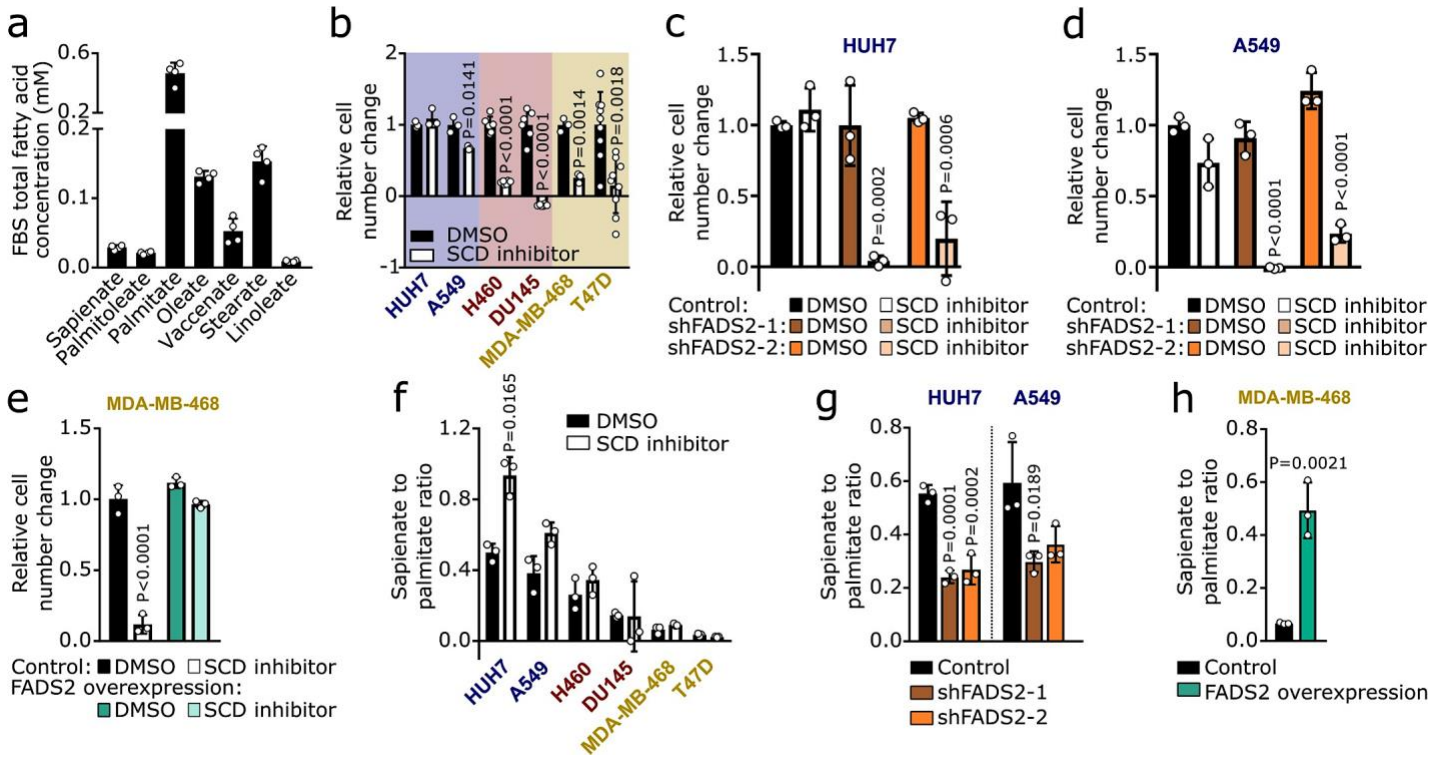

Fig. 3.11: SCD independence and sapienate metabolism occur in medium with glucose and amino acid concentrations that are similar to physiological conditions.

a, Fatty acid concentrations of fetal bovine serum (FBS; *n* = 4). Low FBS conditions (0.5–1% FBS) correspond to a total fatty acid concentration of 4.31–8.62 µM. **b**, Sensitivity profile of cancer cells to Merck Frosst compound 3j (white; HUH7 and A549 2 nM; H460 and DU145, 1 nM; MDA-MB-468 and T47D, 0.5 nM) in BLM , normalized to control. HUH7, *n* = 3; A549, *n* = 3; H460, *n* = 6; DU145, *n* = 6, MDA-MB-468, *n* = 3; T47D, *n* = 9. Two-way ANOVA with Dunnett's multiple comparisons. **c**, **d**, Sensitivity profile of HUH7 and A549 control (non-targeting shRNA, black) and knockdown (shFADS2, (brown (shFADS2-1) and orange (shFADS2-2)) cells treated with DMSO (dark bars) or 2 nM Merck Frosst compound 3j (light bars) in BLM12·13, normalized to control (*n* = 3). Two-way ANOVA with Holm–Sidak multiple comparisons. **e**, Sensitivity profile of MDA-MB-468 control (black) and *FADS2* overexpression (green) cells treated with DMSO (dark bars) or 0.5 nM Merck Frosst compound 3j (light bars) in BLM12·13, normalized to control (*n* = 3). Two-way ANOVA with Holm–Sidak multiple comparisons. **f**, Desaturation activity to sapienate based on the sapienate-to-palmitate ratio in cancer cells, in conditions as described in **b**. *n* = 3. Unpaired two-sided Student's *t*-tests with Holm–Sidak multiple comparisons. **g**, **h**, Desaturation activity from palmitate to sapienate based on the sapienate-to-palmitate ratio, in the same conditions as described in **c–f**. *n* = 3. One-way ANOVA with Dunnett's multiple comparisons (**g**); unpaired Student's *t*-test (**h**). Cancer cell experiments were performed in low FBS BLM (1%, HUH7; 0.5%, all other cancer cells) with a treatment of 72 h. Data are presented as mean ± s.d. from biologically independent samples.

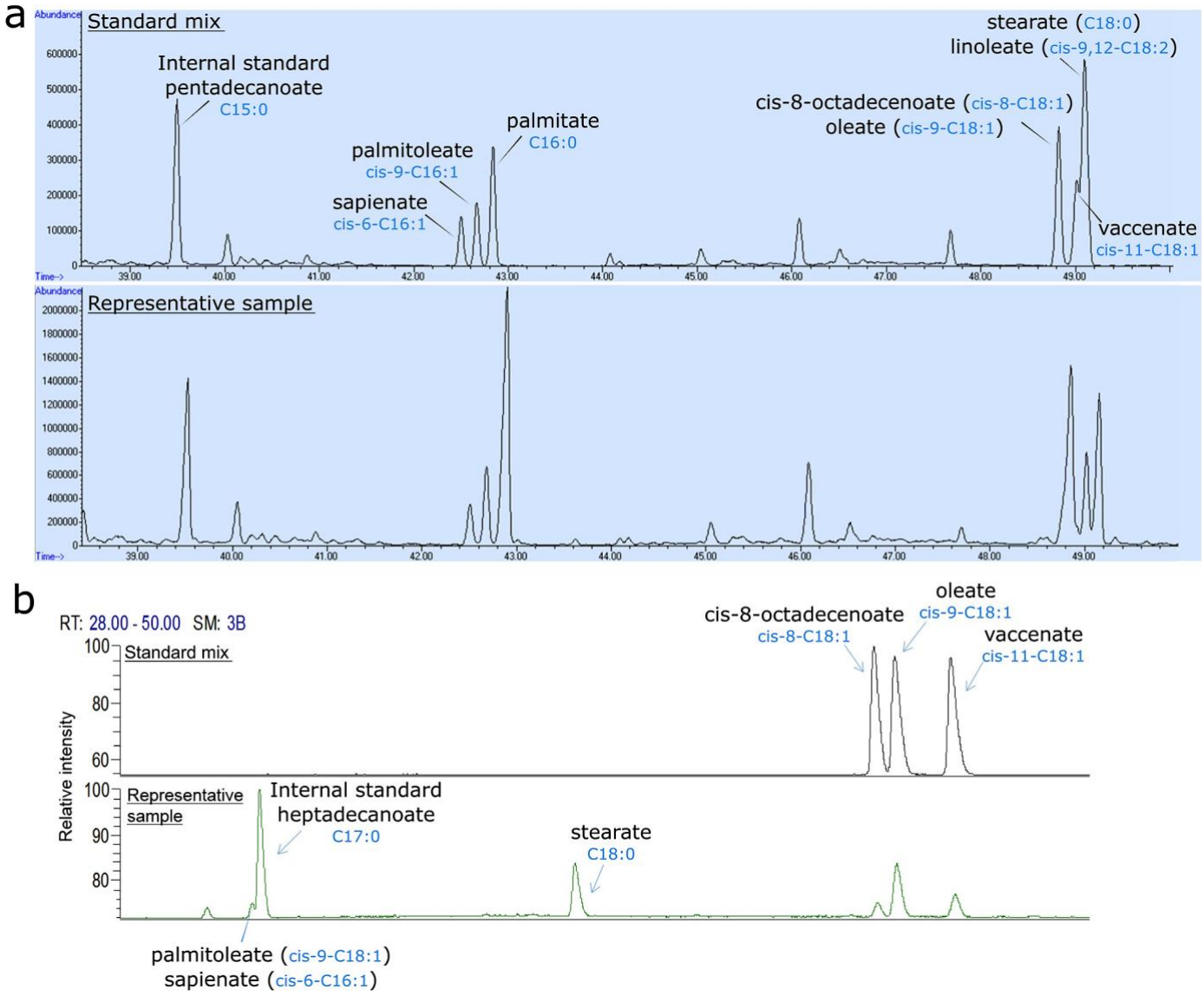

Fig. 3.12: Separation and detection of sapienate and *cis*-8-octadecenoate

a, Separation and detection of sapienate (*cis*-6-hexadecenoate) and palmitoleate (*cis*-9-hexadecenoate) via GC–MS. Separation was optimized using a standard mix, containing pentadecanoate, sapienate, palmitoleate, palmitate, *cis*-8-octadecenoate, oleate, vaccinate, linoleate and stearate (top), and the method was subsequently validated by measurement of these fatty acids in biological samples. Bottom, a representative biological sample. **b**, Separation and detection of *cis*-8-octadecenoate, oleate (*cis*-9-octadecenoate) and vaccinate (*cis*-11-octadecenoate) via GC–FID. Separation was optimized using a standard mix containing *cis*-8-, *cis*-9- and *cis*-11-octadecenoate (top), and the method was subsequently validated by measurement of these fatty acids in biological samples. Bottom, a representative biological sample.

Chapter 4: GBM tumors are heterogeneous in their fatty acid metabolism and modulating fatty acid metabolism sensitizes cancer cells derived from recurring GBM tumors to temozolomide

4.1 Abstract

Glioblastoma is a highly lethal grade of astrocytoma with very low median survival. Despite extensive efforts, there is still a lack of alternatives that might improve these prospects. We uncovered that the chemotherapeutic agent temozolomide impinges on fatty acid synthesis and desaturation in newly diagnosed glioblastoma. This response is, however, blunted in recurring glioblastoma from the same patient. Further, we describe that disrupting cellular fatty acid homeostasis in favor of accumulation of saturated fatty acids such as palmitate synergizes with temozolomide treatment. Pharmacological inhibition of SCD and/or FADS2 allows palmitate accumulation and thus greatly augments temozolomide efficacy. This effect was independent of common GBM prognostic factors and was effective against cancer cells from recurring glioblastoma. In summary, we provide evidence that intracellular accumulation of saturated fatty acids in conjunction with temozolomide based chemotherapy induces death in glioblastoma cells derived from patients.

4.2 Introduction

Glioblastoma (GBM) is the most common adult diffuse glioma but unfortunately also one of the most difficult to treat cancer types. Despite an intensive treatment regimen consisting of surgical resection followed by radiotherapy with concomitant and adjuvant temozolomide[234], the median survival ranges between 15-16 months with 5-year survival rate of only ~5% [140,153]. Temozolomide (TMZ) induces GBM cell death via introducing DNA methylation on purine bases and its efficacy is heavily influenced by molecular factors such as O-6-Methylguanine-DNA Methyltransferase (MGMT) promoter methylation with patients having higher methylation showing better response. Moreover, resistance to TMZ, particularly in recurring tumors interferes with its efficacy[235].

Several studies have revealed that perhaps the most significant contributor to GBM treatment resistance is the inherent inter- and intra-tumoral heterogeneity [236]. Verhaak *et al* and Phillips *et al* defined the existence of 3 distinct GBM subtypes: proneural, mesenchymal and classical, each defined by a specific gene signature [156,157]. Moreover, several studies that used a multi-sampling technique have shown that at least two of the TCGA-derived genomic subtypes of GBM can appear within the same tumor [166,237]. Subsequently, single-cell based analyses have been used to demonstrate cellular heterogeneity in GBM [164,238,239]. Current theories postulate that intra-tumoral heterogeneity can arise from clonal evolution, presence of stem cells and microenvironmental interactions [240]. The latter also includes metabolic interactions. Several studies have shed light on the altered fatty acid (FA) metabolism of GBM cancer cells [241–244]. These tumors display an increased rate of fatty acid synthesis, mostly attributed to an increase in sterol response element binding protein (SREBP) mediated gene expression[245–247]. Further, GBM cells have elevated stearoyl coA desaturase (SCD) activity. In preclinical studies, SCD inhibition reduces growth of GBM tumors alone or in combination with chemotherapy[66,67]. Wang *et al* demonstrated that fatty acid desaturase 2 (FADS2) inhibition in combination with radiotherapy reduced growth of U87 xenografts in nude mice[248]. In addition, inhibition of FADS2 as well as fatty acid elongase 2 (Elovl2), has been demonstrated to curb the growth of glioma stem cells[249]. Ferraro *et al* recently reported that breast cancer cells metastasizing to the brain upregulate the expression of fatty acid synthetase (FASN), the inhibition of which significantly curbed metastases formation[250]. However, the extent of lipid metabolism heterogeneity and its role in disease recurrence is yet to be explored.

In this study, we deconvolute the role of fatty acid metabolism in GBM heterogeneity, treatment and recurrence. Using single cell sequencing data of glioblastoma tissue from patients, we observed that the expression of *FASN*, *SCD* and *FADS2* correlated with distinct cell fates within the cancer cell cluster. We further found that the chemotherapeutic agent temozolomide (TMZ) resulted in a reduction of activities of all these enzymes only in newly diagnosed but not matching recurrent and TMZ-resistant patient-derived glioblastoma cells. Subsequently, we show that recurrent patient-derived glioblastoma cells can be re-sensitized to TMZ either by supplementing the fatty acid palmitate to media or by targeting SCD or FADS2.

4.3 Methods

Single-cell RNA sequencing data pre-processing, clustering, and cancer sub-cluster analysis

After quality control, raw sequencing reads were aligned to the human reference genome GRCh38 and processed to a matrix representing the UMI's per cell barcode per gene using CellRanger (10x Genomics, v2.0). Raw gene expression matrices generated per sample were merged and analysed with the Seurat package (v2.3.4). Matrices were filtered by removing cell barcodes with < 401 UMIs, < 200 expressed genes, > 6000 expressed genes or > 20% of reads mapping to mitochondrial RNA. The remaining cells were normalized and genes with a normalized expression between 0.125 and 3, and a quantile-normalized variance > 0.5 were selected as variable genes. When clustering cell types, we regressed out confounding factors: number of UMIs, percentage of mitochondrial RNA, patient ID and cell cycle (S and G2M phase scores calculated by the CellCycleScoring function in Seurat). After regression for confounding factors, all variably-expressed genes were used to construct principal components (PCs) and PCs covering the highest variance in the dataset were selected. The selection of these PCs was based on elbow and Jackstraw plots. Clusters were calculated by the FindClusters function with a resolution between 0.2 and 2 and visualised using the UMAP dimensional reduction method. Differential gene-expression analysis was performed for clusters generated at various resolutions by both the Wilcoxon rank sum test and Model-based Analysis of Single-cell Transcriptomics (MAST) using the FindMarkers function. A specific resolution was selected when known cell types were identified as a cluster at a given resolution, but not at a lower resolution, with the minimal constraint that each cluster has at least 10 significantly differentially expressed genes (FDR < 0.01 with both methods) with at least a 2-fold difference in expression compared to all other clusters. Annotation of the resulting clusters to cell types was based on the expression of marker genes. All major cell types were identified in one clustering step. The cancer cell cluster, comprising a total of 17,649 cells, could be divided into 12 distinct sub-clusters, SC: 3, 6, 7, 8, 11, 12, 13, 15, 17, 21, 23 and 24 (Figure 1b). Sub-cluster 21 was removed from subsequent analyses, as it contained only one cell. Sub-clusters 3/12/23/24 were also removed from subsequent analyses, since over 75% of the cells in them were contributed by a single patient, as was sub-cluster 13, for which 85% of the cells were contributed by two patients only, rendering the corresponding

sub-clusters patient-specific. Out of the remaining sub-clusters, we identified cluster 15 as a potential low-quality cell cluster, based on the substantially lower library size (nUMI, UMI counts) and number of detected genes (nGene) in the cells comprising it, relative to all other sub-clusters, and therefore removed it too from all subsequent analyses. Consequently, five cancer cell sub-clusters (6, 7, 8, 11, 17) were further analyzed.

Cancer sub-cluster classification and glioblastoma meta-module score calculation

Cells present in either of the remaining 5 cancer cell sub-clusters were first examined as a whole to assess the degree of metabolic heterogeneity within the cancer cell population. For this, standardized variances were determined, across all cells in these clusters, for all genes in the data set. This was achieved using Seurat's FindVariableFeatures function with the "vst" selection method. Genes were then ranked based on their standardized variances, and the resulting ranked gene list was used as input for gene-set enrichment analysis (GSEA). GSEA was performed using the Multilevel method implemented in the R package fgsea (v1.20), with 10,000 permutations and a p-value calculation boundary (eps) of 0. Normalized enrichment scores (NES), representing in this case the degree of heterogeneity for the corresponding gene sets, were determined for a manually assembled collection of 7 gene sets. The latter were built based on the KEGG gene-set collection provided in the R package gage (v2.44.0). They consisted of a global metabolism gene set (ALL METABOLISM), comprising all genes present in any of KEGG's metabolic pathways, as well as 5 extra gene sets containing all genes present in pathways belonging to either of the following KEGG subcategories: Carbohydrate metabolism, Energy metabolism, Lipid metabolism, Nucleotide metabolism, and Amino acid metabolism. An additional gene set containing all metabolic genes not represented in either of these 5 subcategories (Other Metabolism) was also included.

The 5 cancer cell sub-clusters (6, 7, 8, 11, 17) were then classified according to their average gene expression levels of *SCD*, *FADS2* and *FASN*. For this, the raw count matrix was subset to these 5 sub-clusters, and further normalized to units of counts per 100k reads (CP100k) for each cell, by dividing the UMI counts for every gene in each cell by the total UMI counts for that cell, and then multiplying times 10^5. Average normalized expression levels for SCD1, FADS2 and FASN for each sub-cluster were then converted into Z-Scores as:

$$Z_{g,SC} = \frac{\overline{E}_{g,SC} - \mu(\overline{E}_g)}{\sigma(\overline{E}_g)}$$

where $\overline{E}_{g,SC}$ is the average normalized expression level for gene g in sub-cluster SC, while $\mu(\overline{E}_g)$ and $\sigma(\overline{E}_g)$ are respectively the mean and standard deviation of $\overline{E}_{g,SC}$ among all sub-clusters.

Enrichment scores for publicly available gene meta-modules identifying known glioblastoma cell states or fates [5] were determined using the GSVA (gene set variation analysis) package [251]. In brief, the raw count matrix was subset to the 5 sub-clusters of interest and was first subject to size-factor and variance-stabilizing normalization using Monocle. GSVA scores were then determined using default parameters (particularly a Gaussian kernel for cumulative density function estimation, as the input expression matrix is already log-normalized by virtue of the variance stabilization) for a publicly available set of gene meta-modules identifying known glioblastoma cell states or fates [238]. GSVA scores were then averaged over all cells belonging to every given sub-cluster, and these average GSVA scores were further converted (for plotting purposes) into Z-Scores as:

$$Z_{m,SC} = \frac{\overline{S}_{m,SC} - \mu(\overline{S}_m)}{\sigma(\overline{S}_m)}$$

where $\overline{S}_{m,SC}$ is the average GSVA score for the gene meta-module m in sub-cluster SC, while $\mu(\overline{S}_m)$ and $\sigma(\overline{S}_m)$ are respectively the mean and standard deviation of $\overline{S}_{m,SC}$ among all sub-clusters.

Cell lines, cell culture and chemicals

Human GBM cells U87 IDH WT, U87 IDH R132H U251, LN18 and U118 were obtained from ATCC and cultured in Dulbecco's modified Eagle's medium (DMEM) with glutamax and pyruvate (Life Technologies) supplemented with 10% heat-inactivated fetal bovine serum (Life Technologies), 1% penicillin (Life Technologies) and 1% streptomycin (Life Technologies). Human adenocarcinoma A549 and human hepatocellular carcinoma HUH7 cells were cultured in DMEM (Life Technologies) supplemented with 10% heat-inactivated fetal bovine serum (Life Technologies), 1% penicillin (Life Technologies) and 1% streptomycin (Life Technologies). Patient-derived GBM cell lines were generated in-house as described below. All cell lines were confirmed

to be mycoplasma free, based on routine testing using the MycoAlert Mycoplasma Detection Kit (Lonza).

For MS experiments low serum conditions (0.5% FBS for A549 and 1% FBS for others) were applied. 13C6-glucose (CLM-1396 Cambridge Isotope Laboratories) was used for labeling experiments. Merck Frosst Cpd 3j [27]was used as an SCD inhibitor. The fatty acids sodium palmitate, stearic acid, palmitoleic acid, oleic acid, cis-vaccenic acid and linolenic acid were purchased from Sigma-Aldrich. Linoleic acid, arachidonic acid, docosahexaenoic acid and γ-linolenic acid were purchased form Cayman chemical. Sapienate (hexadecenoic acid cis-6) was purchased from Matreya LLC. Solvents for metabolite extraction and mass spectrometry were HPLC grade from Sigma-Aldrich.

Temozolomide, 5-azacytidine, 4μ8C (IRE1 inhibitor), GSK2606414 (PERK inhibitor), Vitamin E and aminotriazole were purchased from Sigma-Aldrich. CellEvent™ Caspase-3/7 Green Detection Reagent and Sytox Green were purchased from Life Technologies.

Generation of patient-derived GBM cell lines

Patient-derived cell lines were generated either from freshly resected tumors tissue or from frozen dissociated tissue.

Generation from fresh tumors: Tissue was obtained from patients undergoing surgical resection at UZ Gasthuisberg, Leuven (Belgium) with informed consent (S59804). Tumor tissue was cut into small pieces (1-2mm) and enzymatically dissociated using the MACS Brain Tumor Dissociation Kit (P) (Miltenyi Biotech). Small pieces of tissue were transferred into gentleMACS^{TM} C Tubes (Miltenyi Biotec) containing Buffer X (3890 μl) that was pre-heated at 37°C for 10-15 minutes. As per manufacturer's instructions, Enzyme N (50μl), Buffer Y (40μl), and Enzyme A (20μl) were added to the C tubes and gently mixed. The gentle MACS programs "h_tumor_02", "h_tumor_03", and "m_brain_01" were run, interspersed with incubation at 37°C for 15 and 10 minutes, respectively. The dissociated sample was passed through a 70μM strainer to remove cell clumps and debris. After centrifugation, the pellet was resuspended with 1 ml ACK lysing buffer (Life Technologies) to remove red blood cells and incubated for 1 min at 37°C. The reaction

was stopped by adding 8ml of pre-heated NSA medium (Stem Cell Technologies). Cells were then re-centrifuged, aspirated and resuspended in fresh NSA medium. The cells were seeded onto laminin-coated flasks and maintained as described below.

Generation from frozen dissociated tumors: Dissociated tumor tissue was obtained from the Center of human genetics, KU Leuven (Belgium) (S61081). Vials with frozen aliquots of dissociated cells were thawed for 2 minutes in a 37°c water bath. Next, the cell suspension was transferred to a 15 ml centrifuge tube containing 9ml pre-heated NSA medium and centrifuged for 5 minutes at 300g. The cell pellets were resuspended in NSA medium, seeded onto laminin-coated flasks and maintained as described below.

Patient-derived GBM cell lines culture

Patient-derived GBM cell lines were cultured in reconstituted human NeuroCult™ NS-A Proliferation kit (Stem Cell Technologies) supplemented with 20µg/ml heparin sodium salt (Stem Cell Technologies), 20ng/ml rhEGF (Peprotech), 20ng/ml b-FGF (Peprotech) and 1% antibiotic/antimycotic (Life Technologies). Flasks or plates were coated with 5µg/ml laminin freshly prepared by diluting 1mg/ml laminin solution (Sigma Aldrich) in dPBS. The flasks/plates were then incubated at 37degrees for atleast 1hour. For seeding cells, laminin was aspirated and fresh medium added immediately. For maintenance, cells were scraped off and re-plated into laminin coated flasks. Accutase **(**Life Technologies**)** was used to dissociate neurospheres and to obtain a single cell suspension, when required. All cell lines were confirmed to be mycoplasma free, based on routine testing using the MycoAlert Mycoplasma Detection Kit (Lonza).

Temozolomide treatment

Patient-derived GBM cells were prepared into a single-cell suspension, seeded in laminin-coated 12-well or 6-well plates (Corning) and grown in a humidified environment at 37 °C with 5% CO_2. After 24 h, the medium was aspirated, cells were washed with dPBS, and replaced with medium containing 250µM TMZ or 0.25% DMSO as control and incubated for 6 days.

Fatty acid conjugation

10% BSA solution was prepared by dissolving bovine serum albumin in NSA medium (Stem Cell Technologies) without supplements. Next, this solution was incubated in a water bath at 37 °C until completely dissolved and then sterile-filtered using a 0.2 micron filter. In the meantime, 100mM stocks of fatty acids were prepared in 50% ethanol (sodium palmitate) or 100% ethanol (all other fatty acids). Subsequently, these were diluted in 10% BSA to obtain 2mM sodium palmitate and 1mM palmitoleate, sapienate, oleate, arachidonate and linoleate. As control, 100% ethanol was diluted 1:50 in 10% BSA and processed the same way as fatty acids. Next, they were incubated in water bath at 37°C for at least 1 hour to allow conjugation. Conjugated fatty acids were aliquoted to avoid freeze-thaw cycles and stored at -20°C.

$^{13}C_6$ glucose labelling experiments

Patient-derived GBM cells were prepared into a single-cell suspension, seeded in laminin-coated 12-well plates (Corning) and grown in a humidified environment at 37 °C with 5% CO_2. After 24 h, the medium was aspirated, cells were washed with dPBS, and replaced with medium 10mM $^{13}C_6$ glucose and with/without 250μM TMZ or 0.25% DMSO as control. Ethanol conjugated with BSA was used as control for fatty acid treatments. Cells were put back in the incubator and incubated for 6 days.

Cell Death Analysis

Cell Death analysis was performed using the IncuCyte ZOOM™ Live Cell Analysis System (Essen BioScience, Inc.). Cells were seeded at a standardized density (10k-20k/well) in laminin-coated 96-well flat clear bottom black plates (Corning) in 100μl of culture medium. After 24 hours, 100μl of fresh medium was added containing 2X the final concentration of fatty acids and/or drugs and 1μM of the dead-cell permeant fluorescent dye Sytox Green™ (Final concentration: 0.5μM) (Life Technologies). The plate was then placed in the IncuCyte chamber maintained in a humidified environment at 37 °C with 5% CO_2 and imaged every 2 hours for 9-10 days. Images were captured using the 10X objective in the phase contrast and green fluorescence channel (400ms exposure). Subsequently, phase confluence and number of sytox green positive cells were measured using the IncuCyte ZOOM™ software (Essen BioScience, Inc.). At each time point, the number of sytox

green positive cells in a well was normlaised to cell confluence in that well to obtain the metric "Cell Death Index".

Protein extraction and western blot analysis

Cells were collected in dPBS by scraping and lysed in RIPA lysis and extraction buffer (Thermo Fisher Scientific) supplemented with protease (Merck Sigma) and phosphatase (Merck Sigma) inhibitors. Extracted proteins were quantified using the Pierce BCA Protein Assay Kit (Thermo Fisher Scientific). Subsequently, 40 µg of protein was loaded on a precast gel NuPAGE Novex 4–12% Bis-Tris (Thermo Fisher Scientific). Proteins were then transferred onto a nitrocellulose membrane using an iBlot2 dry blotting system with iBlot2 transfer stacks (Thermo Fisher Scientific). Membranes were incubated for 1 h at room temperature in a blocking solution of 5% BSA in Tris buffer saline 0.05% Tween-20 (TBS-T). Subsequently, the membranes were incubated overnight at 4 °C with primary antibodies against γh2AX (1:2000) (Merck Millipore#05-636) and α-tubulin (1:2000) (CST#2144).The next day, membranes were incubated with HRP-linked anti-rabbit (Cell Signaling Technology, 7074S) or mouse (Cell Signaling Technology, 7076S) secondary antibodies, used at a dilution of 1:3000 in 5% milk in TBS-T. Bound antibodies were visualized using SuperSignal West Femto Maximum Sensitivity Substrate (Thermo Fisher Scientific). Images were acquired using the ImageQuant LAS 4000 (GE Healthcare).

RNA isolation and qPCR with reverse transcription

Total RNA was isolated with TRIzol reagent (Life Technologies) and cDNA was prepared using qScript cDNA Synthesis Kit (Quantabio) according to manufacturer's instructions. qPCR was performed using PerfeCTa SYBR Green SuperMix (Quantabio) on 7500 Fast Real Time PCR System (Applied Biosystems, Life Technologies) or Platinum™ SYBR™ Green qPCR SuperMix-UDG on ViiA 7 Real-Time PCR System (Applied Biosystems, Life Technologies). Amplification was performed at 95 °C for 10 min, followed by 40 cycles of 15 s at 95 °C and 1 min at 60 °C. *RPL19* was used was loading control. Primer sequences of the genes quantified were: *RPL19* Fwd: 5'-ACCCCAATGAGACCAATAAA-3', *RPL19* Rev: 5'-CGCAAAATCCTCATTCTCCT-3', *FASN* Fwd: 5'-CGCTCTGGTTCATCTGCTCT-3', *FASN* Rev: 5'-GAGCGTAGGATGGAATCTCG-3', *FADS2* Fwd: 5'-GACCACGGCAAGAACTCAAAG-3', *FADS2* Rev: 5'-GAGGGTAGGAATCCAGCCATT-3', *SCD* Fwd: 5'-TCTCTGCTACACTTGGGAGC-3', *SCD* Rev: 5'-GAGCTTTGTAAGAGCGGTGG-3'.

FACS analysis for activated caspase

Percentage of cells with active caspase was determined using CellEvent™ Caspase-3/7 Green Detection Reagent (Thermo Fischer Scientific) as per manufacturer's instructions. Briefly, GBM cells were seeded in laminin-coated plates and then treated with temozolomide for 4 days. Next, the medium was aspirated and replaced with fresh medium with/without temozolomide and palmitate for 2 days. Prior to FACS analysis, medium was again aspirated from the cells and supplemented with medium containing 2μM of CellEvent™ Caspase-3/7 Green Detection Reagent. The plate was put was in the incubator for 30minutes. Subsequently, the cells were collected by scraping and resuspended in 200 μl of dPBS containing 50μg/ml propidium iodide (PI) for live/dead cell differentiation. Samples were acquired on a FACSCanto™ II analyzer (BD Biosciences) using the FACSDiva™ v8.0 software (BD Biosciences), and further analyzed with FlowJo v10.7 (BD Biosciences). Events were first gated to remove cell debris in the FSC-A *vs*. SSC-A plane, followed by doublet removal and selection of live (PI-negative) cells. Caspase activation (FITC +ve) cells were then determined in this population.

Metabolite extraction from cells, tissue, plasma and CSF

Metabolite extractions were performed as previously described [60,252]. For cell samples, wells were washed with blood bank saline, and cell metabolism was quenched by flash-freezing the plates in liquid nitrogen. For tissues, samples were weighed (5–15 mg) and pulverized (Cryomill, Retsch) under liquid nitrogen conditions. For plasma, 20μl of cold plasma was transferred to an Eppendorf tube. For cerebrospinal fluid, the entire volume that could be obtained from each mouse (5-7μl) was used and the volume noted down for normalization. All samples were stored at –80 °C until metabolite extraction. For cells, 800 μl of –20 °C cold 65% methanol was added to the wells and cells were scraped with a pipette tip and suspensions were transferred to Eppendorf tubes. For tissue, plasma or CSF samples, 800 μl of –20 °C cold 65% methanol was directly added to the tube containing pulverized tissue or liquid. Next, 500 μl of –20 °C cold chloroform was added and samples were vortexed at 4 °C for 10 minutes to extract metabolites. Phase separation was achieved by centrifugation at 4 °C for 10 minutes, after which the

chloroform phase (containing the total fatty acid content) was separated and dried by vacuum centrifugation.

Metabolite measurement via GC-MS

Total fatty acid samples were esterified with 500µl 2% sulfuric acid in methanol overnight at 50 °C and extracted by addition of 600µl hexane and 100µl saturated aqueous NaCl. Samples were centrifuged for 5 min and the hexane phase was separated and dried by vacuum centrifugation. Samples were resuspended in hexane, after which total fatty acids were measured with a 7890A GC system (Agilent Technologies) combined with a 5975C or a 7000 inert MSD system (Agilent Technologies). 1µl of each sample was injected in splitless or 3:1 split (7000) mode with an inlet temperature of 270 °C onto a DB35MS column (Agilent Technologies). Helium was used as a carrier gas with a flowrate of 1 ml per min. The oven was held at 80 °C for 1 min and ramped with 5 °C per min to 300 °C. The mass spectrometry system was operated under electron impact ionization at 70 eV and a mass range of 100–650 amu was scanned.

Relative quantification of fatty acids: Relative metabolite abundances were determined using an in-house MATLAB script. Total ion counts were normalized to an internal standard (heptadecanoate) and protein content for cell extracts. The protein concentration was quantified using Pierce BCA Protein Assay Kit (Thermo Fisher Scientific). Tissue samples were normalized to tissue weight (in mg).

Absolute quantification of fatty acids in plasma and CSF: To quantify the absolute levels of fatty acids, a standard curve was prepared using 9 serial dilutions of a fatty acid mix containing palmitate, stearate, sapienate, palmitoleate, cis-vaccenate, oleate, linoleic acid, linolenic acid and γ-linolenic acid. 20µl of each dilution was then extracted and analyzed via GC-MS as described above. Metabolite abundances were determined using an in-house MATLAB script. Total fatty acid amount in each sample was then calculated by extrapolating it to the standard curve. Concentration (in µM) was then calculated using the known parameters of amount, molecular weight and volume extracted (20µl).

Isotopologue distributions: Isotopologue distribution was determined using an in-house MATLAB script. Correction for naturally occurring isotopologues was achieved using Isocor software.

Collection of mouse blood plasma and cerebrospinal fluid

7-9 weeks old male C57BL/6J mice were purchased from Janvier Labs. Mice were kept in standard housing conditions with 12 h of light and 12 h of dark. Food and water were provided ad libitum. The temperature was kept between 20 and 24 °C and the humidity between 45 and 65%. All mouse experiments were performed according to the regulations of the Ethische Commissie Dierproeven at the Vrije Universiteit Brussel.

Blood collection: Blood was withdrawn through heart puncture using EDTA-filled syringes. It was centrifuged at 12,000rcf for 10mins and 20ul of clear plasma was retrieved and instantly frozen.

CSF collection: Animals were anesthetized using Ketamine/Xylazine mixture at a dose of 210 mg/kg and 15 mg/kg respectively. Next, the animal was immobilized on its back and 0.5-1 ml of blood collected via a blind heart puncture. The animal was then turned the animal on its ventral side and a small subcutaneous incision was made in the back of the head and cisterna magna located by visual inspection. Finally, using a micropipette, the cisterna magna was punctured, making sure to not touch the brain parenchyma or any blood vessels. Due to capillary action, 4-7 µl of CSF will automatically flow into the pipette. The animal was then euthanized according to approved protocols.

Collection of human glioblastoma samples

Human samples were collected upon ethical approval of local authorities (S65850). Tissues were obtained from UZ Brussel, Jette (Belgium) after obtaining informed consent.

Statistical analysis

Statistical data analysis was performed using GraphPad Prism v.9.3.1 (GraphPad Software) on $n \geq 3$ biologically independent replicates. Specific details on statistical tests are presented in the figure legends. All data are presented as mean ± s.d.

Data availability

Raw sequencing reads of the human scRNA-seq experiments have been deposited in the controlled access public repository European Genome-phenome Archive (EGA), under study accession number EGAS00001004871.

4.4 Results

Glioblastoma cancer cells display a highly heterogeneous lipid metabolism with high sapienate production

To define the intra-tumour heterogeneity of glioblastoma (GBM) tissues, we analysed the single-cell gene expression profiles of IDH-wt GBM (samples ND1-ND6) from 6 newly diagnosed patients [253]. We identified major cell populations consisting of B cells, T-cells, cancer cells, oligodendrocytes, endothelial cells and fibroblasts using unsupervised clustering (Figure 4.1A). Subsequently, we performed sub-clustering analysis within the cancer cell cluster to better examine intra-tumor heterogeneity. The cancer cell cluster, comprising 17,649 cells, could be divided into 12 distinct sub-clusters (SC: 3, 6, 7, 8, 11, 12, 13, 15, 17, 21, 23 and 24; Figure 4.1B). Next, we selected only cancer cell clusters that were present in most patients, and removed clusters with features indicative of low quality (e.g. low read counts and/or number of genes; see methods and Figure 4.3). Based on this, five sub-clusters (SC: 6, 7, 8, 11, 17) were considered for all subsequent analyses. These results highlight the cellular heterogeneity in GBM cancer cells.

Cellular metabolism has been identified as a liability of tumors within the brain [250,254]. Therefore, we further focused on investigating the metabolic heterogeneity of GBM cancer cells. For this, we ranked all genes in the data set based on their degree of variability across all cells in the 5 cancer cell sub-clusters. This ranked gene list was then used as input for gene set enrichment analysis (GSEA). Normalized enrichment scores (NES) were determined for KEGG-based gene sets representing all metabolic genes, as well as genes involved in specific metabolic pathways (lipid, energy, carbohydrate, amino acid or nucleotide metabolism), and other metabolic genes (i.e. not belonging to any of the latter pathways). Of note, a high NES value indicates here an

overrepresentation of the genes present in the corresponding pathway among the most highly-variable genes in the data set, and thus NES values can be interpreted as a proxy for heterogeneity. Our results indicate that GBM cancer cells display an overall high metabolic heterogeneity. We further observed that, within this metabolic heterogeneity, lipid metabolism was the most heterogenous pathway in GBM cancer cells (Figure 4.1C). This suggests that lipid metabolism is a key contributor to the intra-tumor heterogeneity of GBM.

Prior studies have shown that while brain tissue itself is lipid-rich, the brain microenvironment is characterized by a deprivation of circulating lipids in the cerebrospinal space, and that tumor cells metastasizing to the brain adapt to this lipid-deprived environment by upregulating fatty-acid synthesis[250]. In line with these studies, we observed that the cerebrospinal fluid obtained from healthy C57BL/6 mice was severely lipid deprived (Figure 4.1D). This suggests that *de novo* fatty acid synthesis may also be relevant for GBM progression. *De novo* fatty-acid synthesis involves the production of long-chain saturated fatty acids (mainly palmitate) from acetyl-CoA and malonyl-CoA via the fatty acid synthetase (FASN), which are then converted into unsaturated fatty acids (e.g. palmitoleate) by desaturase enzymes such as stearoyl-CoA desaturase (SCD). Interestingly, we have previously identified an alternative fatty acid mono-desaturation pathway in cancer, mediated by the delta-6-desaturase FADS2, which instead of palmitoleate produces the unusual fatty acid sapienate[60]. In line with this, we reported that GBM tumors display very high FADS2 expression[128]. This suggests that some cancer cells within GBM tumors may alternatively rely on the desaturation of *de novo* synthesized fatty acids to either palmitoleate, sapienate, or both. Thus, we performed GC-MS based analysis of the total fatty acid in 8 human glioblastoma tumors and found that, overall, GBM tumors have nearly equivalent relative SCD activity (palmitoleate to palmitate ratio) and FADS2 activity (sapienate to palmitate ratio) (Figure 4.2A). This indicates that GBM tumors indeed exploit this alternative desaturation pathway and produce considerable amounts of sapienate on top of palmitoleate. The tumors also displayed significant amounts of arachidonic and docosahexaenoic acid, products of the FADS2 PUFA pathway (Figure 4.4A-B). We next compared commercial (U87, U251, U118, LN18) and patient derived GBM cell lines to A549 human lung adenocarcinoma and HUH7 human hepatocellular carcinoma that we have previously characterized [60]. We saw that all GBM cell lines, especially

those derived freshly from patients had significant sapienate production, comparable to that of the FADS2-high HUH7 cells (Figure 4.2B). Of note, GBM cancer cells were also observed to display a high expression of the above mentioned fatty acid synthesis and desaturation genes (*FASN, SCD* and *FADS2*) relative to most other cell types in our scRNA-seq data set (Figure 4.4C), with the exception of oligodendrocytes, for which *SCD* was also highly expressed, in agreement with prior reports [255]. Taken together, these data suggest a preference for *de novo* fatty acid synthesis and desaturation in GBM cells, a feature that might be attributed to the severe lack of extracellular lipids in the brain microenvironment (Figure 4.1D) [250]. They further suggest that GBM cells may rely on either (or both) SCD and FADS2 for fatty-acid desaturation, thus contributing to their heterogeneity at the metabolic level.

In line with the above results, we next asked whether the three key genes of *de novo* fatty acid synthesis, namely *FASN*, *FADS2*, and *SCD*, indeed contribute to GBM heterogeneity (Figure 4.2D). Based on the expression of these three genes, the cancer cell clusters could be subdivided into SCD high (SCD-Hi (SC 6)), FADS2 high (FADS2-Hi (SC 17)), FASN high (FASN-Hi (SC 11)), SCD/FADS2/FASN high, (Triple-Hi (SC 7)) and SCD/FADS2/FASN low (Triple-low (SC 8)) cancer cells (Figure 4.2D). We thus next asked whether these different fatty-acid metabolism-defined clusters represented cells with distinct cell fate or function. To address this question, we used gene set variation analysis (GSVA) to determine relative enrichment scores, among all five clusters, for a known set of publicly available gene meta-modules identifying known GBM cell states or fates [238]. Remarkably, we found a strong correlation between these expression-annotated sub-clusters and specific cell states. The FASN-Hi sub cluster was strongly correlated with a gene expression module defining cycling cells, whereas SCD-Hi cells displayed a preference for mesenchymal lineage, FADS2-Hi cells displayed an astrocytic lineage signature, Triple-Hi cells displayed a preference for oligodendroglial precursor fate, and Triple-low cells displayed a signature of neural progenitor cells (Figure 4.2E). Thus, these results suggest that the expression levels of lipid metabolism genes are associated with cell fate and potentially functionality in GBM.

Overall, our results demonstrate that GBM cancer cells from patients are metabolically heterogeneous, particularly with regards to lipid metabolism. They further show how this metabolic heterogeneity drives intra-tumoral GBM heterogeneity, with the relative expressions

of the three key enzymes involved in the fatty acid synthesis pathway being strongly correlated with different cancer cell fates.

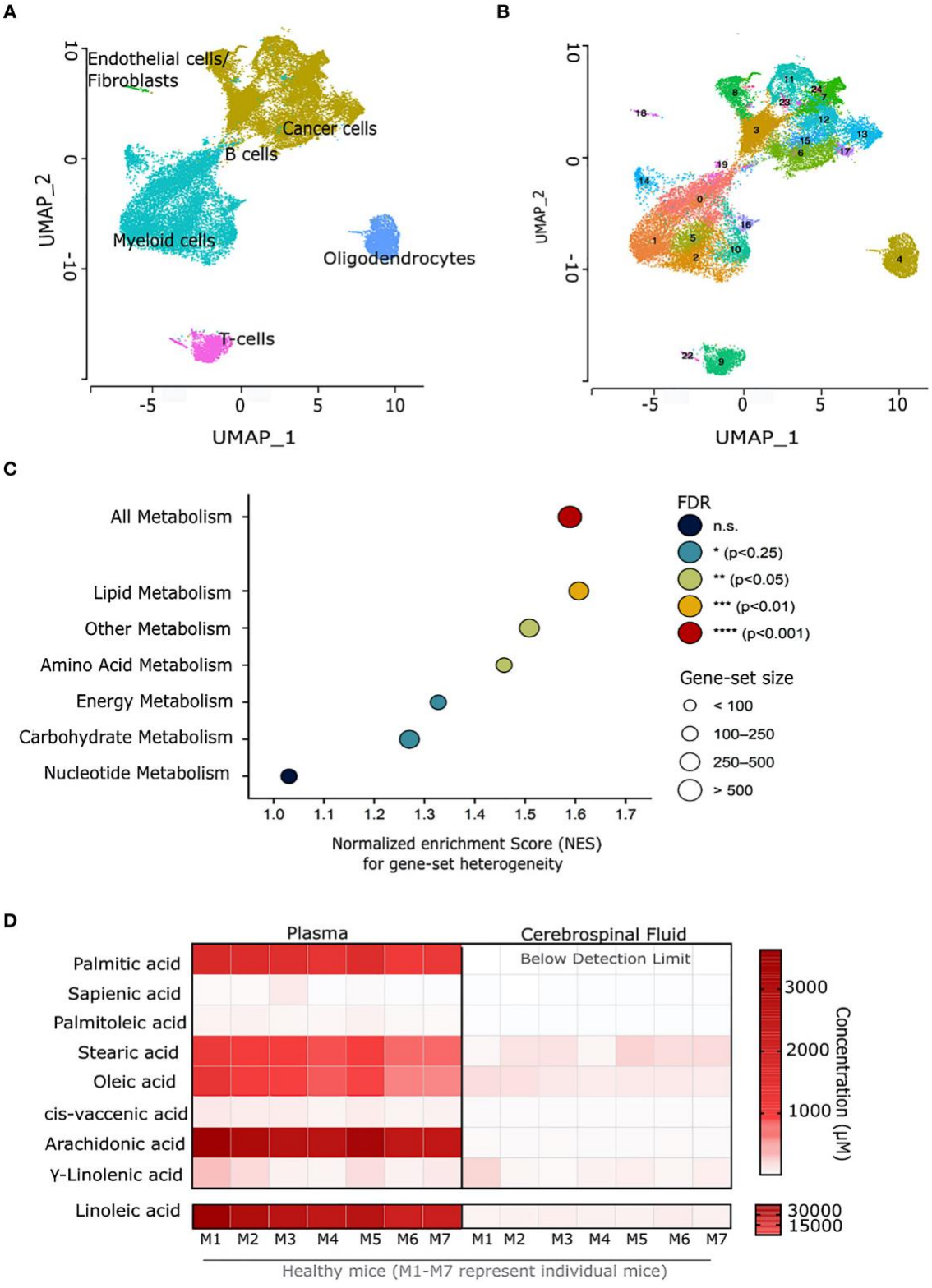

Figure 4.1: Glioblastoma cancer cells have a highly heterogeneous lipid metabolism

(A) Uniform manifold approximation and projection (UMAP) plots of single-cell RNA sequencing data from fresh GBM tissue derived from 6 patients newly diagnosed with GBM **(B)** UMAP plots of sub-clustering analysis performed on single-cell RNA sequencing data from fresh GBM tissue derived from 6 patients newly diagnosed with GBM **(C)** Results of GSEA-based metabolic pathway-heterogeneity analysis for GBM cancer cells. The y-axis indicates the different KEGG-based gene sets included in the analysis (see Methods), whereas the x axis represents the normalized enrichment scores determined for each gene set based on pre-ranked GSEA. Input genes were ranked based on their standardized variances across all cancer cells in sub-clusters of interest (SC: 6, 7, 8, 11, 17) among those in Figure 4.1B. False discovery rate (FDR)-adjusted p values are indicated by the color scale, with gene-set sizes indicated by the dot areas. **(D)** Total fatty acid concentration (μM) in blood plasma and cerebrospinal fluid from 7 C57BL/6J mice (M1-M7 represent individual mice).

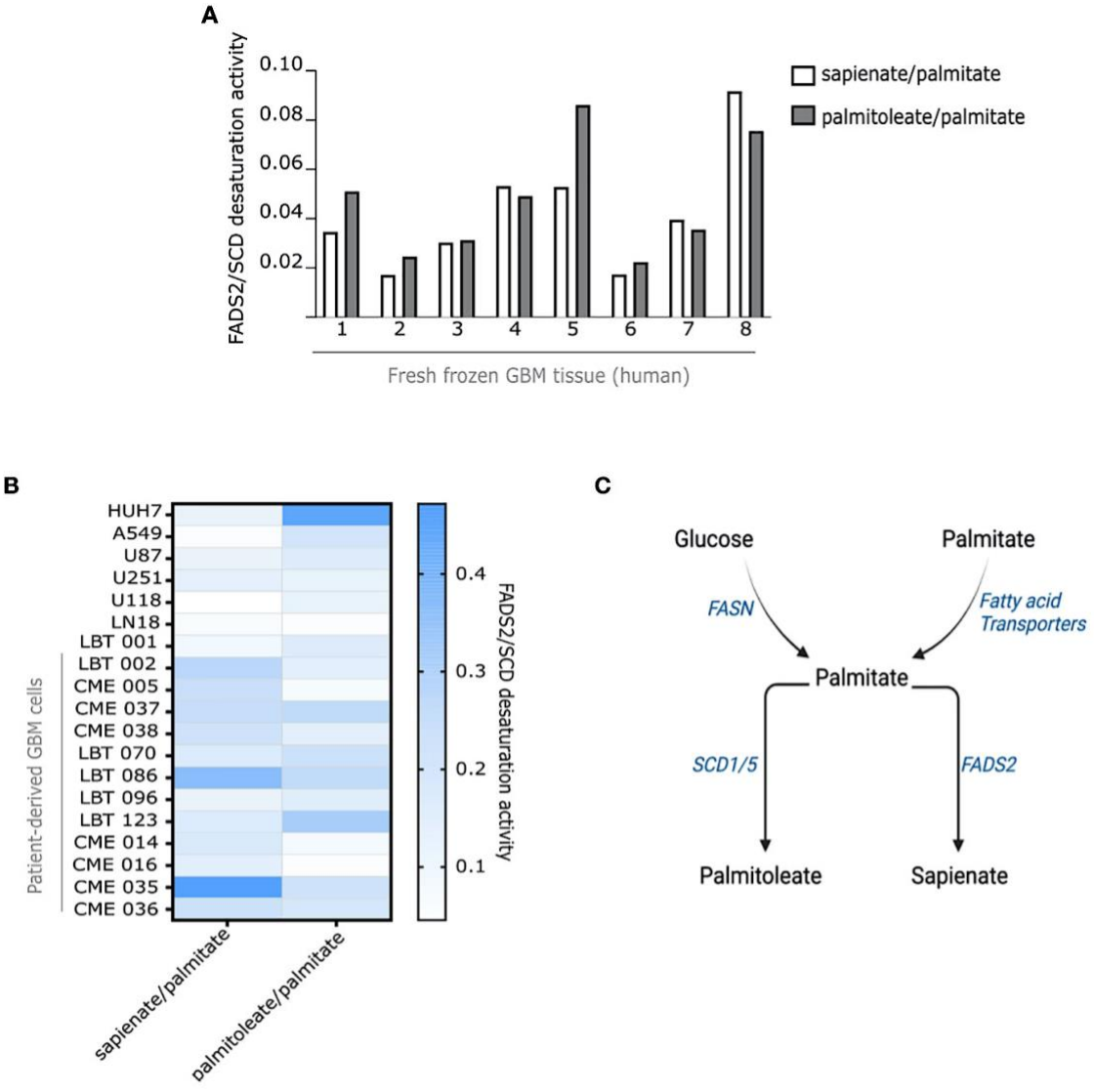

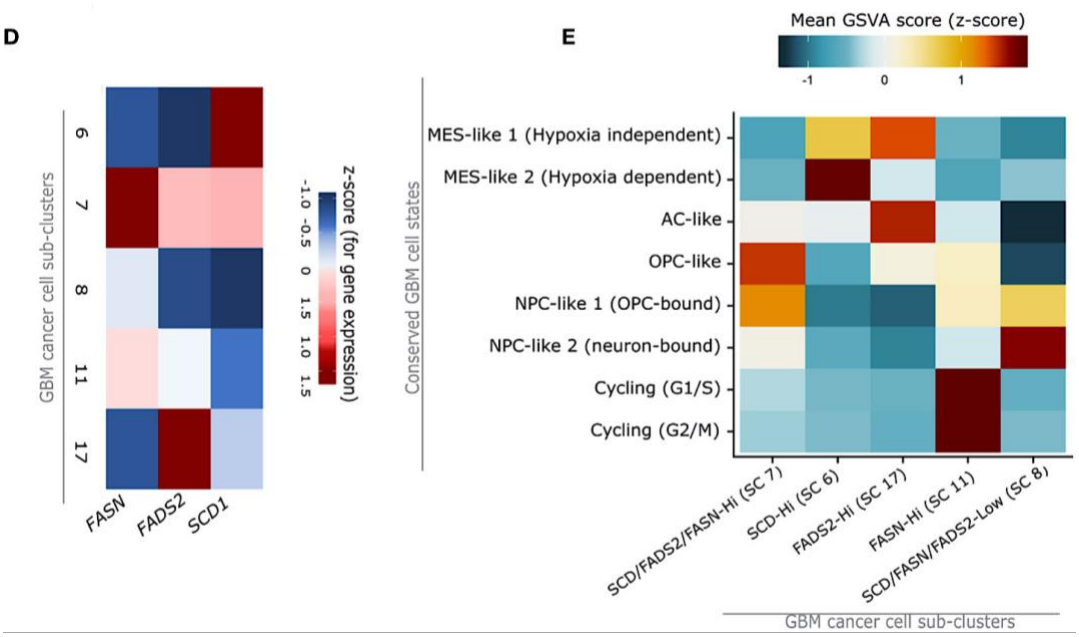

Figure 4.2: Fatty acid metabolism in GBM cancer cells is linked to cell fate

(A) Desaturation activity of SCD (palmitate-to-palmitoleate ratio) and FADS2 (sapienate-to-palmitate ratio) in fresh frozen GBM tissue from 8 patients (B) Desaturation activity of SCD (palmitate-to-palmitoleate ratio) and FADS2 (sapienate-to-palmitate ratio) in human cell lines: hepatocellular carcinoma (HUH7), lung adenocarcinoma (A549), immortalized GBM cells (U87, U251, U118, LN18) and patient-derived GBM cell lines (LBT 001, LBT 002, CME 005, CME 037, CME 038, LBT 070, LBT 086, LBT 096, LBT 123, CME 014, CME 016, CME 035, CME 036). Colour scale represents mean desaturation activity (n=3). HUH7, U87, U251, LN18, U118 were cultured in 1% FBS medium, A549 cells were cultured in 0.5% FBS medium. Patient-derived GBM cells were cultured in NSA medium without FBS. **(C)** Brief overview of the fatty acid mono-desaturation pathway.**(D)** Average gene expression levels of *FASN*, *SCD1* and *FADS2* in cancer cell sub-clusters of interest (SC: 6, 7, 8, 11, 17) among those in Figure 4.1B. The colour scale indicates Z-scores, based on the overall mean expression level (and associated standard deviation) for each gene across all sub-clusters. **(E)** GSVA scores for gene sets representing different GBM cell fates in cancer cell sub-clusters of interest (SC: 6, 7, 8, 11, 17) among those in Figure 4.1B. The colour scale indicates Z-scores, based on the overall mean GSVA score (and associated standard deviation) for each gene set across all sub-clusters. MES=mesenchymal, AC=astrocytic cells, OPC=oligodendrocytic precursor cell, NPC=neuronal progenitor cell.

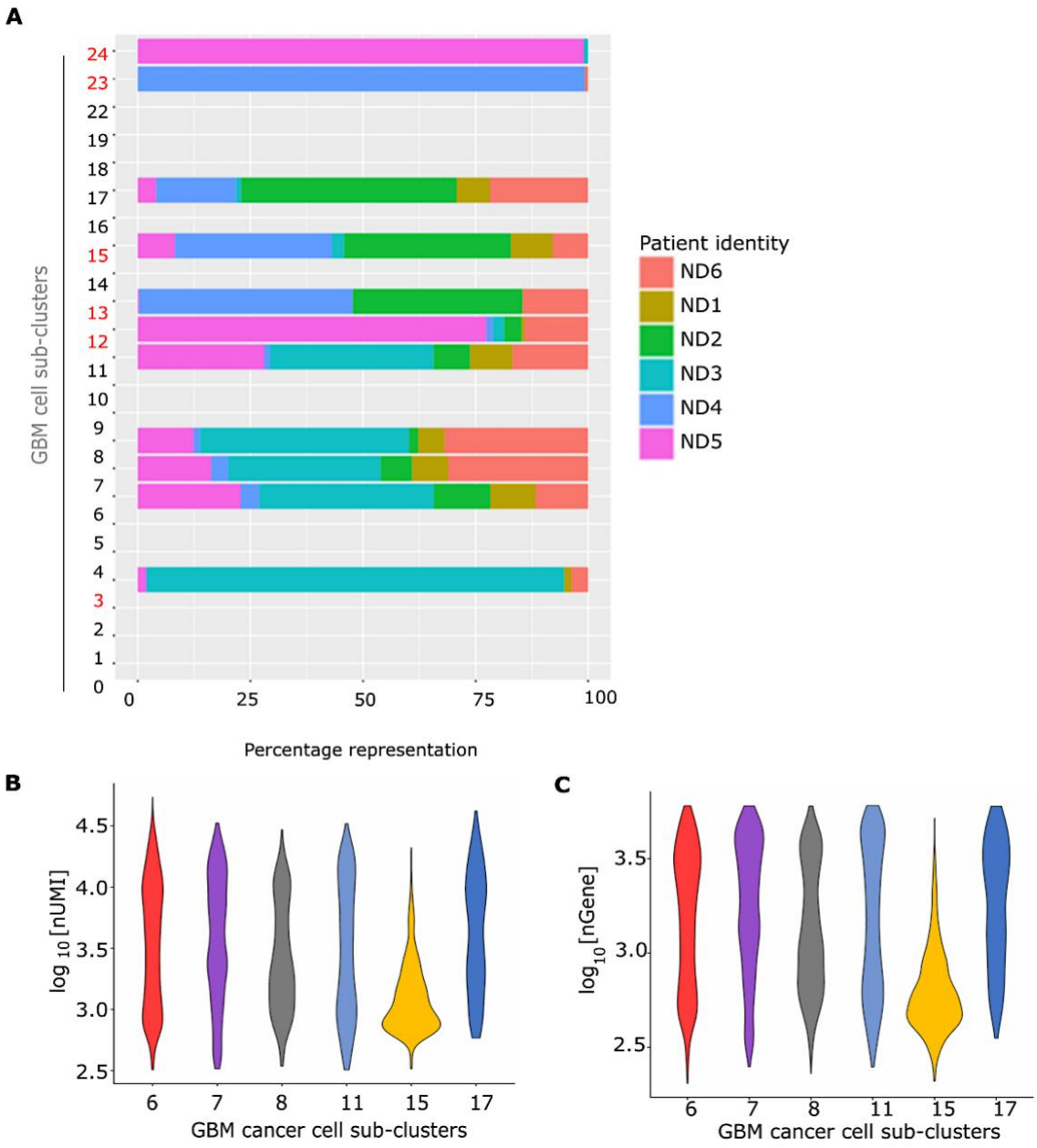

Figure 4.3: Quality control of GBM single-cell RNA sequencing data.

(A) Percentage of cells from each patient in GBM cell sub-clusters. **(B)** Log transformed read counts per cell (log_{10} nUMI) in GBM cancer cell sub-clusters. **(C)** Log transformed no. of detected genes per cell (log_{10} nGene) in GBM cancer cell sub-clusters.

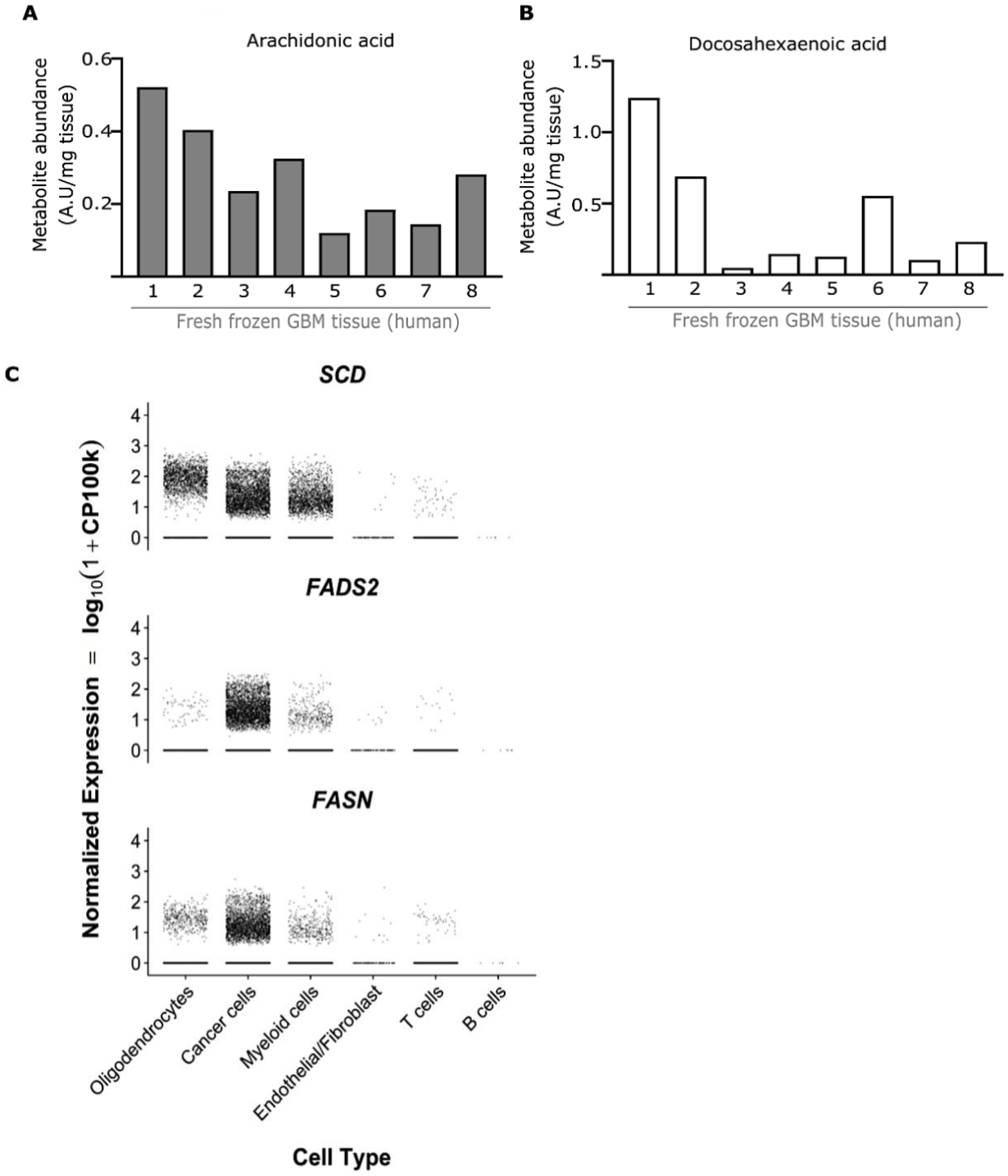

Figure 4.4: GBM tissues produce FADS2-mediated polyunsaturated fatty acids.
(A) Metabolite levels of arachidonic acid in fresh frozen GBM tissue from 8 patients. **(B)** Metabolite levels of docosahexaenoic acid in fresh frozen GBM tissue from 8 patients. **(C)** Normalized expression of FADS2, FASN and SCD in B-cells, T-cells, oligodendrocytes, cancer cells, myeloid cells and endothelial cells/fibroblasts determined via scRNA sequencing.

We next asked whether lipid metabolism contributes to the resistance of reoccurring GBM tumours to the chemotherapeutic agent TMZ. We used four pairs of patient-derived cell lines from matched newly diagnosed (ND) and recurrent GBM (RC) tissue of the same patients. The cells were cultured in low lipid media to resemble the metabolic particularity of the brain (Figure 4.1D). We treated the cell line pairs with TMZ, which induces double stranded break (DSBs) formation in cells, ultimately causing cell death [256]. Phosphorylation at ser-139 residue on histone 2A (γh2AX), a marker of DSB formation [257], was increased in patient derived cell lines from newly diagnosed GBMs cells upon TMZ treatment, while patient derived cell lines from recurrent GBM did not alter h2AX phosphorylation in the presence of TMZ (Figure 4.5A). Thus, in line with the situation in patients, *in vitro* cultured cells derived from recurring GBM had a lower sensitivity to TMZ.

Subsequently, we measured whether TMZ treatment altered the fatty acid metabolism of these cultured GBM cell line pairs. In all 4 pairs, newly diagnosed GBM showed a significant reduction or a trend towards it in mRNA levels of *FASN, FADS2* and *SCD* (Figure 4.5B-D and Figure 4.6) upon TMZ treatment, while recurring GBMs showed either no significant effect or even an increase in the mRNA expression. (Figure 4.5B-D and Figure 4.6). To investigate whether these expression changes translated into altered metabolic activities of these enzymes, we performed ^{13}C tracing analysis [258] by adding 10mM uniformly labelled glucose ($^{13}C_6$ glucose) to the culture medium. We observed that the fraction of labelled glucose incorporated into palmitate, sapienate and palmitoleate reduced upon TMZ treatment in cells derived from newly diagnosed GBM#1 but not in recurring GBM#1 (Figure 4.5E-G) while another pair (GBM#4) displayed this effect for palmitate and palmitoleate and not for sapienate (Figure 4.7A-C). Overall, these results indicate that chemotherapeutic treatment of GBM cell lines reduces the *de novo* fatty acid synthesis and desaturation, a response that is blunted in recurrent GBM cell lines.

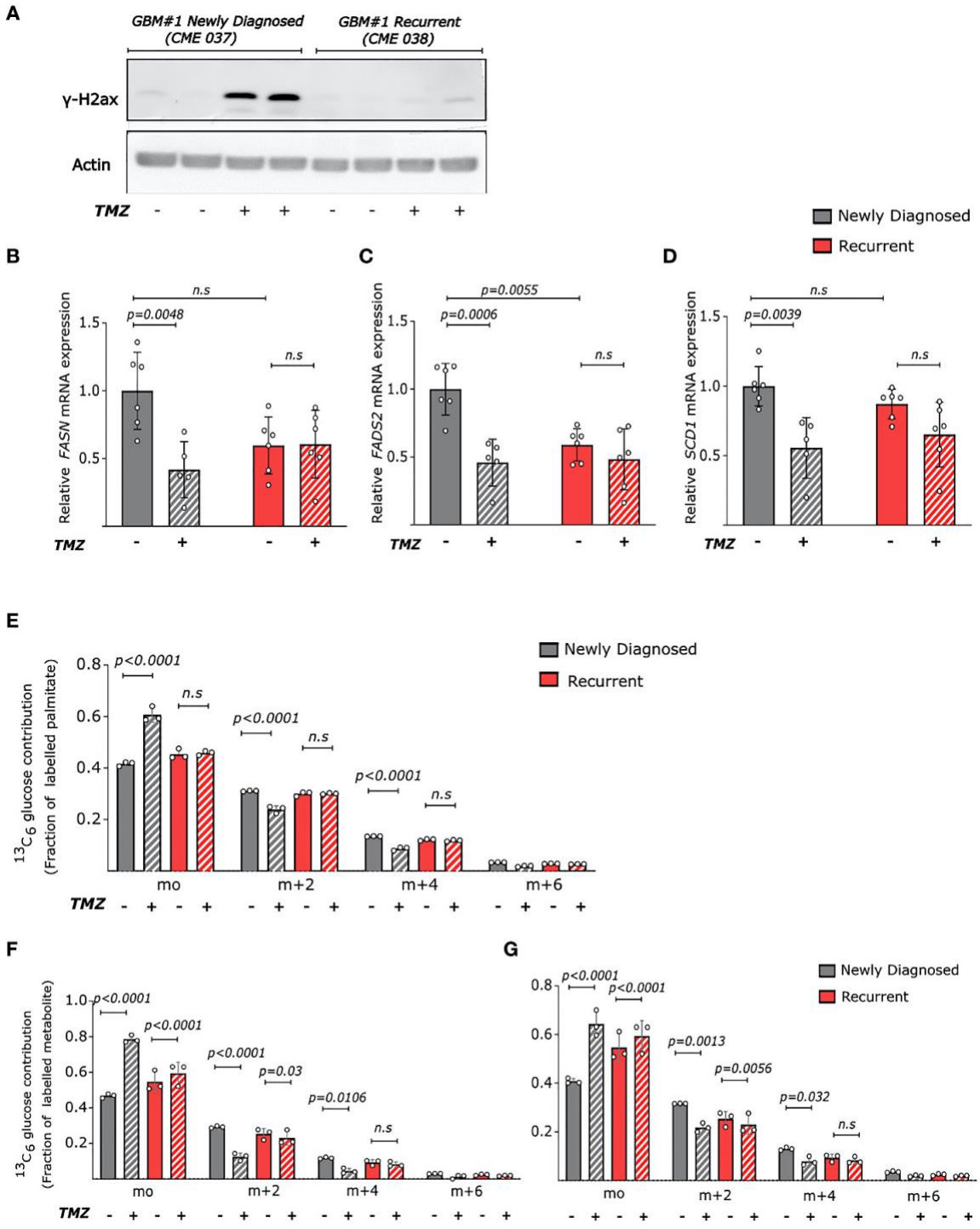

Figure 4.5: Temozolomide abrogates fatty acid metabolism in newly diagnosed but not recurrent GBM
(A) Protein levels of phosphorylated h2AX (γh2AX) and α-tubulin (loading control) in newly diagnosed (CME 037) and recurrent (CME 038) cells from GBM#1 ±TMZ (250μM). TMZ treatment was done for 6 days. **(B-D)** Relative mRNA levels of **(B)** *FASN*, **(C)** *FADS2* and **(D)** SCD1 in newly diagnosed (CME 037) and recurrent (CME 038) cells from GBM#1 ±TMZ (250μM). RPL19 was used as internal control. TMZ treatment

was done for 6 days. Statistical analysis was performed using two-way ANOVA with Sidak's multiple comparison. n=5-6. **(E-G)** Dynamic labelling of newly diagnosed (CME 037) and recurrent (CME 038) cells from GBM#1 with 13C6-glucose showing ^{13}C incorporation into **(E)** palmitate, **(F)** sapienate and **(G)** palmitoleate. TMZ treatment and $^{13}C_6$-glucose supplementation was continued for 6 days. Statistical analysis was performed using two-way ANOVA with Tukey's multiple comparison. n = 3.

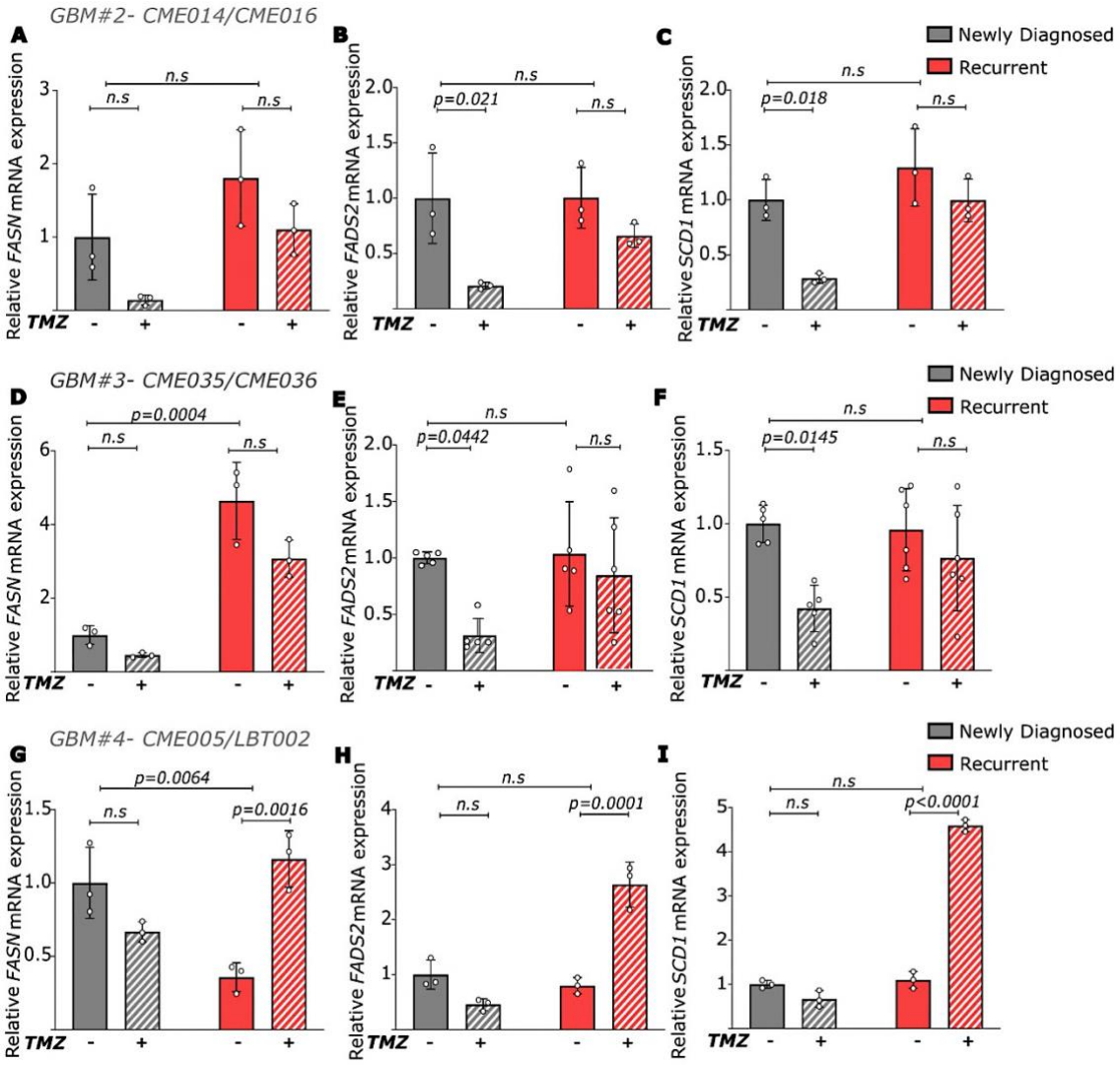

Figure 4.6: Temozolomide abrogates fatty acid metabolism in newly diagnosed but not recurrent GBM

(A-C) Relative mRNA levels of **(A)** *FASN*, **(B)** *FADS2* and **(C)** *SCD* in newly diagnosed (CME 014) and recurrent (CME 016) cells from GBM#2 ±TMZ (250μM). RPL19 was used as internal control. TMZ treatment was done for 6 days. Statistical analysis was performed using two-way ANOVA with Sidak's multiple comparison. n=3. **(D-F)** Relative mRNA levels of **(D)** *FASN*, **(E)** *FADS2* and **(F)** *SCD* in newly diagnosed (CME 035) and recurrent (CME 036) cells from GBM#3 ±TMZ (250μM). RPL19 was used as internal control. TMZ

treatment was done for 6 days. Statistical analysis was performed using two-way ANOVA with Sidak's multiple comparison. n=3. **(G-I)** Relative mRNA levels of (**G**) *FASN*, **(H)** *FADS2* and **(I)** *SCD* in newly diagnosed (CME 005) and recurrent (LBT 002) cells from GBM#4 ±TMZ (250μM). RPL19 was used as internal control. TMZ treatment was done for 6 days. Statistical analysis was performed using two-way ANOVA with Sidak's multiple comparison. n=3.

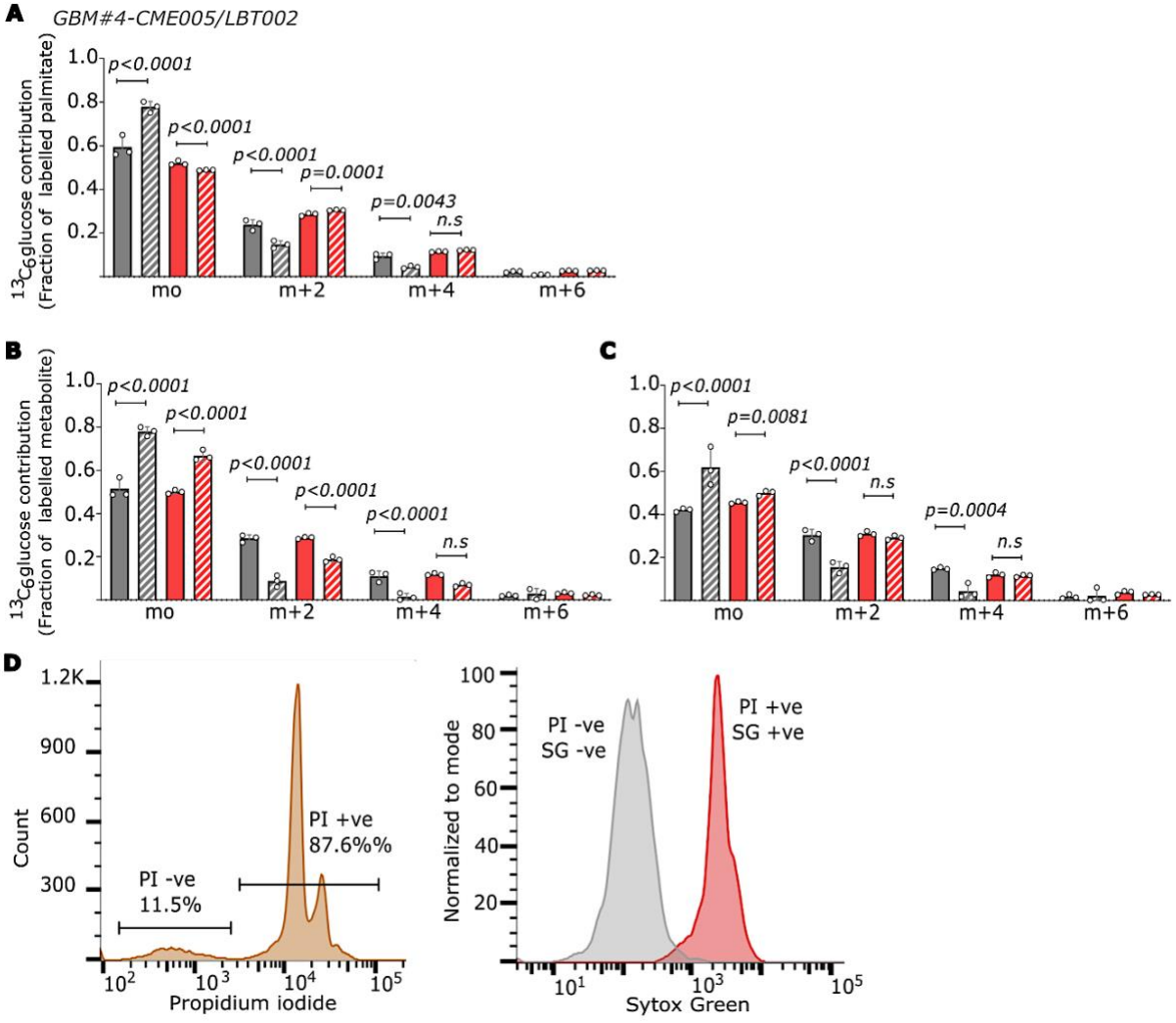

Figure 4.7: Temozolomide abrogates *de novo* fatty acid synthesis and desaturation in newly diagnosed but not recurrent GBM.

(A-C) Dynamic labelling of newly diagnosed (CME 005) and recurrent (LBT 002) cells from GBM#4 with 13C6-glucose showing ^{13}C incorporation into (**A**) palmitate, (**B**) sapienate and (**C)** palmitoleate. TMZ treatment and $^{13}C_6$-glucose supplementation was continued for 6 days. Statistical analysis was performed using two-way ANOVA with Tukey's multiple comparison. n = 3**. (D)** FACS analysis of GBM cells co-stained with propidium iodide (PI) and sytox green. PI-positive and negative cells were gated in the single cells. Sytox green intensity was then determined in cells within the PI-positive and negative gates.

Palmitate supplementation sensitizes GBM to temozolomide

Saturated and unsaturated lipids need to be balanced to avoid cell death based on lipotoxicity[115]. We therefore hypothesized that increasing abundance of palmitate (16:0), a saturated fatty acid, could increase the sensitivity of the GBM cell lines to TMZ. To address this hypothesis, we treated cells with palmitate (100μM) alone or in combination with TMZ (250μM) and monitored cell death overtime using the IncuCyte live-imaging system assay. The cells grew in the presence of sytox green, a fluorescent dye selectively permeant to dead cells[259]. Indeed, in a suspension of dead and living cells, only dead cells (that show positive for propidium iodide), also appear positive for sytox green (Figure 4.7D). Cells were imaged every 2 hours for a period of 9-10 days. Subsequently, we measured the number of dead cells, and normalized it to confluence to establish a cell death index. Palmitate alone had a small effect on cell death in cells-derived from newly diagnosed GBM but had no impact on recurring GBM (Figure 4.8A-B). Strikingly, in cell lines derived from both newly diagnosed and recurring GBM, combination of palmitate and TMZ significantly increased cell death compared to the TMZ single treatment in all 4 pairs (Figure 4.8A-B, Figure 4.9). Furthermore, palmitate supplementation with TMZ, increases the percentage of cells with activated caspase as compared to TMZ alone, while palmitate alone has no significant effect (Figure 4.8C). On the other hand, monounsaturated fatty acids, palmitoleate (16:1, n-9) and sapienate (16:1, n-7) had no effect alone or in combination with TMZ (Figure 4.10 and 4.11). Further, we also found that this effect was independent of current GBM prognostic factors. Although GBM cells used in this study had highly varied levels of MGMT (Figure 4.12A) they all showed drastic cell death induction with palmitate (Figure 4.7). Also, isogeneic U87 IDH WT and U87 IDH R132H responded similarly to palmitate supplementation (Figure 4.12B-C), with the latter displaying hypermethylation. Finally, palmitate was also able to re-sensitize GBM cells treated with the DNA hypomethylating agent 5-azacytidine[260] to TMZ (Figure 4.12D-E). Thus, we concluded that palmitate supplementation re-sensitized cells derived from recurring GBM to TMZ.

Induction of cell death based on lipotoxicity is known to be counteracted by the supplementation of unsaturated fatty acids[115]. In line, we found that supplementation of the mono-unsaturated fatty acids sapienate and palmitoleate rescued cell death induced by the combination of TMZ

with palmitate in GBM cell lines (Figure 4.8D-G). Moreover, modulating the canonical regulators of the cellular lipotoxic response[112] was unable to rescue cell death induced by the combination of TMZ with palmitate. While the PERK inhibitor, GSK2606414 had no effect on palmitate induced lipotoxicity, the IRE1 inhibitor, 4μ8C seemed to further augment the palmitate response (Figure 4.13). This suggests that the synergistic action of palmitate with TMZ is not inhibited by targeting conventional ER stress response mechanisms. Thus, we found that palmitate supplementation re-sensitized cell lines derived from recurring GBMs to TMZ treatment.

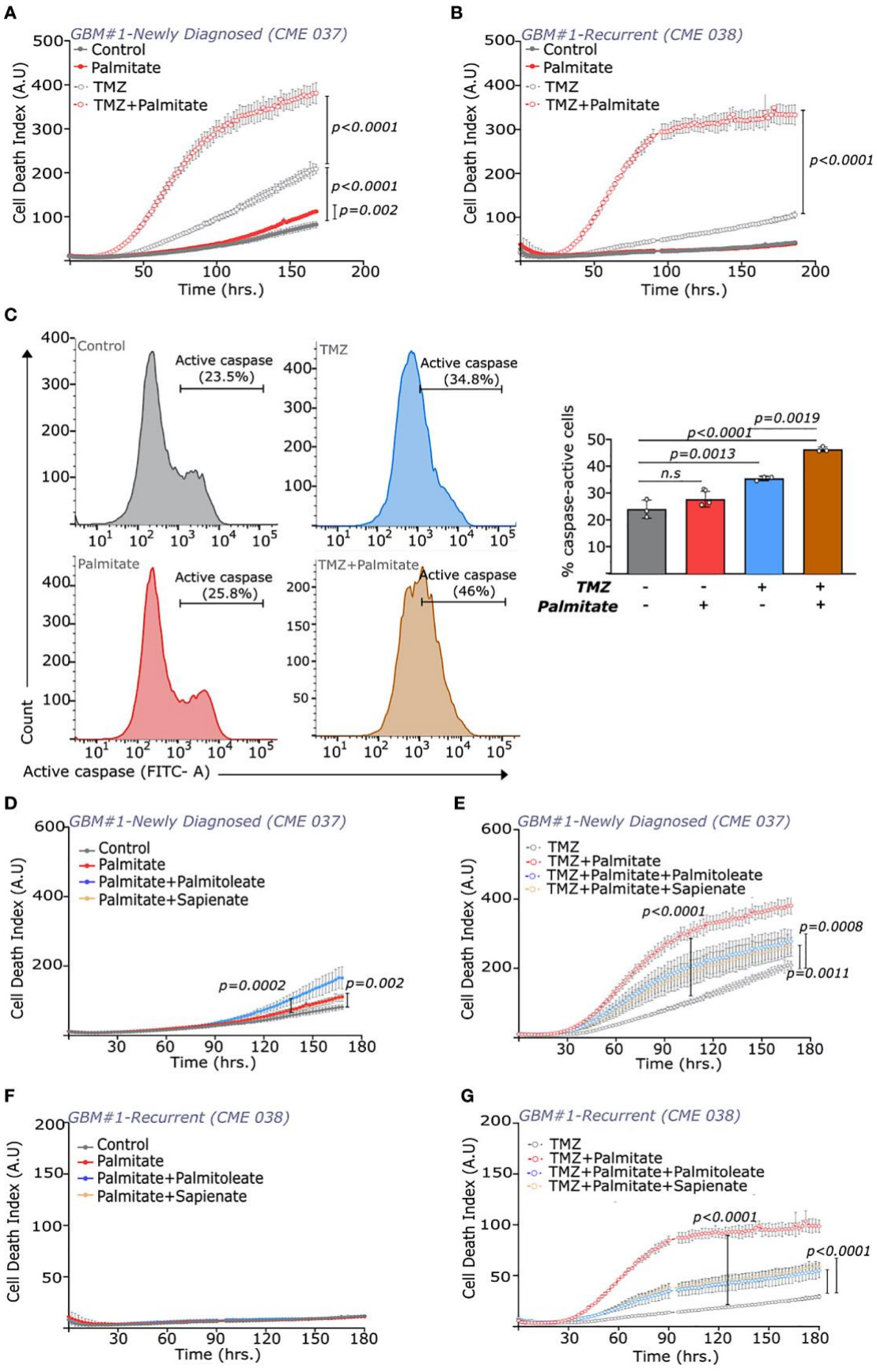
A
GBM#1-Newly Diagnosed (CME 037)
Control
Palmitate
TMZ
TMZ+Palmitate
Cell Death Index (A.U)
Time (hrs.)
p<0.0001
p<0.0001
p=0.002
B
GBM#1-Recurrent (CME 038)
Control
Palmitate
TMZ
TMZ+Palmitate
Cell Death Index (A.U)
Time (hrs.)
p<0.0001
C
Control
Active caspase (23.5%)
TMZ
Active caspase (34.8%)
Palmitate
Active caspase (25.8%)
TMZ+Palmitate
Active caspase (46%)
Count
Active caspase (FITC- A)
% caspase-active cells
p=0.0019
p<0.0001
p=0.0013
n.s
TMZ
Palmitate
D
GBM#1-Newly Diagnosed (CME 037)
Control
Palmitate
Palmitate+Palmitoleate
Palmitate+Sapienate
Cell Death Index (A.U)
Time (hrs.)
p=0.0002
p=0.002
E
GBM#1-Newly Diagnosed (CME 037)
TMZ
TMZ+Palmitate
TMZ+Palmitate+Palmitoleate
TMZ+Palmitate+Sapienate
Cell Death Index (A.U)
Time (hrs.)
p<0.0001
p=0.0008
p=0.0011
F
GBM#1-Recurrent (CME 038)
Control
Palmitate
Palmitate+Palmitoleate
Palmitate+Sapienate
Cell Death Index (A.U)
Time (hrs.)
G
GBM#1-Recurrent (CME 038)
TMZ
TMZ+Palmitate
TMZ+Palmitate+Palmitoleate
TMZ+Palmitate+Sapienate
Cell Death Index (A.U)
Time (hrs.)
p<0.0001
p<0.0001

Figure 4.8: Palmitate influences temozolomide efficacy in newly diagnosed and recurrent GBMs.
(A-B) Cell death index (number of dead cells/confluence) over time in (**A)** newly diagnosed (CME 037) and **(B)** recurrent (CME 038) cells from GBM#1 with ±TMZ (250μM) and ±palmitate (100μM). Statistical analysis was performed using Two-way ANOVA with repeated measures and Sidak's multiple comparison. n=5. **(C)** CellEvent™ Caspase-3/7 based FACS analysis of caspase-active population (FITC+ve) in recurring GBM cells (CME 038) from GBM #1 (left) Cell counts vs FITC intensity in cells with/without TMZ (250 μM) and palmitate (100 μM) (right) Quantitation of the percentage of FITC +ve cells (caspase-active) with/without TMZ (250 μM) and palmitate (100 μM). TMZ treatment was done for 4 days, followed by 2 days of TMZ ± palmitate. Statistical analysis was performed using one-way ANOVA with Tukey's multiple comparison. n=3**. (D-E)** Cell death index (number of dead cells/confluence) over time in newly diagnosed (CME 037) cells from GBM#1 **(D)** without or **(E)** with TMZ (250μM) and ±palmitate (100μM), ± sapienate (100μM) or ±palmitoleate (100μM). Statistical analysis was performed using Two-way ANOVA with with repeated measures and Sidak's multiple comparison. n=5. **(F-G)** Cell death index (number of dead cells/confluence) over time in recurrent (CME 038) cells from GBM#1 **(F)** without or (**G)** with TMZ (250μM) and ±palmitate (100μM), ± sapienate (100μM) or ±palmitoleate (100μM). Statistical analysis was performed using Two-way ANOVA with repeated measures and Sidak's multiple comparison. n=5.

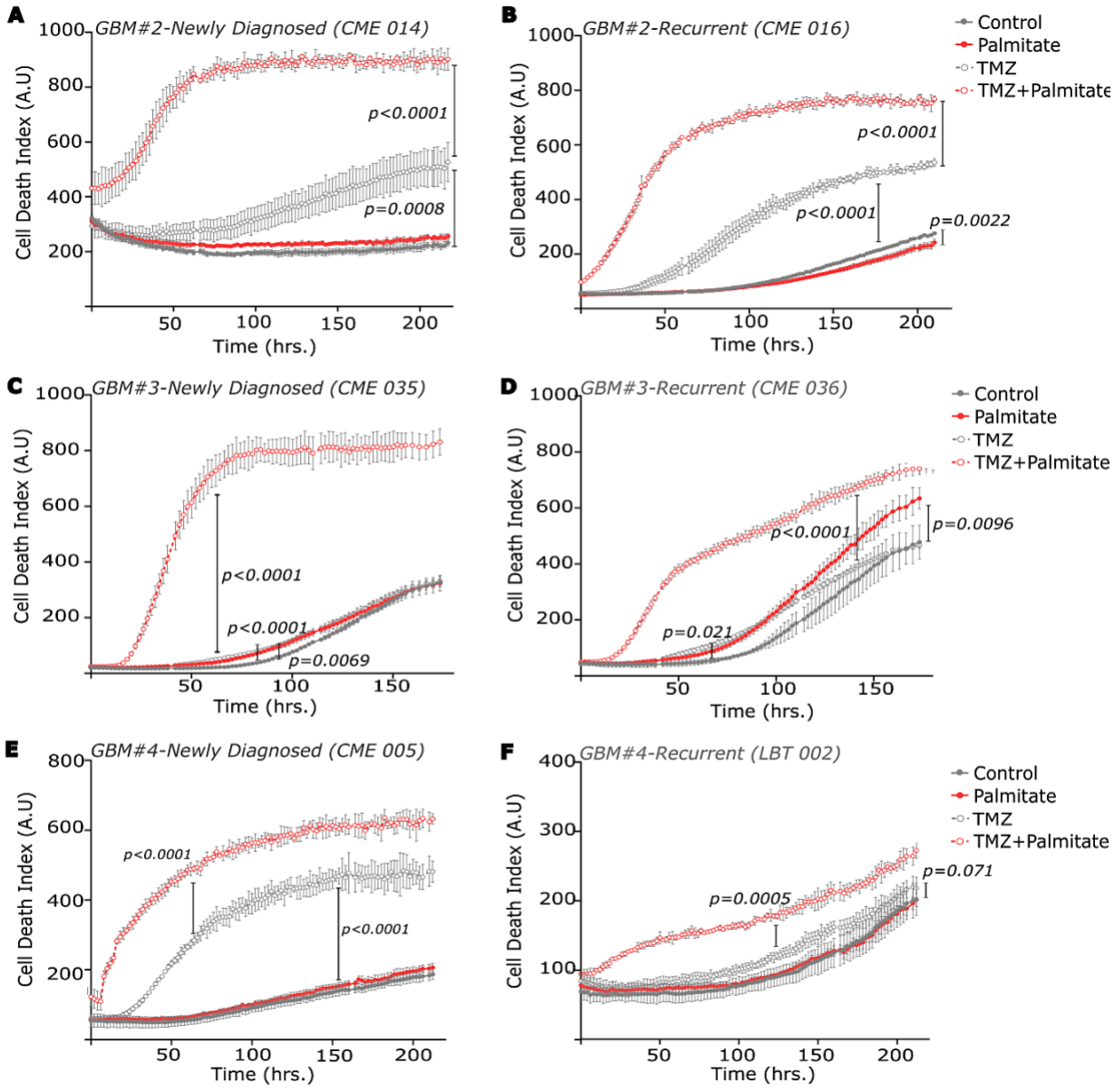

Figure 4.9: Palmitate influences temozolomide efficacy in newly diagnosed and recurrent GBMs.
(A-B) Cell death index (number of dead cells/confluence) over time in (A) newly diagnosed (CME 014) and (B) recurrent (CME 016) cells from GBM#2 with ±TMZ (250μM) and ±palmitate (100μM). Statistical analysis was performed using Two-way ANOVA with repeated measures and Sidak's multiple comparison. n=5. (C-D) Cell death index (number of dead cells/confluence) over time in (A) newly diagnosed (CME 035) and (B) recurrent (CME 036) cells from GBM#3 with ±TMZ (250μM) and ±palmitate (100μM). Statistical analysis was performed using Two-way ANOVA with repeated measures and Sidak's multiple comparison. n=5. (E-F) Cell death index (number of dead cells/confluence) over time in (A) newly diagnosed (CME 005) and (B) recurrent (LBT 002) cells from GBM#4 with ±TMZ (250μM) and ±palmitate

(100μM). Statistical analysis was performed using Two-way ANOVA with repeated measures and Sidak's multiple comparison. n=5.

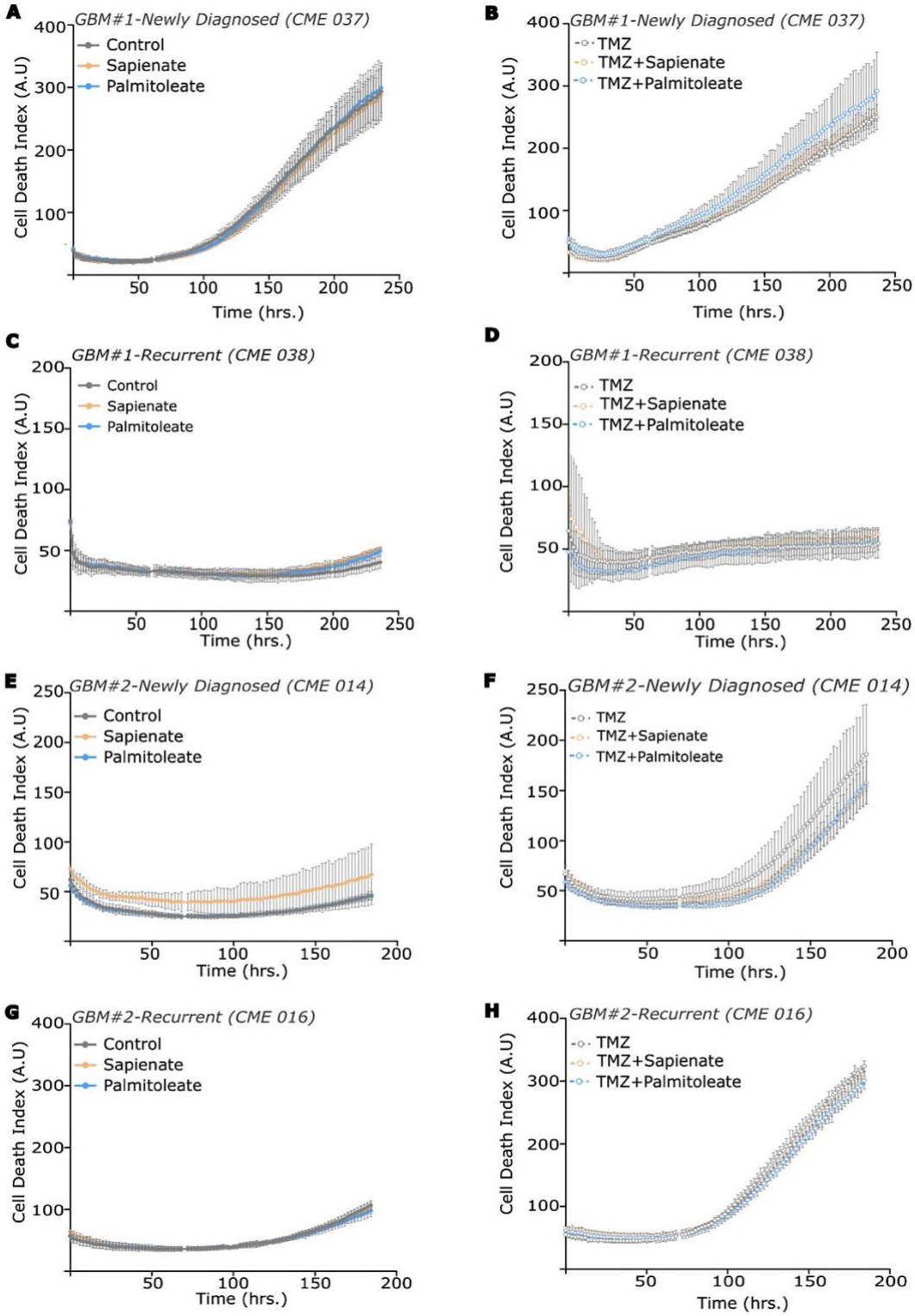

Figure 4.10: Palmitoleate and sapienate supplementation has no effect on temozolomide efficacy in newly diagnosed and recurrent GBMs.

(A-B) Cell death index (number of dead cells/confluence) over time in newly diagnosed (CME 037) cells from GBM#1 (C) without or (D) with TMZ (250μM) and ± sapienate (50μM) or ±palmitoleate (50μM). Statistical analysis was performed using Two-way ANOVA with repeated measures and Sidak's multiple comparison. n=5. Control plots same as that in Figure 4.8. (C-D) Cell death index (number of dead cells/confluence) over time in recurrent (CME 038) cells from GBM#1 (C) without or (D) with TMZ (250μM) and ± sapienate (50μM) or ±palmitoleate (50μM). Statistical analysis was performed using Two-way ANOVA with repeated measures and Sidak's multiple comparison. n=5. Control plots same as that in Figure 4.8. (E-F) Cell death index (number of dead cells/confluence) over time in newly diagnosed (CME 014) cells from GBM#2 (E) without or (F) with TMZ (250μM) and ± sapienate (50μM) or ±palmitoleate (50μM). Statistical analysis was performed using Two-way ANOVA with repeated measures and Sidak's multiple comparison. n=5. (G-H) Cell death index (number of dead cells/confluence) over time in recurrent (CME 016) cells from GBM#2 (G) without or (H) with TMZ (250μM) and ± sapienate (50μM) or ±palmitoleate (50μM). Statistical analysis was performed using Two-way ANOVA with repeated measures and Sidak's multiple comparison. n=5.

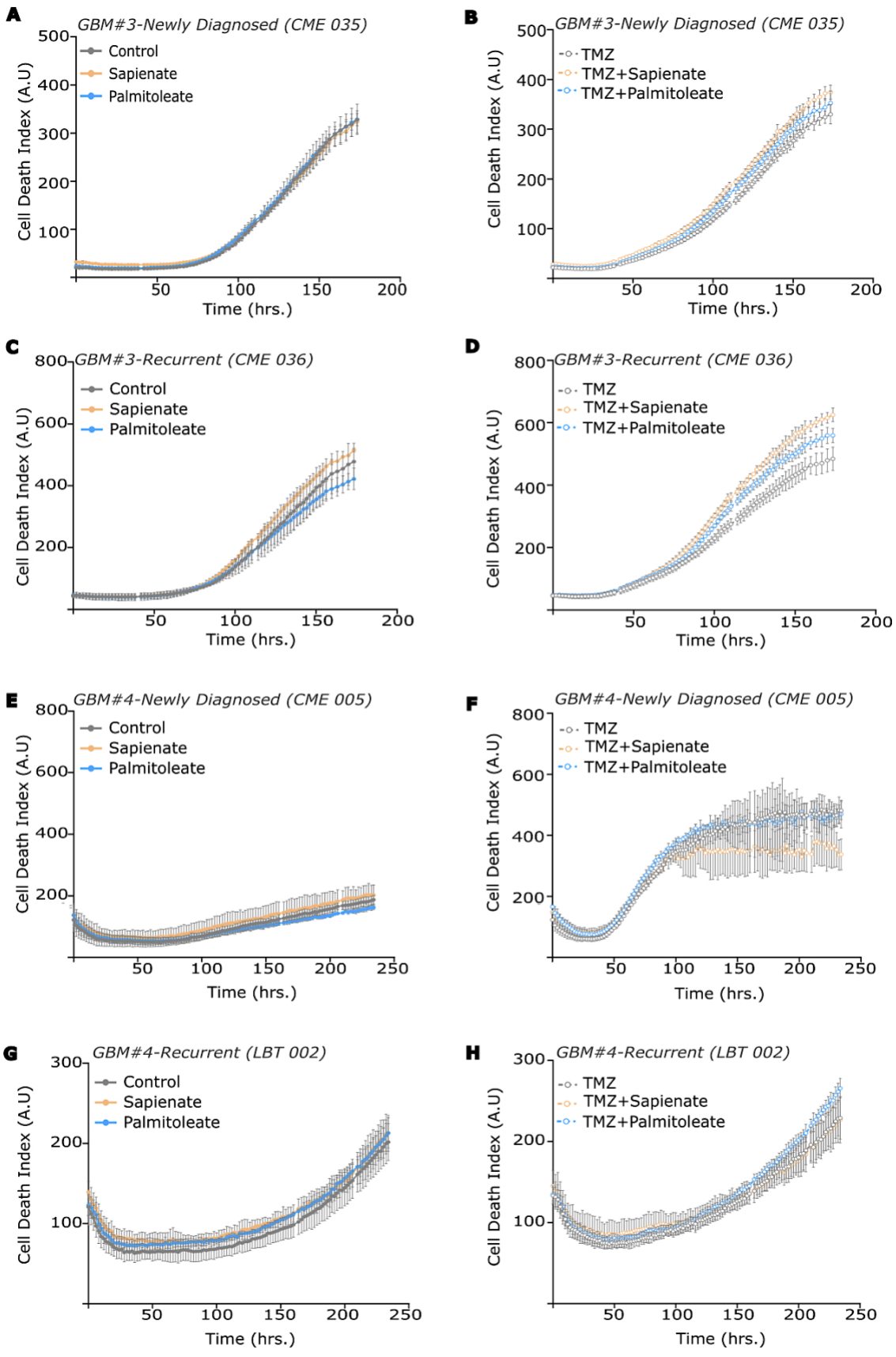
A
GBM#3-Newly Diagnosed (CME 035)
Control
Sapienate
Palmitoleate
Cell Death Index (A.U)
Time (hrs.)
B
GBM#3-Newly Diagnosed (CME 035)
TMZ
TMZ+Sapienate
TMZ+Palmitoleate
Cell Death Index (A.U)
Time (hrs.)
C
GBM#3-Recurrent (CME 036)
Control
Sapienate
Palmitoleate
Cell Death Index (A.U)
Time (hrs.)
D
GBM#3-Recurrent (CME 036)
TMZ
TMZ+Sapienate
TMZ+Palmitoleate
Cell Death Index (A.U)
Time (hrs.)
E
GBM#4-Newly Diagnosed (CME 005)
Control
Sapienate
Palmitoleate
Cell Death Index (A.U)
Time (hrs.)
F
GBM#4-Newly Diagnosed (CME 005)
TMZ
TMZ+Sapienate
TMZ+Palmitoleate
Cell Death Index (A.U)
Time (hrs.)
G
GBM#4-Recurrent (LBT 002)
Control
Sapienate
Palmitoleate
Cell Death Index (A.U)
Time (hrs.)
H
GBM#4-Recurrent (LBT 002)
TMZ
TMZ+Sapienate
TMZ+Palmitoleate
Cell Death Index (A.U)
Time (hrs.)

Figure 4.11: Palmitoleate and sapienate supplementation has no effect on temozolomide efficacy in newly diagnosed and recurrent GBMs.

(A-B) Cell death index (number of dead cells/confluence) over time in newly diagnosed (CME 035) cells from GBM#3 (C) without or (D) with TMZ (250μM) and ± sapienate (50μM) or ±palmitoleate (50μM). Statistical analysis was performed using Two-way ANOVA with repeated measures and Sidak's multiple comparison. n=5. (C-D) Cell death index (number of dead cells/confluence) over time in recurrent (CME 036) cells from GBM#3 (E) without or (F) with TMZ (250μM) and ± sapienate (50μM) or ±palmitoleate (50μM). Statistical analysis was performed using Two-way ANOVA with repeated measures and Sidak's multiple comparison. n=5. (E-F) Cell death index (number of dead cells/confluence) over time in newly diagnosed (CME 005) cells from GBM#4 (E) without or (F) with TMZ (250μM) and ± sapienate (50μM) or ±palmitoleate (50μM). Statistical analysis was performed using Two-way ANOVA with repeated measures and Sidak's multiple comparison. n=5. (G-H) Cell death index (number of dead cells/confluence) over time in recurrent (LBT 002) cells from GBM#4 (G) without or (H) with TMZ (250μM) and ± sapienate (50μM) or ±palmitoleate (50μM). Statistical analysis was performed using Two-way ANOVA with repeated measures and Sidak's multiple comparison. n=5.

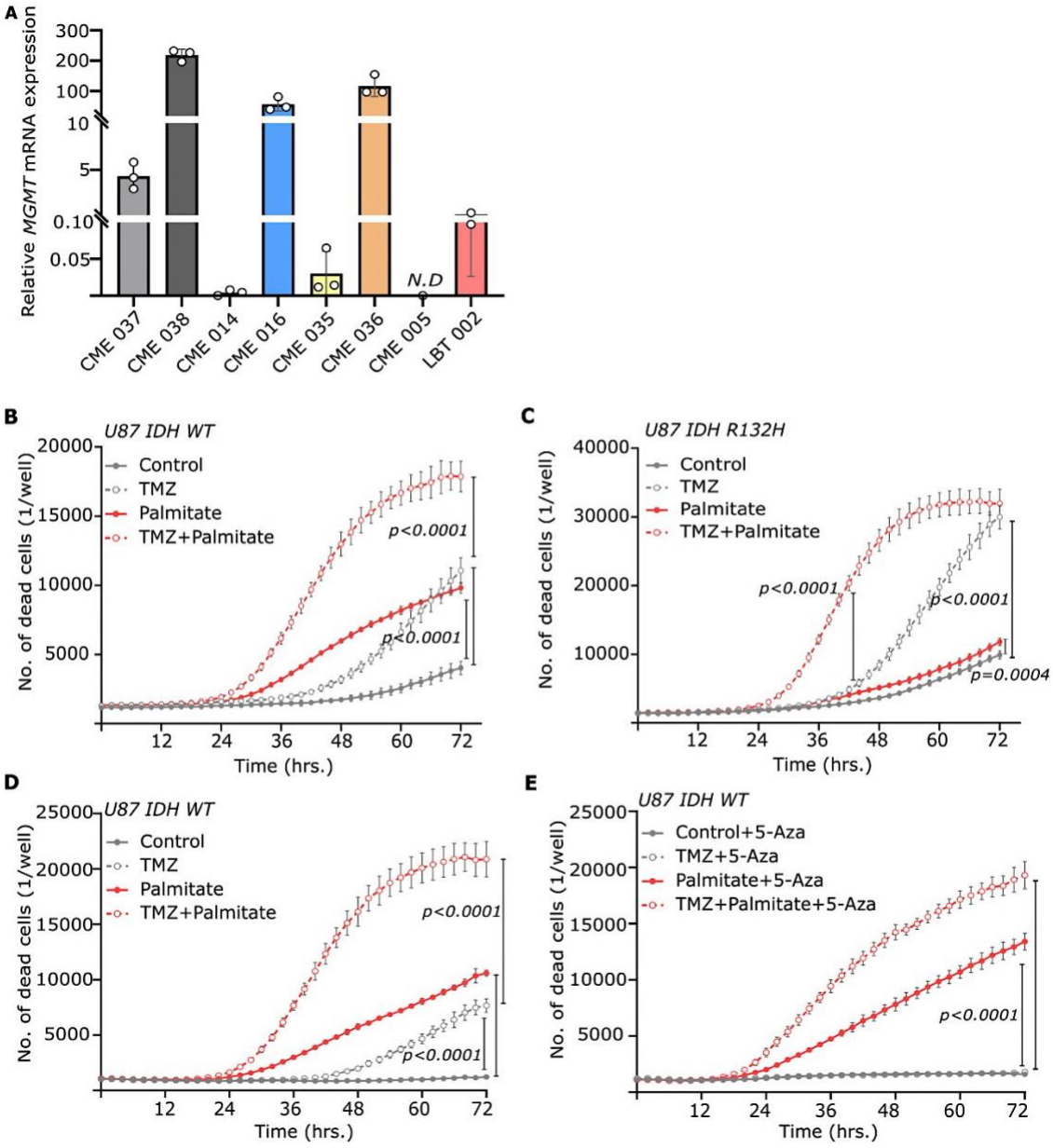

Figure 4.12: Palmitate influences temozolomide efficacy independent of common prognostic factors. (A) mRNA levels of MGMT in all cell lines. RPL19 was used as internal control. (B-C) No. of dead cells over time in (A) U87 IDH WT and (B) U87 IDH R132H cells with ±TMZ (250μM) and ±palmitate (100μM). Statistical analysis was performed using Two-way ANOVA with repeated measures and Sidak's multiple comparison. n=5. (D-E) No. of dead cells over time in U87 IDH WT cells (A)without and (B) with 5-azacytidine (5μM) and ±TMZ (250μM) or ±palmitate (100μM). Statistical analysis was performed using Two-way ANOVA with repeated measures and Sidak's multiple comparison. n=5.

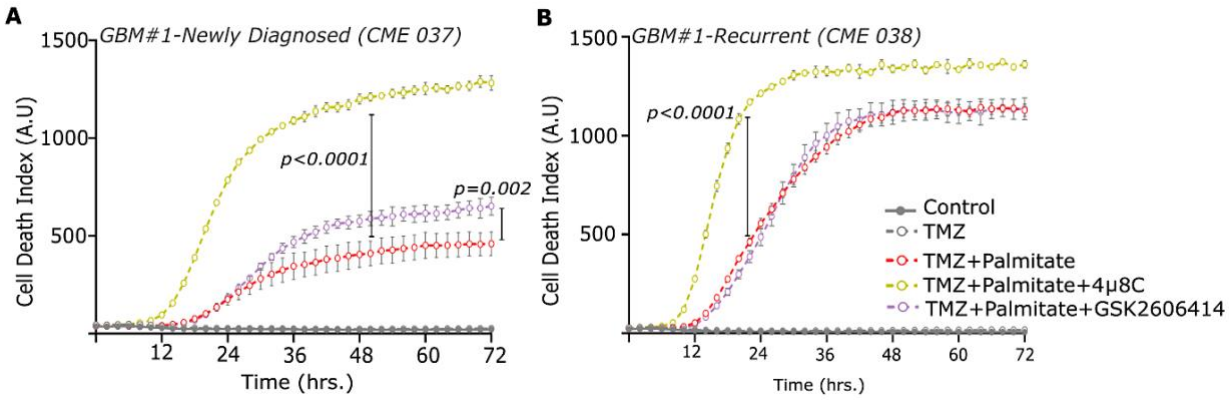

Figure 4.13: IRE1 or PERK pathways do not regulate palmitate mediated lipotoxicity in GBM cells.
(A) Cell death index (number of dead cells/confluence) over time in newly diagnosed (CME 037) cells from GBM#1 with ±TMZ (250μM) and ±palmitate (100μM), PERK inhibitor, GSK2606414 (25nM) and IRE1 inhibitor, 4μ8C (25μM). Statistical analysis was performed using Two-way ANOVA with repeated measures and Sidak's multiple comparison. n=5. (B) Cell death index (number of dead cells/confluence) over time in recurrent (CME 038) cells from GBM#1 with ±TMZ (250μM) and ±palmitate (100μM), PERK inhibitor, GSK2606414 (25nM) and IRE1 inhibitor, 4μ8C (25μM). Statistical analysis was performed using Two-way ANOVA with repeated measures and Sidak's multiple comparison. n=5.

SCD or FADS2 inhibition enhance temozolomide toxicity in GBM

Our observations show that disrupting intracellular FA balance in favor of the saturated fatty acid palmitate has a synergistic effect on TMZ toxicity in both newly diagnosed and recurring GBM cells. Therefore, we next investigated whether pharmacological interventions that accumulate intracellular palmitate may phenocopy the effect of palmitate supplementation. We treated cells with the SCD inhibitor Merck Cpd3j (2nM) or FADS2 inhibitor SC26196 (20μM) either alone or in combination with TMZ. FADS2 and SCD inhibition reduced the sapienate to palmitate and palmitoleate to palmitate ratios respectively, tipping the balance in favor of palmitate (Figure 4.14A-B). The reduction in the sapienate to palmitate ratio was slightly lower in recurrent GBM cells, which is in line with their higher baseline sapienate levels compared to cells from newly diagnosed GBM (Figure 4.15). We observed that both newly diagnosed and recurrent GBM cells were sensitive to FADS2 inhibition and insensitive to SCD inhibition (Figure 4.14C-F), which is in

line with our finding that glioblastoma cells display high FADS2 mono-desaturation activity leading to sapienate and polyunsaturated fatty acid production. However, when added in combination with TMZ, both the SCD and FADS2 inhibition led to a significant induction of cell death (Figure 4.14C-F). Most importantly, this effect was seen in both newly diagnosed and recurrent GBM. Accordingly, supplementation of sapienate partially rescued TMZ+FADS2 inhibition mediated cell death and palmitoleate completely rescued TMZ+SCD inhibition mediated cell death when added in combination with TMZ (Figure 4.16). Combining both SCD and FADS2 inhibition also led to dramatic induction of cell death in both newly diagnosed and recurrent GBM cells (Figure 4.14G-H). Thus, we concluded that both SCD and FADS2 inhibition increased TMZ induced cell death in cell lines derived from newly diagnosed but also reoccurring GBM tumors.

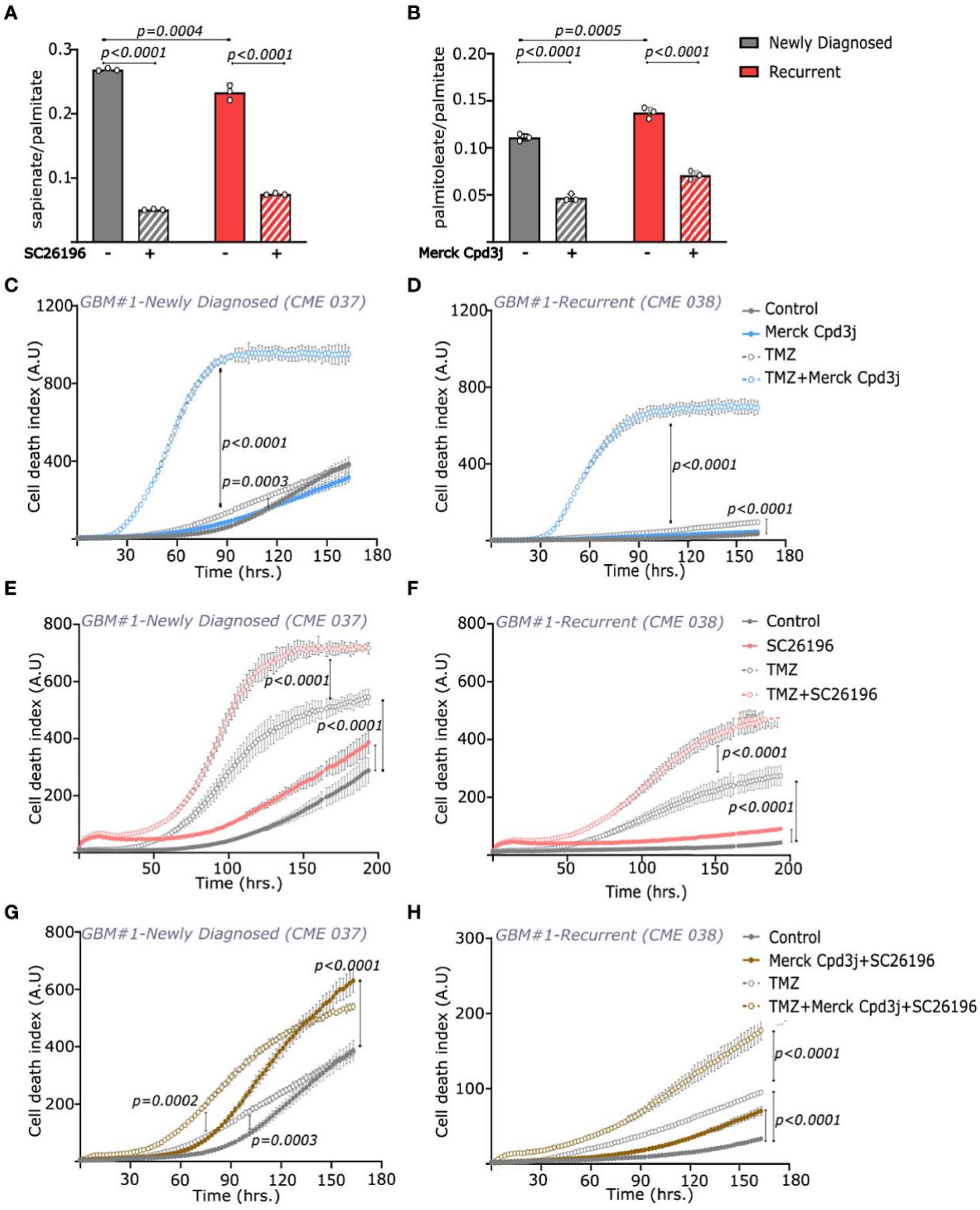
A
p=0.0004
p<0.0001
p<0.0001
sapienate/palmitate
0.3
0.2
0.1
SC26196 - + - +
B
p=0.0005
p<0.0001
p<0.0001
palmitoleate/palmitate
0.20
0.15
0.10
0.05
Merck Cpd3j - + - +
Newly Diagnosed
Recurrent
C
GBM#1-Newly Diagnosed (CME 037)
Cell death index (A.U)
1200
800
400
p<0.0001
p=0.0003
30 60 90 120 150 180
Time (hrs.)
D
GBM#1-Recurrent (CME 038)
Control
Merck Cpd3j
TMZ
TMZ+Merck Cpd3j
p<0.0001
p<0.0001
E
GBM#1-Newly Diagnosed (CME 037)
800
600
400
200
p<0.0001
p<0.0001
50 100 150 200
F
GBM#1-Recurrent (CME 038)
Control
SC26196
TMZ
TMZ+SC26196
p<0.0001
p<0.0001
G
GBM#1-Newly Diagnosed (CME 037)
p<0.0001
p=0.0002
p=0.0003
H
GBM#1-Recurrent (CME 038)
300
200
100
Control
Merck Cpd3j+SC26196
TMZ
TMZ+Merck Cpd3j+SC26196
p<0.0001
p<0.0001

Figure 4.14: FADS2 inhibition in combination with temozolomide induces cell death in newly diagnosed and recurrent GBMs.

(A) Sapienate and palmitate balance in newly diagnosed (CME 037) and recurrent (CME 038) cells from GBM#1 with and without FADS2 inhibitor, SC26196 (20μM). Statistical analysis was performed using Two-way ANOVA with Tukey's multiple comparison. n=3. (B) Palmitoleate and palmitate balance in newly diagnosed (CME 037) and recurrent (CME 038) cells from GBM#1 with and without SCD inhibitor, Merck Cpd3j (1nM). Statistical analysis was performed using Two-way ANOVA with Tukey's multiple comparison. n=3. (C-D) Cell death index (number of dead cells/confluence) over time in (C) newly diagnosed (CME 037) and (D) recurrent (CME 038) cells from GBM#1 ±TMZ (250μM) and ± SCD inhibitor, Merck Cpd3j (2nM). Statistical analysis was performed using Two-way ANOVA repeated measures and Sidak's multiple comparison. n=5. (E-F) Cell death index (number of dead cells/confluence) over time in (E) newly diagnosed (CME 037) and (F) recurrent (CME 038) cells from GBM#1 ±TMZ (250μM) and ± FADS2 inhibitor, SC26196 (20μM). Statistical analysis was performed using Two-way ANOVA with repeated measures and Sidak's multiple comparison. n=5. (G-H) Cell death index (number of dead cells/confluence) over time in (G) newly diagnosed (CME 037) and (H) recurrent (CME 038) cells from GBM#1 ±TMZ (250μM) and ± Merck Cpd3j (2nM)+SC26196 (20μM). Statistical analysis was performed using Two-way ANOVA with repeated measures and Sidak's multiple comparison. n=5.

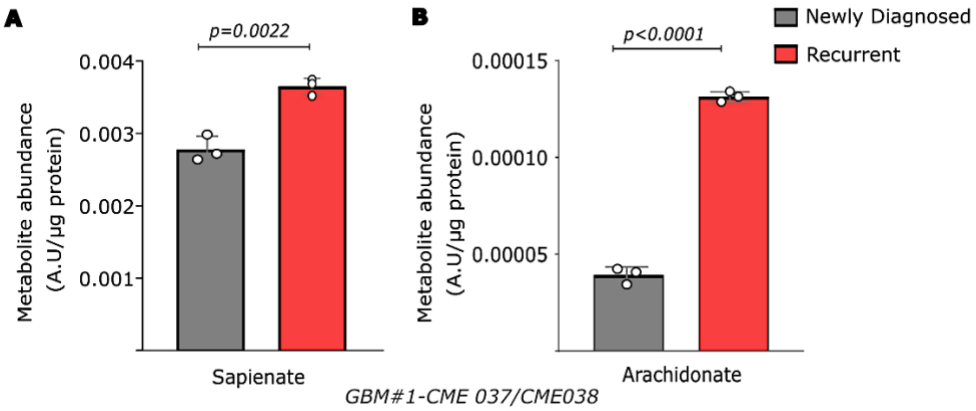

Figure 4.15: Patient-derived GBM cells produce sapienate over arachidonate *in vitro.*

(A) Metabolite levels of sapienate in newly diagnosed (CME 037) and recurrent (CME 038) cells from GBM#1. Statistical analysis was performed using unpaired two-tailed t-test. n=3. (B) Metabolite levels of arachidonate in newly diagnosed (CME 037) and recurrent (CME 038) cells from GBM#1. Statistical analysis was performed using unpaired two-tailed t-test. n=3.

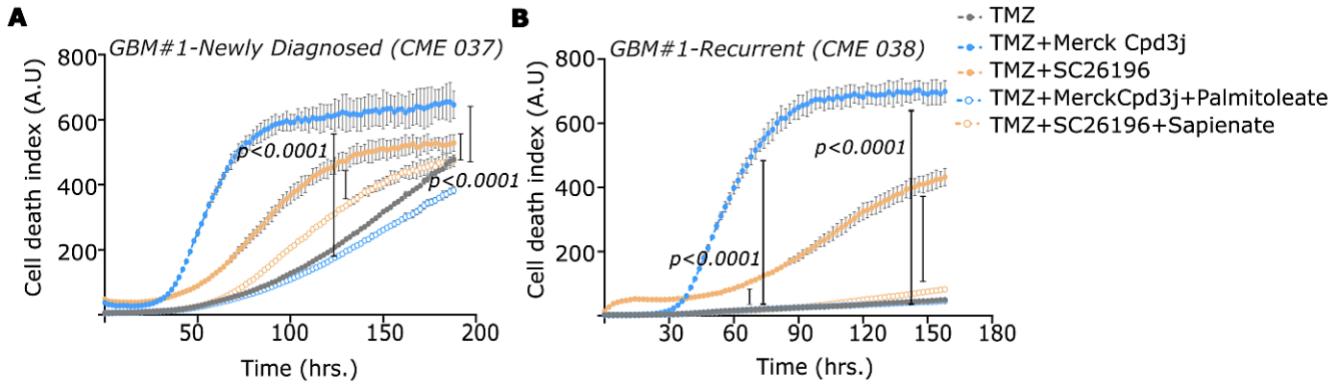

Figure 4.16: Supplementation of monounsaturated fatty acids rescue cell death induced by FADS2 and SCD inhibition with temozolomide.

(A) Cell death index (number of dead cells/confluence) over time in newly diagnosed (CME 037) cells from GBM#1 ±TMZ (250μM) and ± SCD inhibitor, Merck Cpd3j (2nM) with palmitoleate (50μM) or ± FADS2 inhibitor, SC26196 (20μM) with sapienate (50μM). Statistical analysis was performed using Two-way ANOVA repeated measures and Sidak's multiple comparison. n=5. (B) Cell death index (number of dead cells/confluence) over time in recurrent (CME 038) cells from GBM#1 ±TMZ (250μM) and ± SCD inhibitor, Merck Cpd3j (2nM) with palmitoleate (50μM) or ± FADS2 inhibitor, SC26196 (20μM) with sapienate (50μM). Statistical analysis was performed using Two-way ANOVA repeated measures and Sidak's multiple comparison. n=5.

Discussion

By combining single cell analysis on patient tissues and *in vitro* techniques, we identified that lipid metabolism plays a crucial role in glioblastoma (GBM). The gene expression levels of *FASN*, *SCD* and *FADS2* were highly heterogeneous in GBM cancer cells and correlated with cell fate. Activities of these key enzyme were reduced upon TMZ treatment but only in newly diagnosed and not recurrent GBM. Perturbing the cellular saturated to monounsaturated fatty acid balance either by extracellular supplementation of palmitate or by inhibition of SCD/FADS2 had a synergistic effect on TMZ treatment. Thus, our work highlights an observation that might be exploited to treat recurrent GBM.

Our study shows that cell fate in glioblastoma tissue is intimately linked with expression of fatty acid synthesis and processing genes, which define distinct sub-clusters within the larger cancer

cell population. This is in line with previous findings showing that FASN expression is correlated with stemness [261] and its inhibition induces apoptosis in patient derived GBM cells [262]. It was also shown that CD133^{+} glioma stem cells from *in vitro* cultured neurospheres display elevated FADS1 and FADS2 activities[263] and that SCD and FADS2 exhibit spatial heterogeneity with higher expression in the peritumoral area[264].

We find that disrupting the fatty acid balance to accumulate palmitate is very effective at mediating cell death in cultured GBM cells when used in combination with TMZ. While this has not been observed before, the mechanism of lipotoxicity is very consistent with previous work showing that the ratio of monounsaturated to saturated FAs regulates invasiveness and proliferation in melanoma cells[91]. In a pancreatic cancer model, increased availability of extracellular palmitate induces lipotoxic cell death and curbs tumor growth while SCD overexpression considerably increases it[115]. Lipotoxicity is contrasted by ferroptosis, [35,36] a pathway that is being targeted in several cancers[265,266]. Therein, polyunsaturated fatty acids (PUFAs) incorporated in membranes undergo oxidation and trigger an iron-mediated cell death [121,267]. Shifting fatty acid balance by external supplementation of monounsaturated fatty acids rescues ferroptosis [123] while depleting them via SCD or FADS2 inhibition augments it [126,268].

Disease recurrence remains the biggest challenge in GBM management and there is no standard of care for patients having reoccurring GBM [135,269]. Our findings imply that targeting fatty acid desaturation in combination with TMZ to accumulate toxic saturated fatty acids might prove beneficial to these patients. Further, the effect of palmitate accumulation was independent of disease status, DNA methylation status, MGMT levels, IDH status, all of which are crucial GBM prognostic factors and hinder with chemotherapy. Therefore, our data imply that palmitate accumulation might have therapeutic benefits in patients that do not respond to conventional therapy. Although it may seem paradoxical that higher levels of fatty acids might provide a survival advantage, a large number of studies has shown that higher BMI correlates with improved survival in glioblastoma patients [270–273], though this is contested by some other reports [274,275]. Moreover, fatty acid rich ketogenic diet also provides a survival advantage in glioblastoma [276]. Yet, it remains to be determined whether this is due to lipid accumulation in cancer cells or systemic effects. Enrichment of saturated fatty acids is not a feasible treatment option as they

can have a negative impact on patient health. Therefore, pharmacological means such as SCD and FADS2 inhibition are attractive targets and do extend survival in preclinical studies [66,67,99,248]. In addition, we have previously reported that a combination of SCD and FADS2 inhibition successfully curbs tumour growth in an orthotopic hepatocellular carcinoma model, albeit not necessarily involving the same mechanism [60]. Rudalska *et al* reported in HCC that induction of lipotoxicity by targeting SCD1 had a significant effect on tumour growth[113]. It would, therefore, be interesting to explore whether this treatment regimen would benefit other cancers beside GBM.

Chapter 5: Conclusion and Discussion

In this PhD thesis, we unraveled novel aspects of FA desaturation in cancer. Findings described in Chapter 3 show the existence of an alternative palmitate desaturation pathway that is novel to cancer cells, leading to the production of the unusual MUFA sapienate. The identification of this pathway was fueled by the observation that cancer cells display a range of sensitivity to SCD inhibition. Remarkably, we found that SCD inhibition-insensitive cells have higher sapienate production *via* FADS2 and *vice versa*. Finally, we showed that SCD inhibition dramatically reduced growth of orthoptic HCC tumors derived by transplantation of FADS2 silenced cells into nude mice. Further, HCC and NSCLC patients display elevated sapienate production specifically in tumor tissue.

FADS2-mediated sapienate production is well described in human sebocytes where it is the major component of human sebum and is mostly (~80%) synthesized *de novo* from glucose[277]. Reducing sebum sapienate content by ACC inhibition has indeed been suggested as a treatment option for *acne vulgaris*[277]. Prior to our study, sapienate production was thought to be exclusive to humans and more specifically to sebocytes[278]. We demonstrate that firstly, sapienate production is activated in cancers as compared to normal tissues and secondly, mouse cancer tissues also produce sapienate. Subsequent to our study, Young and colleagues have extended these findings showing that cancer cells may even display SCD, FADS2 and FADS1 promiscuous activity leading to the production of several unusual MUFAs and PUFAs[279]. Among other novel activities, FADS2 unexpectedly carries out Δ8-desaturation of stearate to produce an (18:1 n-10) FA, highlighting the metabolic flexibility of desaturation in cancers. The authors also showed that these FAs were incorporated into membrane phospholipids, indicating that, like we showed for sapienate, these atypical fatty acids do in fact impact cell physiology.

As discussed before, membrane FA composition is a critical determinant of cell signaling and survival, making it conceivable that these atypical FAs impact membrane dynamics. A recent study by Lee and colleagues confirms this hypothesis. The authors showed that metastasizing melanoma cells upregulate sapienate production, which in turn increases membrane fluidity and permits metastasis. Inhibition of FADS2 with the specific inhibitor SC26196 reduced melanoma

cell migration and reduced membrane fluidity *in vitro* and FADS2 KD cells injected *via* the tail vein formed ~68% lower lung metastases. Interestingly, palmitoleate addition or SCD inhibition failed to have the same effect on membrane fluidity, indicating specificity of FADS2 in melanoma cells[280]. When exploring FADS2 targeting as a therapeutic option in melanoma, one must however keep in mind the sapienate production ability of sebocytes. It will be interesting to investigate whether melanoma cells take up sapienate from skin sebum.

In addition to its role in FA production, FADS2 modulation also has other metabolic implications. Desaturation reactions catalyzed by FADS1/2 involve the regeneration of NAD+ from NADH[281]. Kim and colleagues found that *in vitro* treatments that reduced cellular NAD/NADH ratio promoted an increase in FADS1 and FADS2 activities, consequently increasing PUFA content. The authors also showed the evidence of this in humans by analyzing the PUFA content of individuals with mutations in *SLC6A11* (a pyruvate transporter) that is a risk factor for type 2 diabetes. These individuals did in fact show elevated PUFA content[281], highlighting the association of lipid metabolism and metabolic disorders.

Following our report, another study from the Fendt Lab showed that FADS2 and SCD are transcriptionally regulated by sterol-response element binding protein (SREBP). SREBP1/2 are master transcriptional activators of fatty acid and sterol biogenesis. They bind to sterol-response elements (SREs) upstream to promoters of their target genes, including SCD, ACLY, FASN and LDLR. SREBP's role and its inhibition has indeed been investigated in several cancers[282]. Surprisingly, studies showed that SREBP targeting induces lipotoxicity induced *via* increase in the SFA-to-UFA ratio, leading to a reduced tumor growth in a GBM xenograft model[283,284]. Another study by Guo and colleagues showed that EGFR-amplified GBMs are sensitive to SREBP targeting and SREBP silenced tumors show reduced tumor growth[285]. Interestingly, this effect was amplified when mice were simultaneously administered atorvastatin, a hydroxymethylglutaryl coA reductase inhibitor[285]. This highlights that indeed the effect of SREBP targeting can, at least in part, be attributed to reduced sterol synthesis. Triki and colleagues observed that the FADS2 promoter features SREs and indeed SREBP activates FADS2 transcription, highlighting SREBP as the transcriptional activator of both SCD and FADS2[128]. In this study, the authors also found that

GBMs are highly sapienate-dependent. Building on this, we next went on to investigate the role of FA desaturation in GBM.

As discussed before, GBM is a particularly challenging tumor with very poor survival rate[140]. Recurrent tumors, which are less sensitive to therapy, ultimately cause patient death and therefore, we focused on studying newly diagnosed as well as recurrent GBMs. Another major challenge in targeting GBMs has been that tumors are very heterogeneous, so we first started with addressing this in our study. We found that GBM tumors displayed tremendous heterogeneity in their lipid metabolism, with specific genes in the FA metabolic pathway correlating with distinct cell states. Further, we showed that TMZ treatment reduces FA synthesis and desaturation in newly diagnosed GBMs. Elevating intracellular palmitate levels by exogenous supplementation or SCD and/or FADS2 targeting synergizes with TMZ and dramatically induces cell death in pair-matched newly diagnosed and recurrent patient-derived GBM cell lines.

The dry weight of human brain is ~50% lipids but most of this is housed in structural elements such as myelin sheaths and neural tissue, with an abundance of phospholipid-bound LC-PUFAs such as arachidonic acid, docosahexaenoic acid and eicosapentaenoic acid[286]. Absolute quantification of FAs in murine CSF indicates that given the high lipid requirement of brain cells, little is left for the brain microenvironment. We propose that this environment rewires the GBM lipid metabolism, making them reliant on *de novo* FA synthesis, rather than uptake. This has indeed been demonstrated recently for ER^+ breast cancer cells metastasizing to the brain. Ferraro and colleagues found that breast cancer cells upregulate FASN when metastasizing to the brain owing to the lipid-depleted microenvironment. Indeed, FASN silencing markedly reduced the growth of brain metastases, without affecting the primary tumor[250].

We identified that only newly diagnosed (ND) but not recurrent (RC) GBM cells downregulate FASN, SCD and FADS2 activities upon TMZ treatment. We do not yet, however, understand the mechanistic basis of this regulation. A potential mechanism could be that TMZ treatment in ND GBM cells downregulates SREBP, the transcriptional activator of SCD, FADS2 and FASN. SREBP is indeed upregulated in GBM and its expression is associated with poor prognosis in GBM patients[287]. Simultaneously with our study, Choo and colleagues showed that TMZ resistant GBM

cells show elevated SREBP levels and that treatment with fatostatin, an SREBP inhibitor induces death in TMZ-resistant cells *in vitro*[288]. Targeting of SREBP has been suggested for several cancers, including GBM and continues to be explored[289].

We then identified that extracellular palmitate synergizes with TMZ and dramatically induces cell death in both ND and RC GBM cells, while the MUFAs palmitoleate and sapienate had no effect. We also found that the PUFAs linoleate or arachidonic acid had no effect on TMZ sensitivity either, while the SFA stearate increased TMZ sensitivity as well (data not shown). These findings clearly indicate that the accumulation of SFAs, in particular, synergize with TMZ in GBM cells indicating lipotoxic cell death. Curiously, however, in our model, palmitate supplementation was not associated with activation of the ER stress response. As hinted by a global lipidomic analysis of palmitate supplemented cells by Piccolis and colleagues, the cellular lipotoxic response is a global change accompanied by the alteration of several cellular pathways[112]. Future global metabolomic studies performing such analyses will certainly provide better insight into the lipotoxic response.

The role of diet itself in cancer cannot be overlooked and obesity has been identified as a risk factor for many cancers[290,291]. Paradoxically, our findings suggest that GBM patients with higher body mass index (BMI) would show improved survival. Several multi-patient studies have confirmed this hypothesis, while one study opposes it[270,272–274,292,293]. A criticism of these studies is the use of BMI, which may not perfectly reflect body fat content, as a stratification criterion. Perhaps the use of parameters such as waist circumference and body fat percentage, which better reflect body fat content, may provide further clarification of these discrepancies. Another contributing factor to this may be that, rather than a general increase in FAs, a specific increase in saturated FAs mediates the synergistic effect. We have indeed observed that GBM cells, when cultured in high serum conditions (which has ~550μM of palmitate[60]), have reduced sensitivity to TMZ compared to reduced serum culture conditions (data not shown). This suggests that an overall increase in extracellular FAs does not elicit the same effect as increased palmitate and rather has the opposite effect.

Further, our findings hint that, clinically, palmitate supplementation may be beneficial in addition to TMZ. However, a palmitate-rich diet will certainly have adverse systemic consequences. A high SFA diet promotes systemic metabolic dysfunction including hepatic and cardiovascular dysfunction[294]. These widespread systemic effects are a concern, making such dietary regimens rather harmful for patients. An alternative to this is pharmacological interventions that accumulate intracellular palmitate. FADS2 and SCD are both elevated in cancer cells and their inhibition is well tolerated in pre-clinical models. Rather, mice lacking these proteins are protected from hyperlipidemia and diet-induced obesity[295,296]. Therefore, pharmacological targeting of these proteins is a more clinically translatable suggestion. Our study shows that dual silencing of these proteins induced reduction of hepatocellular carcinomas and patient-derived GBM cells. In the future, it will be interesting to examine the effects of administration of combined SCD and FADS2 inhibitors in cancers.

Overall, findings presented in this thesis clearly reflect the therapeutic potential of targeting FA monodesaturation in cancer and provide strong evidence for *in vitro* as well as pre-clinical implementation of this regimen. In the future, it will be of crucial importance to investigate the *in vivo* implications of this treatment regimen, not only in hepatocellular carcinoma, adenocarcinoma and glioblastoma, but also in other primary cancers and metastases.

Acknowledgements, personal contribution and conflict of interest statements

Author list

Chapter 3:

Kim Vriens[1,2,28], Stefan Christen[1,2,28], **Sweta Parik[1],2,3,4**, Dorien Broekaert[1,2,] Kazuaki Yoshinaga[5,6], Ali talebi[7], Jonas Dehairs[7], Carmen escalona-Noguero[1,2], Roberta Schmieder[1,2], Thomas Cornfield[8], Catriona Charlton[8], Laura romero-Pérez[9], Matteo Rossi[1,2], Gianmarco Rinaldi[1,2], Martin F. Orth[9], Ruben Boon[10], Axelle Kerstens[11,12], Suet Ying Kwan[13], Brandon Faubert[14], Andrés Méndez-Lucas[15], Charlotte C. Kopitz[16], Ting Chen[17], Juan Fernandez-Garcia[1,2], João A. G. Duarte[1,2], Arndt A. Schmitz[16], Patrick Steigemann[16], Mustapha Najimi[18], Andrea Hägebarth[16], Jo A. Van Ginderachter[3,4], Etienne Sokal[18], Naohiro Gotoh[19], Kwok-Kin Wong[17], Catherine Verfaillie[10], Rita Derua[20], Sebastian Munck[11,12], Mariia Yuneva[15], Laura Beretta[13], Ralph J. DeBerardinis[14,21], Johannes V. Swinnen[7], Leanne Hodson[8], David Cassiman[22,23], Chris Verslype[22,24], Sven Christian[16], Sylvia Grünewald[16], Thomas G. P. Grünewald[9,25,26,27] & Sarah-Maria Fendt[1,2*]

[1]Laboratory of Cellular Metabolism and Metabolic Regulation, VIB-KU Leuven Center for Cancer Biology, VIB, Leuven, Belgium. 2Laboratory of Cellular Metabolism and Metabolic Regulation,

[2]Department of Oncology, KU Leuven and Leuven Cancer Institute (LKI), Leuven, Belgium.

[3]Laboratory of Cellular and Molecular Immunology, Vrije Universiteit Brussel, Brussels, Belgium.

[4]Myeloid Cell Immunology Laboratory, VIB Center for Inflammation Research, Brussels, Belgium.

[5]Tsukishima Foods Industry, Tokyo, Japan.

[6]Cluster of Agricultural Sciences, Faculty of Food and Agricultural Sciences, Fukushima University, Fukushima, Japan.

[7]Laboratory of Lipid Metabolism and Cancer, Department of Oncology, Leuven Cancer Institute (LKI), Leuven, Belgium.

[8]The Oxford Centre for Diabetes, Endocrinology and Metabolism, Radcliffe Department of Medicine, University of Oxford, Churchill Hospital, Oxford, UK.

[9]Max-Eder Research Group for Pediatric Sarcoma Biology, Institute of Pathology, Faculty of Medicine, LMU Munich, Munich, Germany.

[10]Stem Cell Institute, Department of Development and Regeneration, KU Leuven, Leuven, Belgium.

[11]VIB Bio Imaging Core and VIB-KU Leuven Center for Brain & Disease Research, KU Leuven, Leuven, Belgium.

[12]Molecular Neurobiology, Department of Neuroscience, KU Leuven, Leuven, Belgium.

[13]Department of Molecular and Cellular Oncology, University of Texas MD Anderson Cancer Center, Houston, TX, USA.

[14]Children's Medical Center Research Institute, UT Southwestern, Dallas, TX, USA.

[15]The Francis Crick Institute, London, UK.

[16]Bayer AG, Research & Development, Pharmaceuticals, Berlin, Germany.

[17]Perlmutter Cancer Center, NYU Langone Medical Center, Smilow Research Center New York, NY, USA.

[18]Laboratory of Pediatric Hepatology and Cell Therapy, Institut de Recherche Expérimentale et Clinique (IREC), Université Catholique de Louvain and Cliniques Universitaires St Luc, Brussels, Belgium.

[19]Department of Food Science and Technology, Tokyo University of Marine Science and Technology, Tokyo, Japan.

[20]Laboratory of Protein Phosphorylation and Proteomics, Department of Cellular and Molecular Medicine, KU Leuven, Leuven, Belgium.

[21]Howard Hughes Medical Institute, UT Southwestern Medical Center, Dallas, TX, USA.

[22]Department of Hepatology, KU Leuven, Leuven, Belgium.

[23]Department of Chronic Diseases, Metabolism and Ageing, KU Leuven, Leuven, Belgium.

[24]Department of Digestive Oncology, KU Leuven, Leuven, Belgium.

[25]Institute of Pathology, Faculty of Medicine, LMU Munich, Munich, Germany.

[26]German Cancer Consortium (DKTK), Partner site Munich, Munich, Germany.

[27]German Cancer Research Center (DKFZ), Heidelberg, Germany.

[28]These authors contributed equally: Kim Vriens, Stefan Christen.

*e-mail: sarah-maria.fendt@kuleuven.vib.be

Chapter 4:

Sweta Parik[1,2,3,4], Juan Fernández-García[1,2], Francesca Lodi[5,6], Karen De Vlaminck[3,4], Marleen Derweduwe[7], Steven De Vleeschouwer[8], Raf Sciot[9], Wietse Geens[10], Linqian Weng[11], Francesca Maria Bosisio[9,12], Gabriele Bergers[11,13], Johnny Duerinck[10], Frederick De Smet[7], Diether Lambrechts[5,6], Jo A. Van Ginderachter[3,4], Sarah-Maria Fendt[1,2]*

[1]Laboratory of Cellular Metabolism and Metabolic Regulation, VIB-KU Leuven Center for Cancer Biology, VIB, Leuven, Belgium

[2]Laboratory of Cellular Metabolism and Metabolic Regulation, Department of Oncology, KU Leuven and Leuven Cancer Institute (LKI), Leuven, Belgium

[3]Laboratory of Cellular and Molecular Immunology, Vrije Universiteit Brussel, Brussels, Belgium

[4]Myeloid Cell Immunology Laboratory, VIB Center for Inflammation Research, Brussels, Belgium

[5]Laboratory for Translational Genetics, VIB-KU Leuven Center for Cancer Biology, VIB, Leuven, Belgium

[6]Laboratory for Translational Genetics, Department of Human Genetics, KU Leuven, Leuven, Belgium

[7]Laboratory for Precision Cancer Medicine, Translational Cell and Tissue Research, Department of Imaging & Pathology, KU Leuven, Leuven, Belgium

[8]Department of Neurosurgery, University Hospital Leuven, Belgium

[9]Department of Pathology, University Hospitals Leuven, KU Leuven, 3000 Leuven, Belgium

[10]Department of Neurosurgery, UZ Brussel, Jette, Belgium.

[11]Laboratory of Tumor Microenvironment and Therapeutic Resistance, VIB-KU Leuven Center for Cancer Biology, VIB, Leuven, Belgium

[12]Department of Imaging and Pathology, Laboratory of Translational Cell & Tissue Research

[13]Department of Neurological Surgery, UCSF Comprehensive Cancer Center, University of California San Francisco (UCSF), San Francisco, CA, United States.

*** Correspondence:**

Sarah-Maria Fendt

sarah-maria.fendt@kuleuven.be

Author Contributions

Chapter 3:

Investigation and validation, K.V., S. Christen and **S.P.** generated knockdown and overexpression cell lines; K.V., S. Christen, **S.P**.,D.B., C.E.-N. and L.R.-P. quantified FADS2 gene expression; K.V., S. Christen and **S.P.** performed growth and labelling experiments; growth experiments were reproduced independently; K.V. and S. Christen performed reverse labelling experiments; K.V., S. Christen, **S.P.,** D.B. and R.S. performed metabolite extractions; K.V., S. Christen, R.S. and K.Y. performed metabolite measurement; K.V., **S.P.,** G.R. and M.R. analysed FADS2 protein data; T. Cornfield, C.C. and L.H. analysed phospholipid-bound sapienate and palmitoleate; A.T. and J.D. performed phospholipidomic analysis and assessed lipid peroxidation sensitivity; A.K. analysed

membrane fluidity; K.V., D.B., R.S. and C.C.K. performed mouse experiments; K.V., M.F.O., B.F., R.J.D., D.C., C. Verslype and T.G.P.G. collected and assessed human clinical samples. T.G.P.G. and M.F.O. performed haematoxylin and eosin staining. In formal analysis, K.V., S. Christen and S.-M.F. interpreted all data, except data from haematoxylin and eosin staining, which were interpreted by T.G.P.G. and M.F.O. The following authors provided resources: M.N. and E.S. provided primary hepatocytes; R.B. and C. Verfaillie advised on genetic engineering and primary hepatocytes; B.F. and R.J.D. provided human lung tissue and plasma samples; D.C., C. Verslype, S. Christian, S.G., A.S. and T.G.P.G. provided human liver tissue and plasma samples; N.G., J.V.S. and L.H. advised on lipid and fatty acid analysis. S.M. advised on membrane fluidity; R.D., J.F.-G. and J.A.G.D. supported the development of the mass spectrometry method; A.M.-L., M.Y., S.Y.K. and L.B. provided liver tissue and plasma from genetic mouse models; and A.S., P.S., A.H., J.A.V.G., S. Christian, S.G., A.S., T. Chen, K.-K.W. provided reagents. S.-M.F. advised on experiments and analysis. This work was conceptualized by K.V., S. Christen and S.-M.F. K.V. provided visualization. S.-M.F. wrote the original draft, which was reviewed and edited by K.V., S. Christen and S.-M.F. S.-M.F. supervised this work and acquired funding.

Chapter 4:

S-M.F. and **S.P.** designed the study; **S.P** conducted the experiments and analyzed data; J.F.G and F.L analyzed the single-cell sequencing data. K.D.V isolated blood and cerebrospinal fluid from mice. M.D, S.D.V and R.S collected generated patient-derived GBM cells. W.G assisted with collection of human GBM tumors. L.W assisted with analysis of single-cell sequencing data. **S.P**, S-M.F and J.V.G wrote and edited the manuscript. S-M.F. and J.V.G supervised the study. All authors read and approved the final manuscript.

Conflict of interest

Chapter 3:

A.H., C.C.K., A.S., P.S., S. Christian and S.G. have competing interests as employees of Bayer AG. K.-K.W. is a founder and equity holder of G1 Therapeutics and he has Consulting/Sponsored

Research Agreements with AstraZeneca, Janssen, Pfizer, Array, Novartis, Merck, Takeda, Ono, Targimmune and BMS. S.-M.F. has received research funding from Bayer AG and Merck.

Chapter 4:

S-MF has received funding from Bayer AG, Merck and Black Belt Therapeutics, has consulted for Fund+ and is in the advisory board of Alesta Therapeutics. JVG collaborates with Montis and has consulted for Fund+. All other authors declare no conflict of interest.

Scientific acknowledgements

Chapter 3:

We thank all patients and volunteers as well as J. van Pelt, I. Vander Elst and P. Windmolders for advice on the orthotopic injections and patient sample collection; F. Impens and D. Van Haver (VIB Proteomics Core); V. van Hoef (VIB-CCB Bioinformatics Expertise Center); and D. Nittner (VIB-CCB Histology Expertise Center). S.P. is supported by a VIB International PhD student fellowship. G.R. is supported by Kom op tegen Kanker and FWO fellowships. R.S., M.R., J.F.-G. and J.A.G.D. are supported by FWO fellowships. R.J.D., a Howard Hughes Medical Institute Investigator, Joel B. Steinberg, M.D. Chair in Pediatrics and Robert L. Moody, Sr. Faculty Scholar at UT Southwestern, are funded by CPRIT (RP160089) and the National Cancer Institute (R35CA22044901). T.G.P.G. is funded by the German Cancer Aid (DKH-111886, DKH-70112257), LMUexcellent, Bettina-Bräu-Stiftung, Dr. Leopold und Carmen Ellinger, MatthiasLackas, Walter Schulz, Wilhelm Sander (2016.167.1), Gert & Susanna Mayer Foundations, and the Deutsche Forschungsgemeinschaft (DFG 391665916). S.-M.F. is funded by the European Research Council under the ERC Consolidator Grant Agreement n.771486–MetaRegulation and Marie Curie CIG n.617727-MetabolismConnect, FWO Odysseus II, KU Leuven Methusalem Co-funding, and Bayer AG.

Chapter 4:

We thank all patients for their valuable contribution. We thank all members of Fendt lab and van Ginderachter lab for their feedback. S.P. received an international PhD scholarship from VIB. J.F.-

G. is an FWO postdoctoral fellow JVG is supported by iBOF, EOS, FWO, Stichting tegen Kanker, Kom op tegen Kanker and EU-Innovative Medicines Initiative research grants. S-MF acknowledges funding from the European Research Council under the ERC Consolidator Grant Agreement n. 771486–MetaRegulation, FWO – Research Projects, KU Leuven – FTBO, King Baudouin Foundation, Beug Foundation, Stichting tegen Kanker and Fonds Baillet Latour.

References

1. Hanahan, D. & Weinberg, R. A. Hallmarks of cancer: the next generation. *Cell* **144**, 646–674 (2011).

2. Koundouros, N. & Poulogiannis, G. Reprogramming of fatty acid metabolism in cancer. *British Journal of Cancer* vol. 122 4–22 Preprint at https://doi.org/10.1038/s41416-019-0650-z (2020).

3. Nagarajan, S. R., Butler, L. M. & Hoy, A. J. The diversity and breadth of cancer cell fatty acid metabolism. *Cancer & Metabolism 2021 9:1* **9**, 1–28 (2021).

4. Zhao, W. *et al.* Tumor and Stem Cell Biology Candidate Antimetastasis Drugs Suppress the Metastatic Capacity of Breast Cancer Cells by Reducing Membrane Fluidity. *Cancer Res* **76**,.

5. Heilos, D. *et al.* Altered membrane rigidity via enhanced endogenous cholesterol synthesis drives cancer cell resistance to destruxins. *Oncotarget* **9**, 25661–25680 (2018).

6. Bi, J. *et al.* Oncogene Amplification in Growth Factor Signaling Pathways Renders Cancers Dependent on Membrane Lipid Remodeling. *Cell Metab* **30**, 525-538.e8 (2019).

7. Li, J. *et al.* Ferroptosis: past, present and future. *Cell Death and Disease* vol. 11 Preprint at https://doi.org/10.1038/s41419-020-2298-2 (2020).

8. Dillon, L. M. & Miller, T. W. Therapeutic targeting of cancers with loss of PTEN function. *Curr Drug Targets* **15**, 65 (2014).

9. Ma, chi *et al.* NAFLD causes selective CD4 + T lymphocyte loss and promotes hepatocarcinogenesis. (2016) doi:10.1038/nature16969.

10. Wang, D. & Dubois, R. N. Eicosanoids and cancer. *Nature Reviews Cancer 2010 10:3* **10**, 181–193 (2010).

11. Ko, P. & Dixon, S. J. Protein palmitoylation and cancer. *EMBO Rep* **19**, (2018).

12. Bollu, L. R. *et al.* Intracellular activation of EGFR by fatty acid synthase dependent palmitoylation. *Oncotarget* **6**, 34992 (2015).

13. Mikalayeva, V. *et al.* Fatty Acid Synthesis and Degradation Interplay to Regulate the Oxidative Stress in Cancer Cells. *Int J Mol Sci* **20**, (2019).

14. Li, M., Xian, H. chun, Tang, Y. J., Liang, X. hua & Tang, Y. ling. Fatty acid oxidation: driver of lymph node metastasis. *Cancer Cell International 2021 21:1* **21**, 1–13 (2021).

15. Camarda, R. *et al.* Inhibition of fatty acid oxidation as a therapy for MYC-overexpressing triple-negative breast cancer. *Nature Medicine 2016 22:4* **22**, 427–432 (2016).

16. Duman, C. *et al.* Acyl-CoA-Binding Protein Drives Glioblastoma Tumorigenesis by Sustaining Fatty Acid Oxidation. *Cell Metab* **30**, 274-289.e5 (2019).

17. Lee, C. kun *et al.* Tumor metastasis to lymph nodes requires YAP-dependent metabolic adaptation. *Science (1979)* **363**, 644–649 (2019).

18. Nomura, D. K. *et al.* Monoacylglycerol Lipase Regulates a Fatty Acid Network that Promotes Cancer Pathogenesis. *Cell* **140**, 49–61 (2010).

19. Lopes-Coelho, F., Gouveia-Fernandes, S. & Serpa, J. Metabolic cooperation between cancer and non-cancerous stromal cells is pivotal in cancer progression. *Tumor Biology* **40**, 1–15 (2018).

20. Corn, K. C., Windham, M. A. & Rafat, M. Lipids in the Tumor Microenvironment: From Cancer Progression to Treatment. *Prog Lipid Res* **80**, 101055 (2020).

21. Zhao, H. *et al.* Tumor microenvironment derived exosomes pleiotropically modulate cancer cell metabolism. *Elife* **5**, (2016).

22. Ruan, C., Meng, Y. & Song, H. CD36: an emerging therapeutic target for cancer and its molecular mechanisms. *J Cancer Res Clin Oncol* **148**, 1551–1558 (2022).

23. Watt, M. J. *et al. Suppressing fatty acid uptake has therapeutic effects in preclinical models of prostate cancer*. *Sci. Transl. Med* vol. 11 http://stm.sciencemag.org/ (2019).

24. Pascual, G. *et al.* Targeting metastasis-initiating cells through the fatty acid receptor CD36. *Nature 2016 541:7635* **541**, 41–45 (2016).

25. Ladanyi, A. *et al.* Adipocyte-induced CD36 expression drives ovarian cancer progression and metastasis. *Oncogene 2018 37:17* **37**, 2285–2301 (2018).

26. Pan, J. *et al.* CD36 mediates palmitate acid-induced metastasis of gastric cancer via AKT/GSK-3β/β-catenin pathway. *Journal of Experimental and Clinical Cancer Research* **38**, 1–15 (2019).

27. Drury, J. *et al.* Upregulation of CD36, a Fatty Acid Translocase, Promotes Colorectal Cancer Metastasis by Increasing MMP28 and Decreasing E-Cadherin Expression. (2022) doi:10.3390/cancers14010252.

28. Ruan, C., Meng, Y. & Song, H. CD36: an emerging therapeutic target for cancer and its molecular mechanisms. *J Cancer Res Clin Oncol* **148**, 1551–1558 (2022).

29. Forootan, F. S. *et al. Fatty acid activated PPARg promotes tumorigenicity of prostate cancer cells by up regulating VEGF via PPAR responsive elements of the promoter*. vol. 7 www.impactjournals.com/oncotarget.

30. Zhang, M. *et al.* Adipocyte-derived lipids mediate melanoma progression via FATP proteins. *Cancer Discov* **8**, 1006–1025 (2018).

31. Veglia, F. *et al.* Fatty acid transport protein 2 reprograms neutrophils in cancer. *Nature 2019 569:7754* **569**, 73–78 (2019).

32. Bensaad, K. *et al.* Fatty acid uptake and lipid storage induced by HIF-1α contribute to cell growth and survival after hypoxia-reoxygenation. *Cell Rep* **9**, 349–365 (2014).

33. Tan, Y. *et al.* Metabolic reprogramming from glycolysis to fatty acid uptake and beta-oxidation in platinum-resistant cancer cells. *Nature Communications 2022 13:1* **13**, 1–16 (2022).

34. Geng, F. *et al.* Inhibition of SOAT1 suppresses glioblastoma growth via blocking SREBP-1-mediated lipogenesis. *Clinical Cancer Research* **22**, 5337–5348 (2016).

35. Yue, S. *et al.* Cholesteryl ester accumulation induced by PTEN loss and PI3K/AKT activation underlies human prostate cancer aggressiveness. *Cell Metab* **19**, 393–406 (2014).

36. Menendez, J. A. & Lupu, R. Fatty acid synthase and the lipogenic phenotype in cancer pathogenesis. *Nature Reviews Cancer* vol. 7 763–777 Preprint at https://doi.org/10.1038/nrc2222 (2007).

37. Röhrig, F. & Schulze, A. The multifaceted roles of fatty acid synthesis in cancer. *Nature Reviews Cancer* vol. 16 732–749 Preprint at https://doi.org/10.1038/nrc.2016.89 (2016).

38. Bauer, D. E., Hatzivassiliou, G., Zhao, F., Andreadis, C. & Thompson, C. B. ATP citrate lyase is an important component of cell growth and transformation. *Oncogene* **24**, 6314–6322 (2005).

39. Hatzivassiliou, G. *et al.* ATP citrate lyase inhibition can suppress tumor cell growth. *Cancer Cell* **8**, 311–321 (2005).

40. Granchi, C. ATP citrate lyase (ACLY) inhibitors: An anti-cancer strategy at the crossroads of glucose and lipid metabolism. *European Journal of Medicinal Chemistry* vol. 157 1276–1291 Preprint at https://doi.org/10.1016/j.ejmech.2018.09.001 (2018).

41. Migita, T. *et al.* ATP Citrate Lyase: Activation and Therapeutic Implications in Non–Small Cell Lung Cancer. *Cancer Res* **68**, 8547–8554 (2008).

42. Chajès, V., Cambot, M., Moreau, K., Lenoir, G. M. & Joulin, V. Acetyl-CoA carboxylase α is essential to breast cancer cell survival. *Cancer Res* **66**, 5287–5294 (2006).

43. Brusselmans, K., de Schrijver, E., Verhoeven, G. & Swinnen, J. v. *RNA Interference-Mediated Silencing of the Acetyl-CoA-Carboxylase-a Gene Induces Growth Inhibition and Apoptosis of Prostate Cancer Cells*. http://aacrjournals.org/cancerres/article-pdf/65/15/6719/2533896/6719-6725.pdf.

44. Wang, C. *et al.* Acetyl-CoA carboxylase-α inhibitor TOFA induces human cancer cell apoptosis. *Biochem Biophys Res Commun* **385**, 302–306 (2009).

45. Granchi, C. ATP citrate lyase (ACLY) inhibitors: An anti-cancer strategy at the crossroads of glucose and lipid metabolism. *Eur J Med Chem* **157**, 1276–1291 (2018).

46. Zhao, S. *et al.* ATP-Citrate Lyase Controls a Glucose-to-Acetate Metabolic Switch. *Cell Rep* **17**, 1037–1052 (2016).

47. Mews, P. *et al.* Acetyl-CoA synthetase regulates histone acetylation and hippocampal memory. *Nature 2017 546:7658* **546**, 381–386 (2017).

48. Wellen, K. E. *et al.* ATP-citrate lyase links cellular metabolism to histone acetylation. *Science (1979)* **324**, 1076–1080 (2009).

49. Lally, J. S. V. *et al.* Inhibition of Acetyl-CoA Carboxylase by Phosphorylation or the Inhibitor ND-654 Suppresses Lipogenesis and Hepatocellular Carcinoma. *Cell Metab* **29**, 174-182.e5 (2019).

50. Svensson, R. U. *et al.* Inhibition of acetyl-CoA carboxylase suppresses fatty acid synthesis and tumor growth of non-small-cell lung cancer in preclinical models. *Nat Med* **22**, 1108–1119 (2016).

51. Alo, P. L. *et al.* Expression of Fatty Acid Synthase (FAS) as a Predictor of Recurrence in Stage I Breast Carcinoma Patients.

52. Fiorentino, M. *et al.* Overexpression of fatty acid synthase is associated with palmitoylation of Wnt1 and cytoplasmic stabilization of b-catenin in prostate cancer. *Laboratory Investigation* **88**, 1340–1348 (2008).

53. Wu, X. *et al.* FASN regulates cellular response to genotoxic treatments by increasing PARP-1 expression and DNA repair activity via NF-κB and SP1. *Proc Natl Acad Sci U S A* **113**, E6965–E6973 (2016).

54. Buckley, D. *et al.* Fatty acid synthase – Modern tumor cell biology insights into a classical oncology target. *Pharmacol Ther* **177**, 23–31 (2017).

55. Zaytseva, Y. Y. *et al.* Preclinical evaluation of novel fatty acid synthase inhibitors in primary colorectal cancer cells and a patient-derived xenograft model of colorectal cancer. *Oncotarget* **9**, 24787–24800 (2018).

56. Brenner, A. J. *et al.* First-in-human investigation of the oral first-in-class fatty acid synthase (FASN) inhibitor, TVB-2640. *https://doi.org/10.1200/jco.2015.33.15_suppl.tps2615* **33**, TPS2615–TPS2615 (2015).

57. Drury, J. *et al.* Inhibition of Fatty Acid Synthase Upregulates Expression of CD36 to Sustain Proliferation of Colorectal Cancer Cells. *Front Oncol* **10**, 1185 (2020).

58. Jiang, L. *et al.* Metabolic reprogramming during TGFβ1-induced epithelial-to-mesenchymal transition. *Oncogene* **34**, 3908–3916 (2015).

59. Czumaj, A., Tomasz´, T. & Nski, T. Biological Role of Unsaturated Fatty Acid Desaturases in Health and Disease. doi:10.3390/nu12020356.

60. Vriens, K. *et al.* Evidence for an alternative fatty acid desaturation pathway increasing cancer plasticity. *Nature 2019 566:7744* **566**, 403–406 (2019).

61. Kubota, C. S. & Espenshade, P. J. Targeting Stearoyl-CoA Desaturase in Solid Tumors. *Cancer Research* vol. 82 1682–1688 Preprint at https://doi.org/10.1158/0008-5472.CAN-21-4044 (2022).

62. von Roemeling, C. A. *et al.* Stearoyl-CoA Desaturase 1 Is a Novel Molecular Therapeutic Target for Clear Cell Renal Cell Carcinoma. doi:10.1158/1078-0432.CCR-12-3249.

63. Mason, P. *et al.* SCD1 inhibition causes cancer cell death by depleting mono-unsaturated fatty acids. *PLoS One* **7**, (2012).

64. Li, W. *et al. Targeting stearoyl-CoA desaturase 1 to repress endometrial cancer progression*. *Oncotarget* vol. 9 www.impactjournals.com/oncotarget (2018).

65. Fritz, V. *et al.* Abrogation of De novo lipogenesis by stearoyl-CoA desaturase 1 inhibition interferes with oncogenic signaling and blocks prostate cancer progression in mice. *Mol Cancer Ther* **9**, 1740–1754 (2010).

66. Pinkham, K. *et al.* Stearoyl CoA Desaturase Is Essential for Regulation of Endoplasmic Reticulum Homeostasis and Tumor Growth in Glioblastoma Cancer Stem Cells. *Stem Cell Reports* **12**, 712–727 (2019).

67. Oatman, N. *et al. H E A L T H A N D M E D I C I N E Mechanisms of stearoyl CoA desaturase inhibitor sensitivity and acquired resistance in cancer*. *Sci. Adv* vol. 7 http://advances.sciencemag.org/ (2021).

68. Ariyama, H., Kono, N., Matsuda, S., Inoue, T. & Arai, H. Decrease in membrane phospholipid unsaturation induces unfolded protein response. *Journal of Biological Chemistry* **285**, 22027–22035 (2010).

69. Scaglia, N. & Igal, R. A. Stearoyl-CoA desaturase is involved in the control of proliferation, anchorage-independent growth, and survival in human transformed cells. *Journal of Biological Chemistry* **280**, 25339–25349 (2005).

70. Peck, B. *et al.* Inhibition of fatty acid desaturation is detrimental to cancer cell survival in metabolically compromised environments. *Cancer Metab* **4**, (2016).

71. Peck, B. *et al.* Inhibition of fatty acid desaturation is detrimental to cancer cell survival in metabolically compromised environments. *Cancer Metab* **4**, (2016).

72. Nashed, M., Chisholm, J. W. & Ariel Igal, R. Stearoyl-CoA desaturase activity modulates the activation of epidermal growth factor receptor in human lung cancer cells. *https://doi.org/10.1258/ebm.2012.012126* **237**, 1007–1017 (2012).

73. Xu, C. *et al.* ARTICLE Lipidomics reveals that sustained SREBP-1-dependent lipogenesis is a key mediator of gefitinib-acquired resistance in EGFR-mutant lung cancer. doi:10.1038/s41420-021-00744-1.

74. Igal, R. A. Stearoyl CoA desaturase-1: New insights into a central regulator of cancer metabolism. *Biochimica et Biophysica Acta - Molecular and Cell Biology of Lipids* vol. 1861 1865–1880 Preprint at https://doi.org/10.1016/j.bbalip.2016.09.009 (2016).

75. Fritz, V. *et al.* Abrogation of De novo Lipogenesis by Stearoyl-CoA Desaturase 1 Inhibition Interferes with Oncogenic Signaling and Blocks Prostate Cancer Progression in Mice. doi:10.1158/1535-7163.MCT-09-1064.

76. Hess, D., Chisholm, J. W. & Igal, R. A. Inhibition of StearoylCoA Desaturase Activity Blocks Cell Cycle Progression and Induces Programmed Cell Death in Lung Cancer Cells. *PLoS One* **5**, 11394 (2010).

77. Rios-Esteves, J. & Resh, M. D. Stearoyl CoA Desaturase Is Required to Produce Active, Lipid-Modified Wnt Proteins. *Cell Rep* **4**, 1072–1081 (2013).

78. Lai, K. K. Y. *et al.* Stearoyl-CoA Desaturase Promotes Liver Fibrosis and Tumor Development in Mice via a Wnt Positive-Signaling Loop by Stabilization of Low-Density Lipoprotein-Receptor-Related Proteins 5 and 6. *Gastroenterology* **152**, 1477–1491 (2017).

79. Gao, Y. *et al.* Stearoyl-CoA-desaturase-1 regulates gastric cancer stem-like properties and promotes tumour metastasis via Hippo/YAP pathway. *Br J Cancer* **122**, 1837–1847 (2020).

80. Ma, X. L. *et al.* Sphere-forming culture enriches liver cancer stem cells and reveals Stearoyl-CoA desaturase 1 as a potential therapeutic target. *BMC Cancer* **19**, (2019).

81. Noto, A. *et al.* Stearoyl-CoA-desaturase 1 regulates lung cancer stemness via stabilization and nuclear localization of YAP/TAZ. *Oncogene* **36**, 4573–4584 (2017).

82. Pisanu, M. E. *et al.* Inhibition of Stearoyl-CoA desaturase 1 reverts BRAF and MEK inhibition-induced selection of cancer stem cells in BRAF-mutated melanoma. *Journal of Experimental and Clinical Cancer Research* **37**, (2018).

83. Yi, M. *et al.* Emerging role of lipid metabolism alterations in Cancer stem cells. doi:10.1186/s13046-018-0784-5.

84. aging-v12i15-103598.

85. Noto, A. *et al.* Stearoyl-CoA desaturase-1 is a key factor for lung cancer-initiating cells. *Cell Death Dis* **4**, (2013).

86. Li, J. *et al.* Lipid Desaturation Is a Metabolic Marker and Therapeutic Target of Ovarian Cancer Stem Cells. *Cell Stem Cell* **20**, 303-314.e5 (2017).

87. Teng, J. *et al.* Dissecting inherent intratumor heterogeneity in patient-derived glioblastoma culture models. *Neuro Oncol* **19**, 820–832 (2017).

88. Ran, H. *et al.* Stearoyl-CoA desaturase-1 promotes colorectal cancer metastasis in response to glucose by suppressing PTEN. *Journal of Experimental and Clinical Cancer Research* **37**, (2018).

89. Liu, G. *et al.* Lung fibroblasts promote metastatic colonization through upregulation of stearoyl-CoA desaturase 1 in tumor cells. *Oncogene* doi:10.1038/s41388-017-0062-6.

90. Liu, G. *et al.* Lung fibroblasts promote metastatic colonization through upregulation of stearoyl-CoA desaturase 1 in tumor cells. doi:10.1038/s41388-017-0062-6.

91. Vivas-García, Y. *et al.* Lineage-Restricted Regulation of SCD and Fatty Acid Saturation by MITF Controls Melanoma Phenotypic Plasticity. *Mol Cell* **77**, 120-137.e9 (2020).

92. Tracz-Gaszewska, Z. & Dobrzyn, P. Stearoyl-CoA Desaturase 1 as a Therapeutic Target for the Treatment of Cancer. *Cancers (Basel)* **11**, (2019).

93. SearchResults.

94. Williams, N. S. *et al.* Tumor-Activated Benzothiazole Inhibitors of Stearoyl-CoA Desaturase. *J Med Chem* **63**, 9773–9786 (2020).

95. Smith, K. R. & Thiboutot, D. M. Thematic review series: Skin Lipids. Sebaceous gland lipids: friend or foe? *J Lipid Res* **49**, 271–281 (2008).

96. Peck, B. & Schulze, A. Lipid desaturation – the next step in targeting lipogenesis in cancer? *FEBS J* **283**, 2767–2778 (2016).

97. Hansen-Petrik, M. B. *et al.* Selective inhibition of Δ-6 desaturase impedes intestinal tumorigenesis. *Cancer Lett* **175**, 157–163 (2002).

98. Qu, C., Wan, X., Rong, J. & Huang, R. Inhibiting Delta-6 Desaturase Activity Suppresses Tumor Growth in Mice. *PLoS One* **7**, 47567 (2012).

99. Gimple, R. C. *et al.* Glioma stem cell–specific superenhancer promotes polyunsaturated fatty-acid synthesis to support EGFR signaling. *Cancer Discov* **9**, 1248–1267 (2019).

100. Wang, J. *et al.* Cancer Management and Research Dovepress Delta-6-desaturase inhibitor enhances radiation therapy in glioblastoma in vitro and in vivo. *Cancer Manag Res* 10–6779 (2018) doi:10.2147/CMAR.S185601.

101. Lee, H. J. *et al.* FADS2-mediated fatty acid desaturation and cholesterol esterification are signatures of metabolic reprogramming during 2 melanoma progression. doi:10.1101/2020.07.12.198903.

102. Kalinski, P. Regulation of Immune Responses by Prostaglandin E2. *The Journal of Immunology* **188**, 21–28 (2012).

103. Pan, Y. *et al.* Deletion of cyclooxygenase-2 inhibits K-ras–induced lung carcinogenesis. *Oncotarget* **6**, 38816 (2015).

104. Howe, L. R. *et al.* HER2/neu-Induced Mammary Tumorigenesis and Angiogenesis Are Reduced in Cyclooxygenase-2 Knockout Mice. *Cancer Res* **65**, 10113–10119 (2005).

105. Sonoshita, M. *et al. Arachidonic acid is metabolized to prostaglandin H 2 (PGH 2) by cyclooxygenase (COX) Acceleration of intestinal polyposis through prostaglandin receptor EP2 in Apc Δ716 knockout mice*. *NATURE MEDICINE • VOLUME* vol. 7 http://medicine.nature.com (2001).

106. Castellone, M. D., Teramoto, H., Williams, B. O., Druey, K. M. & Gutkind, J. S. Medicine: Prostaglandin E2 promotes colon cancer cell growth through a Gs-axin-β-catenin signaling axis. *Science (1979)* **310**, 1504–1510 (2005).

107. Wang, D., Buchanan, F. G., Wang, H., Dey, S. K. & Dubois, R. N. *Prostaglandin E 2 Enhances Intestinal Adenoma Growth via Activation of the Ras-Mitogen-Activated Protein Kinase Cascade*. http://aacrjournals.org/cancerres/article-pdf/65/5/1822/2541234/1822-1829.pdf.

108. Han, J. & Kaufman, R. J. The role of ER stress in lipid metabolism and lipotoxicity. *J Lipid Res* **57**, 1329–1338 (2016).

109. Schaffer, J. E. Lipotoxicity: Many Roads to Cell Dysfunction and Cell Death: Introduction to a Thematic Review Series. (2016) doi:10.1194/jlr.E069880.

110. Wei, Y., Wang, D., Topczewski, F. & Pagliassotti, M. J. Saturated fatty acids induce endoplasmic reticulum stress and apoptosis independently of ceramide in liver cells. *Am J Physiol Endocrinol Metab* **291**, (2006).

111. Pineau, L. *et al.* Lipid-induced ER stress: synergistic effects of sterols and saturated fatty acids. *Traffic* **10**, 673–690 (2009).

112. Piccolis, M. *et al.* Probing the Global Cellular Responses to Lipotoxicity Caused by Saturated Fatty Acids. *Mol Cell* **74**, 32-44.e8 (2019).

113. Rudalska, R. *et al.* LXRα activation and Raf inhibition trigger lethal lipotoxicity in liver cancer. *Nat Cancer* **2**, 201–217 (2021).

114. Schultz, J. R. *et al.* Role of LXRs in control of lipogenesis. *Genes Dev* **14**, 2831–2838 (2000).

115. Lien, E. C. *et al.* Low glycaemic diets alter lipid metabolism to influence tumour growth. *Nature* **599**, 302–307 (2021).

116. Cheng, X. *et al.* Targeting DGAT1 Ameliorates Glioblastoma by Increasing Fat Catabolism and Oxidative Stress. *Cell Metab* **32**, 229-242.e8 (2020).

117. Yuan, Y., Shah, N., Almohaisin, M. I., Saha, S. & Lu, F. Assessing fatty acid-induced lipotoxicity and its therapeutic potential in glioblastoma using stimulated Raman microscopy. *Scientific Reports* | **11**, 7422 (123AD).

118. Cheng, X., Geng, F. & Guo, D. DGAT1 protects tumor from lipotoxicity, emerging as a promising metabolic target for cancer therapy. *Mol Cell Oncol* **7**, (2020).

119. Wang, W. *et al.* CD8+ T cells regulate tumour ferroptosis during cancer immunotherapy. *Nature* **569**, 270–274 (2019).

120. Kagan, V. E. *et al.* Oxidized arachidonic and adrenic PEs navigate cells to ferroptosis. *Nat Chem Biol* **13**, 81–90 (2017).

121. Stockwell, B. R. *et al.* Ferroptosis: A Regulated Cell Death Nexus Linking Metabolism, Redox Biology, and Disease. *Cell* vol. 171 273–285 Preprint at https://doi.org/10.1016/j.cell.2017.09.021 (2017).

122. Dolma, S., Lessnick, S. L., Hahn, W. C. & Stockwell, B. R. Identification of genotype-selective antitumor agents using synthetic lethal chemical screening in engineered human tumor cells. *Cancer Cell* **3**, 285–296 (2003).

123. Magtanong, L. *et al.* Exogenous Monounsaturated Fatty Acids Promote a Ferroptosis-Resistant Cell State. *Cell Chem Biol* **26**, 420-432.e9 (2019).

124. Tesfay, L. *et al.* Stearoyl-CoA desaturase 1 protects ovarian cancer cells from ferroptotic cell death. *Cancer Res* **79**, 5355–5366 (2019).

125. Yi, J., Zhu, J., Wu, J., Thompson, C. B. & Jiang, X. Oncogenic activation of PI3K-AKT-mTOR signaling suppresses ferroptosis via SREBP-mediated lipogenesis. doi:10.1073/pnas.2017152117/-/DCSupplemental.

126. Jiang, Y. *et al.* EGLN1/c-Myc induced lymphoid-specific helicase inhibits ferroptosis through lipid metabolic gene expression changes. *Theranostics* **7**, 3293–3305 (2017).

127. Xuan, Y. *et al.* SCD1/FADS2 fatty acid desaturases equipoise lipid metabolic activity and redox-driven ferroptosis in ascites-derived ovarian cancer cells. *Theranostics* **12**, 3534–3552 (2022).

128. Triki, M. *et al.* mTOR Signaling and SREBP Activity Increase FADS2 Expression and Can Activate Sapienate Biosynthesis. *Cell Rep* **31**, (2020).

129. Dierge, E. *et al.* Peroxidation of n-3 and n-6 polyunsaturated fatty acids in the acidic tumor environment leads to ferroptosis-mediated anticancer effects. *Cell Metab* **33**, 1701-1715.e5 (2021).

130. Manzo, T. *et al.* Accumulation of long-chain fatty acids in the tumor microenvironment drives dysfunction in intrapancreatic cd8+ t cells. *Journal of Experimental Medicine* **217**, (2020).

131. Xu, S. *et al.* Uptake of oxidized lipids by the scavenger receptor CD36 promotes lipid peroxidation and dysfunction in CD8+ T cells in tumors. *Immunity* **54**, 1561-1577.e7 (2021).

132. Ma, X. *et al.* CD36-mediated ferroptosis dampens intratumoral CD8+ T cell effector function and impairs their antitumor ability. *Cell Metab* **33**, 1001-1012.e5 (2021).

133. Burnet, N. G., Jefferies, S. J., Benson, R. J., Hunt, D. P. & Treasure, F. P. Years of life lost (YLL) from cancer is an important measure of population burden--and should be considered when allocating research funds. *Br J Cancer* **92**, 241–245 (2005).

134. Stupp, R. *et al. Radiotherapy plus Concomitant and Adjuvant Temozolomide for Glioblastoma*. www.nejm.org.

135. Campos, B., Olsen, L. R., Urup, T. & Poulsen, H. S. A comprehensive profile of recurrent glioblastoma. *Oncogene* vol. 35 5819–5825 Preprint at https://doi.org/10.1038/onc.2016.85 (2016).

136. Kim, J. *et al.* Spatiotemporal Evolution of the Primary Glioblastoma Genome. *Cancer Cell* **28**, 318–328 (2015).

137. Andor, N., Harness, J. v., Müller, S., Mewes, H. W. & Petritsch, C. EXPANDS: expanding ploidy and allele frequency on nested subpopulations. *Bioinformatics* **30**, 50–60 (2013).

138. Wang, J. *et al.* Clonal evolution of glioblastoma under therapy. (2016) doi:10.1038/ng.3590.

139. Johnson, B. E. *et al.* Mutational analysis reveals the origin and therapy-driven evolution of recurrent glioma. *Science (1979)* **343**, 189–193 (2014).

140. Molinaro, A. M., Taylor, J. W., Wiencke, J. K. & Wrensch, M. R. Genetic and molecular epidemiology of adult diffuse glioma. *Nature Reviews Neurology* vol. 15 405–417 Preprint at https://doi.org/10.1038/s41582-019-0220-2 (2019).

141. Komori, T. Grading of adult diffuse gliomas according to the 2021 WHO Classification of Tumors of the Central Nervous System. doi:10.1038/s41374-021-00667-6.

142. Cohen, A. L., Holmen, S. L. & Colman, H. NEURO-ONCOLOGY (LE ABREY, SECTION EDITOR) IDH1 and IDH2 Mutations in Gliomas. doi:10.1007/s11910-013-0345-4.

143. Wiestler, B. *et al.* Integrated DNA methylation and copy-number profiling identify three clinically and biologically relevant groups of anaplastic glioma. *Acta Neuropathol* **3**, 561–571 (2014).

144. Ceccarelli, M. *et al.* Molecular Profiling Reveals Biologically Discrete Subsets and Pathways of Progression in Diffuse Glioma. *Cell* **164**, 550–563 (2016).

145. Hovestadt, V. *et al.* Robust molecular subgrouping and copy-number profiling of medulloblastoma from small amounts of archival tumour material using high-density DNA methylation arrays. *Acta Neuropathol* **3**, 913–916 (2013).

146. Gerson, S. L. MGMT: its role in cancer aetiology and cancer therapeutics. *Nature Reviews Cancer 2004 4:4* **4**, 296–307 (2004).

147. Malmström, A. *et al.* Temozolomide versus standard 6-week radiotherapy versus hypofractionated radiotherapy in patients older than 60 years with glioblastoma: The Nordic randomised, phase 3 trial. *Lancet Oncol* **13**, 916–926 (2012).

148. Gilbert, M. R. *et al.* Dose-dense temozolomide for newly diagnosed glioblastoma: A randomized phase III clinical trial. *Journal of Clinical Oncology* **31**, 4085–4091 (2013).

149. Weller, M. *et al.* Molecular predictors of progression-free and overall survival in patients with newly diagnosed glioblastoma: A prospective translational study of the German Glioma Network. *Journal of Clinical Oncology* **27**, 5743–5750 (2009).

150. Hegi, M. E. *et al.* MGMT Gene Silencing and Benefit from Temozolomide in Glioblastoma . *New England Journal of Medicine* **352**, 997–1003 (2005).

151. Wick, W. *et al.* Temozolomide chemotherapy alone versus radiotherapy alone for malignant astrocytoma in the elderly: The NOA-08 randomised, phase 3 trial. *Lancet Oncol* **13**, 707–715 (2012).

152. Perry, J. R. *et al.* Short-Course Radiation plus Temozolomide in Elderly Patients with Glioblastoma. *New England Journal of Medicine* **376**, 1027–1037 (2017).

153. Oronsky, B., Reid, T. R., Oronsky, A., Sandhu, N. & Knox, S. J. A Review of Newly Diagnosed Glioblastoma. *Frontiers in Oncology* vol. 10 Preprint at https://doi.org/10.3389/fonc.2020.574012 (2021).

154. Aum, D. J. *et al.* Molecular and cellular heterogeneity: The hallmark of glioblastoma. *Neurosurg Focus* **37**, (2014).

155. Qazi, M. A. *et al.* Intratumoral heterogeneity: pathways to treatment resistance and relapse in human glioblastoma. *Annals of Oncology* **28**, 1448–1456 (2017).

156. Phillips, H. S. *et al.* Molecular subclasses of high-grade glioma predict prognosis, delineate a pattern of disease progression, and resemble stages in neurogenesis. *Cancer Cell* **9**, 157–173 (2006).

157. Verhaak, R. G. W. *et al.* Integrated Genomic Analysis Identifies Clinically Relevant Subtypes of Glioblastoma Characterized by Abnormalities in PDGFRA, IDH1, EGFR, and NF1. *Cancer Cell* **17**, 98–110 (2010).

158. Parker, N. R., Khong, P., Parkinson, J. F., Howell, V. M. & Wheeler, H. R. Molecular heterogeneity in glioblastoma: Potential clinical implications. *Front Oncol* **5**, (2015).

159. Brennan, C. W. *et al.* The somatic genomic landscape of glioblastoma. *Cell* **155**, 462 (2013).

160. Weller, M. *et al.* Rindopepimut with temozolomide for patients with newly diagnosed, EGFRvIII-expressing glioblastoma (ACT IV): a randomised, double-blind, international phase 3 trial. *Lancet Oncol* **18**, 1373–1385 (2017).

161. Snuderl, M. *et al.* Mosaic amplification of multiple receptor tyrosine kinase genes in glioblastoma. *Cancer Cell* **20**, 810–817 (2011).

162. Szerlip, N. J. *et al.* Intratumoral heterogeneity of receptor tyrosine kinases EGFR and PDGFRA amplification in glioblastoma defines subpopulations with distinct growth factor response. doi:10.1073/pnas.1114033109.

163. Little, S. E. *et al.* Receptor tyrosine kinase genes amplified in glioblastoma exhibit a mutual exclusivity in variable proportions reflective of individual tumor heterogeneity. *Cancer Res* **72**, 1614–1620 (2012).

164. Patel, A. P. *et al.* Single-cell RNA-seq highlights intratumoral heterogeneity in primary glioblastoma. *Science (1979)* **344**, 1396–1401 (2014).

165. Bergmann, N. *et al.* The Intratumoral Heterogeneity Reflects the Intertumoral Subtypes of Glioblastoma Multiforme: A Regional Immunohistochemistry Analysis. *Front Oncol* **10**, (2020).

166. Sottoriva, A. *et al.* Intratumor heterogeneity in human glioblastoma reflects cancer evolutionary dynamics. *Proc Natl Acad Sci U S A* **110**, 4009–4014 (2013).

167. Meyer, M. *et al.* Single cell-derived clonal analysis of human glioblastoma links functional and genomic heterogeneity. *Proc Natl Acad Sci U S A* **112**, 851–856 (2015).

168. Wang, J. *et al.* Clonal evolution of glioblastoma under therapy. *Nature Genetics 2016 48:7* **48**, 768–776 (2016).

169. Wenger, A. *et al.* Neuro-Oncology Intratumor DNA methylation heterogeneity in glioblastoma: implications for DNA methylation-based classification. doi:10.1093/neuonc/noz011.

170. Paulson, J. A. *et al.* Epigenetic encoding, heritability and plasticity of glioma transcriptional cell states. doi:10.1038/s41588-021-00927-7.

171. (No Title). (2004) doi:10.1038/nature03031.

172. Prager, B. C., Bhargava, S., Mahadev, V., Hubert, C. G. & Rich, J. N. Glioblastoma Stem Cells: Driving Resilience through Chaos. *Trends in Cancer* vol. 6 223–235 Preprint at https://doi.org/10.1016/j.trecan.2020.01.009 (2020).

173. Chen, J. *et al.* A restricted cell population propagates glioblastoma growth after chemotherapy. *Nature 2012 488:7412* **488**, 522–526 (2012).

174. Bao, S. *et al.* Glioma stem cells promote radioresistance by preferential activation of the DNA damage response. *Nature 2006 444:7120* **444**, 756–760 (2006).

175. Liu, G. *et al.* Analysis of gene expression and chemoresistance of CD133+ cancer stem cells in glioblastoma. *Mol Cancer* **5**, 1–12 (2006).

176. Cheng, L. *et al.* Elevated invasive potential of glioblastoma stem cells. *Biochem Biophys Res Commun* **406**, 643–648 (2011).

177. Wang, X. *et al.* ADAM17 promotes U87 glioblastoma stem cell migration and invasion. *Brain Res* **1538**, 151–158 (2013).

178. Chemotherapy resistance of glioblastoma stem cells. (2006) doi:10.1038/sj.cdd.4401872.

179. Binda, E. *et al.* Wnt5a drives an invasive phenotype in human glioblastoma stem-like cells. *Cancer Res* **77**, 996–1007 (2017).

180. Zeppernick, F. *et al.* Stem Cell Marker CD133 Affects Clinical Outcome in Glioma Patients. doi:10.1158/1078-0432.CCR-07-0932.

181. Pallini, R. *et al.* Cancer Stem Cell Analysis and Clinical Outcome in Patients with Glioblastoma Multiforme. doi:10.1158/1078-0432.CCR-08-0644.

182. Chen, J. *et al.* A restricted cell population propagates glioblastoma growth after chemotherapy. (2012) doi:10.1038/nature11287.

183. Chen, R. *et al.* A Hierarchy of Self-Renewing Tumor-Initiating Cell Types in Glioblastoma. *Cancer Cell* **17**, 362–375 (2010).

184. Wang, J. *et al.* CD133 negative glioma cells form tumors in nude rats and give rise to CD133 positive cells. doi:10.1002/ijc.23130.

185. Nathanson, D. A. *et al.* Targeted therapy resistance mediated by dynamic regulation of extrachromosomal mutant EGFR DNA. *Science (1979)* **343**, 72–76 (2014).

186. Auffinger, B. *et al.* Conversion of differentiated cancer cells into cancer stem-like cells in a glioblastoma model after primary chemotherapy. *Cell Death Differ* **21**, 1119–1131 (2014).

187. Dahan, P. *et al.* Ionizing radiations sustain glioblastoma cell dedifferentiation to a stem-like phenotype through survivin: possible involvement in radioresistance. *Cell Death & Disease 2014 5:11* **5**, e1543–e1543 (2014).

188. Dirkse, A. *et al.* Stem cell-associated heterogeneity in Glioblastoma results from intrinsic tumor plasticity shaped by the microenvironment. doi:10.1038/s41467-019-09853-z.

189. Wang, L. *et al.* The phenotypes of proliferating glioblastoma cells reside on a single axis of variation. *Cancer Discov* **9**, 1708–1719 (2019).

190. Castellan, M. *et al.* Single-cell analyses reveal YAP/TAZ as regulators of stemness and cell plasticity in glioblastoma. doi:10.1038/s43018-020-00150-z.

191. Wolf, A. *et al.* Hexokinase 2 is a key mediator of aerobic glycolysis and promotes tumor growth in human glioblastoma multiforme. *Journal of Experimental Medicine* **208**, 313–326 (2011).

192. Maher, E. A. *et al.* Metabolism of [U-13C]glucose in human brain tumors in vivo. *NMR Biomed* **25**, 1234–1244 (2012).

193. Mashimo, T. *et al.* Acetate is a bioenergetic substrate for human glioblastoma and brain metastases. *Cell* **159**, 1603–1614 (2014).

194. Ebrahimi, M. *et al.* Astrocyte-expressed FABP7 regulates dendritic morphology and excitatory synaptic function of cortical neurons. *Glia* **64**, 48–62 (2016).

195. Tao, B. B. *et al.* Up-regulation of USP2a and FASN in gliomas correlates strongly with glioma grade. *J Clin Neurosci* **20**, 717–720 (2013).

196. Grube, S. *et al.* Overexpression of fatty acid synthase in human gliomas correlates with the WHO tumor grade and inhibition with Orlistat reduces cell viability and triggers apoptosis. *J Neurooncol* **118**, 277–287 (2014).

197. Guo, D. *et al.* EGFR signaling through an Akt-SREBP-1-dependent, rapamycin-resistant pathway sensitizes glioblastomas to antilipogenic therapy. *Sci Signal* **2**, (2009).

198. Guo, D. *et al.* The AMPK agonist AICAR inhibits the growth of EGFRvIII-expressing glioblastomas by inhibiting lipogenesis. *Proc Natl Acad Sci U S A* **106**, 12932–12937 (2009).

199. Jones, J. E. C. *et al.* Inhibition of Acetyl-CoA Carboxylase 1 (ACC1) and 2 (ACC2) Reduces Proliferation and De Novo Lipogenesis of EGFRvIII Human Glioblastoma Cells. *PLoS One* **12**, (2017).

200. Yasumoto, Y. *et al.* Inhibition of Fatty Acid Synthase Decreases Expression of Stemness Markers in Glioma Stem Cells. *PLoS One* **11**, (2016).

201. Cheng, C. *et al.* Glucose-Mediated N-glycosylation of SCAP Is Essential for SREBP-1 Activation and Tumor Growth. *Cancer Cell* **28**, 569–581 (2015).

202. Ru, P. *et al.* Feedback Loop Regulation of SCAP/SREBP-1 by miR-29 Modulates EGFR Signaling-Driven Glioblastoma Growth. *Cell Rep* **16**, 1527–1535 (2016).

203. Infiltrative and drug-resistant slow-cycling cells support metabolic heterogeneity in glioblastoma. https://www.embopress.org/doi/epdf/10.15252/embj.201798772?src=getftr.

204. de Rosa, A. *et al.* A Radial Glia Gene Marker, Fatty Acid Binding Protein 7 (FABP7), Is Involved in Proliferation and Invasion of Glioblastoma Cells. *PLoS One* **7**, (2012).

205. Choi, W. S. *et al.* Fabp7 facilitates uptake of docosahexaenoic acid in glioblastoma neural stem-like cells. *Nutrients* **13**, (2021).

206. Villa, G. R. *et al.* An LXR-Cholesterol Axis Creates a Metabolic Co-Dependency for Brain Cancers. *Cancer Cell* **30**, 683–693 (2016).

207. Guo, D. *et al.* An LXR agonist promotes glioblastoma cell death through inhibition of an EGFR/AKT/ SREBP-1/LDLR-dependent pathway. *Cancer Discov* **1**, 442–456 (2011).

208. Zhang, J. & Liu, Q. Cholesterol metabolism and homeostasis in the brain. *Protein Cell* **6**, 254 (2015).

209. Fang, R. *et al.* EGFR/SRC/ERK-stabilized YTHDF2 promotes cholesterol dysregulation and invasive growth of glioblastoma. *Nat Commun* **12**, (2021).

210. McBrayer, S. K. *et al.* Transaminase Inhibition by 2-Hydroxyglutarate Impairs Glutamate Biosynthesis and Redox Homeostasis in Glioma. *Cell* **175**, 101-116.e25 (2018).

211. Tateishi, K. *et al.* Extreme Vulnerability of IDH1 Mutant Cancers to NAD+ Depletion. *Cancer Cell* **28**, 773–784 (2015).

212. Elia, I., Schmieder, R., Christen, S. & Fendt, S. M. Organ-specific cancer metabolism and its potential for therapy. *Handb Exp Pharmacol* **233**, 321–353 (2016).

213. Ramtohul, Y. K. *et al.* SAR and optimization of thiazole analogs as potent stearoyl-CoA desaturase inhibitors. *Bioorg Med Chem Lett* **20**, 1593–1597 (2010).

214. Tardito, S. *et al.* Glutamine synthetase activity fuels nucleotide biosynthesis and supports growth of glutamine-restricted glioblastoma. (2015) doi:10.1038/ncb3272.

215. Fernández-García, J. & Fendt, S. M. Assessing the impact of the nutrient microenvironment on the metabolism of effector CD8+ T cells. *Methods in Molecular Biology* **1862**, 187–216 (2019).

216. Christen, S. *et al.* Breast Cancer-Derived Lung Metastases Show Increased Pyruvate Carboxylase-Dependent Anaplerosis. *Cell Rep* **17**, 837–848 (2016).

217. Lorendeau, D. *et al.* Dual loss of succinate dehydrogenase (SDH) and complex I activity is necessary to recapitulate the metabolic phenotype of SDH mutant tumors. *Metab Eng* **43**, 187–197 (2017).

218. Kharroubi, A. T., Masterson, T. M., Aldaghlas, T. A., Kennedy, K. A. & Kelleher, J. K. Isotopomer spectral analysis of triglyceride fatty acid synthesis in 3T3-L1 cells. *https://doi.org/10.1152/ajpendo.1992.263.4.E667* **263**, (1992).

219. Lipid Synthesis and Manufacture - Google Books. https://books.google.co.in/books?hl=en&lr=&id=4eCsP-jXMCYC&oi=fnd&pg=PA1&ots=1W-Iz_ZmzA&sig=aZU3sFGa7I8QiSNqXXUI__O2kGY&redir_esc=y#v=onepage&q&f=false.

220. Folch, J., Lees, M. & Sloane, G. H. *A SIMPLE METHOD FOR THE ISOLATION AND PURIFICATION OF TOTAL LIPIDES FROM ANIMAL TISSUES**.

221. Holub, B. J. & Skeaff, C. M. Nutritional regulation of cellular phosphatidylinositol. *Methods Enzymol* **141**, 234–244 (1987).

222. Hodson, L., Murray Skeaff, C., Wallace, A. J. & Arribas, G. L. B. Stability of plasma and erythrocyte fatty acid composition during cold storage. *Clinica Chimica Acta* **321**, 63–67 (2002).

223. Marien, E. *et al.* Non-small cell lung cancer is characterized by dramatic changes in phospholipid profiles. *Int J Cancer* **137**, 1539–1548 (2015).

224. Rysman, E. *et al.* De novo lipogenesis protects cancer cells from free radicals and chemotherapeutics by promoting membrane lipid saturation. *Cancer Res* **70**, 8117–8126 (2010).

225. Ekroos, K. *et al.* Charting molecular composition of phosphatidylcholines by fatty acid scanning and ion trap MS3 fragmentation. *J Lipid Res* **44**, 2181–2192 (2003).

226. Rentero, C., Magenau, A., Abu-Siniyeh, A., Owen, D. M. & Gaus, K. Quantitative imaging of membrane lipid order in cells and organisms. (2012) doi:10.1038/nprot.2011.419.

227. Prouty, S. M. & Pappas, A. Sapienic acid: Species-specific fatty acid metabolism of the human sebaceous gland. *Lipids and Skin Health* 139–157 (2015) doi:10.1007/978-3-319-09943-9_10/FIGURES/2.

228. Ge, L., Gordon, J. S., Hsuan, C., Stenn, K. & Prouty, S. M. Identification of the Δ-6 Desaturase of Human Sebaceous Glands: Expression and Enzyme Activity. *Journal of Investigative Dermatology* **120**, 707–714 (2003).

229. Fischer, E. & Sauer, U. Large-scale in vivo flux analysis shows rigidity and suboptimal performance of Bacillus subtilis metabolism. (2005) doi:10.1038/ng1555.

230. Zoeller, R. A. & Wood, R. The importance of the stearoyl-CoA desaturase system in octadecenoate metabolism in the Morris hepatoma 7288C. *Biochimica et Biophysica Acta (BBA) - Molecular Cell Research* **845**, 380–388 (1985).

231. Ackerman, D. & Simon, M. C. Hypoxia, lipids, and cancer: surviving the harsh tumor microenvironment. *Trends Cell Biol* **24**, 472–478 (2014).

232. Dall'Armi, C., Devereaux, K. A. & di Paolo, G. The role of lipids in the control of autophagy. *Current Biology* **23**, (2013).

233. Currie, E., Schulze, A., Zechner, R., Walther, T. C. & Farese, R. v. Cellular fatty acid metabolism and cancer. *Cell Metab* **18**, 153–161 (2013).

234. Stupp, R. & Roila, F. Malignant glioma: ESMO clinical recommendations for diagnosis, treatment and follow-up. *Annals of Oncology* **20**, (2009).

235. Zhang, J., F.G. Stevens, M. & D. Bradshaw, T. Temozolomide: mechanisms of action, repair and resistance. *Curr Mol Pharmacol* **5**, 102–114 (2012).

236. Ou, A., Alfred Yung, W. K. & Majd, N. Molecular mechanisms of treatment resistance in glioblastoma. *International Journal of Molecular Sciences* vol. 22 1–24 Preprint at https://doi.org/10.3390/ijms22010351 (2021).

237. Bergmann, N. *et al.* The Intratumoral Heterogeneity Reflects the Intertumoral Subtypes of Glioblastoma Multiforme: A Regional Immunohistochemistry Analysis. *Front Oncol* **10**, (2020).

238. Neftel, C. *et al.* An Integrative Model of Cellular States, Plasticity, and Genetics for Glioblastoma. *Cell* **178**, 835-849.e21 (2019).

239. Parker, J. J. *et al.* Intratumoral heterogeneity of endogenous tumor cell invasive behavior in human glioblastoma. *Sci Rep* **8**, (2018).

240. Varn, F. S. *et al.* Glioma progression is shaped by genetic evolution and microenvironment interactions. *Cell* **185**, 2184-2199.e16 (2022).

241. Kant, S. *et al.* Enhanced fatty acid oxidation provides glioblastoma cells metabolic plasticity to accommodate to its dynamic nutrient microenvironment. *Cell Death Dis* **11**, (2020).

242. Caniglia, J. L. *et al.* Beyond glucose: Alternative sources of energy in glioblastoma. *Theranostics* vol. 11 2048–2057 Preprint at https://doi.org/10.7150/thno.53506 (2021).

243. Cheng, X. *et al.* Targeting DGAT1 Ameliorates Glioblastoma by Increasing Fat Catabolism and Oxidative Stress. *Cell Metab* **32**, 229-242.e8 (2020).

244. Duman, C. *et al.* Acyl-CoA-Binding Protein Drives Glioblastoma Tumorigenesis by Sustaining Fatty Acid Oxidation. *Cell Metab* **30**, 274-289.e5 (2019).

245. Lewis, C. A. *et al.* SREBP maintains lipid biosynthesis and viability of cancer cells under lipid- and oxygen-deprived conditions and defines a gene signature associated with poor survival in glioblastoma multiforme. *Oncogene* **34**, 5128–5140 (2015).

246. Guo, D. *et al.* An LXR agonist promotes glioblastoma cell death through inhibition of an EGFR/AKT/ SREBP-1/LDLR-dependent pathway. *Cancer Discov* **1**, 442–456 (2011).

247. Guo, D., Hlavin Bell, E., Mischel, P. & Chakravarti, A. *Targeting SREBP-1-driven lipid metabolism to treat cancer*.

248. Wang, J. *et al.* Delta-6-desaturase inhibitor enhances radiation therapy in glioblastoma in vitro and in vivo. *Cancer Manag Res* **10**, 6779–6790 (2018).

249. Gimple, R. C., Bhargava, S., Dixit, D. & Rich, J. N. Glioblastoma stem cells: lessons from the tumor hierarchy in a lethal cancer. (2019) doi:10.1101/gad.324301.

250. Ferraro, G. B. *et al.* Fatty acid synthesis is required for breast cancer brain metastasis. *Nat Cancer* **2**, 414–428 (2021).

251. Hänzelmann, S., Castelo, R. & Guinney, J. *GSVA: gene set variation analysis for microarray and RNA-Seq data*. *BMC Bioinformatics* vol. 14 http://www.biomedcentral.com/1471-2105/14/7http://www.bioconductor.org.Background (2013).

252. Rossi, M. *et al.* PHGDH heterogeneity potentiates cancer cell dissemination and metastasis. *Nature* **605**, 747–753 (2022).

253. Pombo Antunes, A. R. *et al.* Single-cell profiling of myeloid cells in glioblastoma across species and disease stage reveals macrophage competition and specialization. *Nat Neurosci* **24**, 595–610 (2021).

254. Strickland, M. & Stoll, E. A. Metabolic reprogramming in glioma. *Frontiers in Cell and Developmental Biology* vol. 5 Preprint at https://doi.org/10.3389/fcell.2017.00043 (2017).

255. Bergles, D. E. *et al.* CNS myelination and remyelination depend on fatty acid synthesis by oligodendrocytes. (2019) doi:10.7554/eLife.44702.001.

256. Zhang, J., Stevens, M. F. G. & Bradshaw, T. D. *Temozolomide: Mechanisms of Action, Repair and Resistance*. *Current Molecular Pharmacology* vol. 5 (2012).

257. Mah, L. J., El-Osta, A. & Karagiannis, T. C. γh2AX: A sensitive molecular marker of DNA damage and repair. *Leukemia* vol. 24 679–686 Preprint at https://doi.org/10.1038/leu.2010.6 (2010).

258. Buescher, J. M. *et al.* A roadmap for interpreting 13C metabolite labeling patterns from cells. *Current Opinion in Biotechnology* vol. 34 189–201 Preprint at https://doi.org/10.1016/j.copbio.2015.02.003 (2015).

259. Wenzel, C. *et al.* 3D high-content screening for the identification of compounds that target cells in dormant tumor spheroid regions. *Exp Cell Res* **323**, 131–143 (2014).

260. Sato, T., Issa, J. P. J. & Kropf, P. DNA hypomethylating drugs in cancer therapy. *Cold Spring Harb Perspect Med* **7**, (2017).

261. Yasumoto, Y. *et al.* Inhibition of fatty acid synthase decreases expression of stemness markers in glioma stem cells. *PLoS One* **11**, (2016).

262. Grube, S. *et al.* Overexpression of fatty acid synthase in human gliomas correlates with the WHO tumor grade and inhibition with Orlistat reduces cell viability and triggers apoptosis. *J Neurooncol* **118**, 277–287 (2014).

263. Shakya, S. *et al.* Altered lipid metabolism marks glioblastoma stem and non-stem cells in separate tumor niches. doi:10.1101/2020.09.20.304964.

264. Korbecki, J. *et al.* Expression of SCD and FADS2 is lower in the necrotic core and growing tumor area than in the peritumoral area of glioblastoma multiforme. *Biomolecules* **10**, (2020).

265. Wu, Y. *et al.* Ferroptosis in Cancer Treatment: Another Way to Rome. *Frontiers in Oncology* vol. 10 Preprint at https://doi.org/10.3389/fonc.2020.571127 (2020).

266. Chen, Y. *et al.* Ferroptosis: A New Strategy for Cancer Therapy. *Frontiers in Oncology* vol. 12 Preprint at https://doi.org/10.3389/fonc.2022.830561 (2022).

267. Yang, W. S. *et al.* Peroxidation of polyunsaturated fatty acids by lipoxygenases drives ferroptosis. *Proc Natl Acad Sci U S A* **113**, E4966–E4975 (2016).

268. Li, D. & Li, Y. The interaction between ferroptosis and lipid metabolism in cancer. *Signal Transduction and Targeted Therapy* vol. 5 Preprint at https://doi.org/10.1038/s41392-020-00216-5 (2020).

269. Birzu, C. *et al.* Recurrent Glioblastoma: From Molecular Landscape to New Treatment Perspectives. (2020) doi:10.3390/cancers.

270. Schneider, M. *et al.* Newly diagnosed glioblastoma in geriatric (65 +) patients: impact of patients frailty, comorbidity burden and obesity on overall survival. *J Neurooncol* **149**, 421–427 (2020).

271. Valente Aguiar, P., Carvalho, B., Vaz, R. & Linhares, P. Body mass index as an independent prognostic factor in glioblastoma. *Cancer Causes and Control* **32**, 327–336 (2021).

272. Potharaju, M. *et al.* Body Mass Index as a Prognostic Marker in Glioblastoma Multiforme: A Clinical Outcome. *Int J Radiat Oncol Biol Phys* **102**, 204–209 (2018).

273. Cha, J. Y., Park, J. S., Hong, Y. K., Jeun, S. S. & Ahn, S. Impact of Body Mass Index on Survival Outcome in Patients with Newly Diagnosed Glioblastoma: A Retrospective Single-Center Study. *Integr Cancer Ther* **20**, (2021).

274. Weller, J. *et al.* Prognostic impact of obesity in newly-diagnosed glioblastoma: a secondary analysis of CeTeG/NOA-09 and GLARIUS. *J Neurooncol* (2022) doi:10.1007/s11060-022-04046-z.

275. Disney-Hogg, L. *et al.* Influence of obesity-related risk factors in the aetiology of glioma /631/67/68 /631/67/2324 article. *Br J Cancer* **118**, 1020–1027 (2018).

276. Woolf, E. C. & Scheck, A. C. The ketogenic diet for the treatment of malignant glioma. *Journal of Lipid Research* vol. 56 5–10 Preprint at https://doi.org/10.1194/jlr.R046797 (2015).

277. Esler, W. P. *et al.* Human sebum requires de novo lipogenesis, which is increased in acne vulgaris and suppressed by acetyl-CoA carboxylase inhibition. *Sci Transl Med* **11**, (2019).

278. Ge, L., Gordon, J. S., Hsuan, C., Stenn, K. & Prouty, S. M. Identification of the Δ-6 Desaturase of Human Sebaceous Glands: Expression and Enzyme Activity. *Journal of Investigative Dermatology* **120**, 707–714 (2003).

279. Young, R. S. E. *et al.* Apocryphal FADS2 activity promotes fatty acid diversification in cancer. *Cell Rep* **34**, (2021).

280. Lee, H. J. *et al.* Multimodal Metabolic Imaging Reveals Pigment Reduction and Lipid Accumulation in Metastatic Melanoma. *BME Front* **2021**, 1–17 (2021).

281. Kim, W. *et al.* Polyunsaturated Fatty Acid Desaturation Is a Mechanism for Glycolytic NAD + Recycling. *Cell Metab* **29**, 856-870.e7 (2019).

282. Currie, E., Schulze, A., Zechner, R., Walther, T. C. & Farese, R. v. Cellular fatty acid metabolism and cancer. *Cell Metab* **18**, 153–161 (2013).

283. Griffiths, B. *et al.* Sterol regulatory element binding protein-dependent regulation of lipid synthesis supports cell survival and tumor growth. *Cancer Metab* **1**, (2013).

284. Williams, K. J. *et al.* An essential requirement for the SCAP/SREBP signaling axis to protect cancer cells from lipotoxicity. *Cancer Res* **73**, 2850–2862 (2013).

285. Guo, D. *et al.* EGFR signaling through an Akt-SREBP-1-dependent, rapamycin-resistant pathway sensitizes glioblastomas to antilipogenic therapy. *Sci Signal* **2**, (2009).

286. Bruce, K. D., Zsombok, A. & Eckel, R. H. Lipid processing in the brain: A key regulator of systemic metabolism. *Front Endocrinol (Lausanne)* **8**, 60 (2017).

287. Lewis, C. A. *et al.* SREBP maintains lipid biosynthesis and viability of cancer cells under lipid- and oxygen-deprived conditions and defines a gene signature associated with poor survival in glioblastoma multiforme. *Oncogene 2015 34:40* **34**, 5128–5140 (2015).

288. Choo, M. *et al.* Involvement of cell shape and lipid metabolism in glioblastoma resistance to temozolomide. doi:10.1038/s41401-022-00984-6.

289. Guo, D., Bell, E. H., Mischel, P. & Chakravarti, A. Targeting SREBP-1-driven lipid metabolism to treat cancer. *Curr Pharm Des* **20**, 2619 (2014).

290. Key, T. J. *et al.* Diet, nutrition, and cancer risk: what do we know and what is the way forward? *The BMJ* **368**, (2020).

291. Mayne, S. T., Playdon, M. C. & Rock, C. L. Diet, nutrition, and cancer: past, present and future. *Nature Reviews Clinical Oncology 2016 13:8* **13**, 504–515 (2016).

292. Valente Aguiar, P., Carvalho, B., Vaz, R. & Linhares, P. Body mass index as an independent prognostic factor in glioblastoma. *Cancer Causes and Control* **32**, 327–336 (2021).

293. Jones, L. W. *et al.* Association between body mass index and mortality in patients with glioblastoma mutliforme. *Cancer Causes and Control* **21**, 2195–2201 (2010).

294. Maffeis, C. *et al.* Lipid and saturated fatty acids intake and cardiovascular risk factors of obese children and adolescents. *Eur J Clin Nutr* **75**, 1109–1117 (2021).

295. Ntambi, J. M. *et al. Loss of stearoyl-CoA desaturase-1 function protects mice against adiposity*. https://www.pnas.org.

296. Stoffel, W. *et al.* Obesity resistance and deregulation of lipogenesis in Δ6-fatty acid desaturase (FADS2) deficiency. *EMBO Rep* **15**, 110–120 (2014).

Addendum

This addendum shortly describes my research experience and the list of the studies to which I have contributed that are already published or in the course of publication.

Research experience:

2017-present: KU Leuven and VUB, Belgium

As a joint PhD student in the labs of Prof. Sarah-Maria Fendt and Prof. Jo Van Ginderachter, I currently:

- Study the role of fatty acid metabolism in cancer.
- Apply ^{13}C tracer techniques to investigate *de novo* fatty acid metabolism in cancers.
- Use metabolomics, molecular biology and cell biology techniques to address the effect of fatty acids in cancer therapies.

- Use *in vitro* techniques to investigate the metabolic requirements of CD8+ T-cells.

2014-2017: Mumbai, India

As an M.Sc student in the lab of Prof. Ullas Kolthur Seetharam at Tata Institute of Fundamental Research, Mumbai, India I:

- Used *Drosophila melanogaster* as a model system to identify the role of sirtuins in organismal physiology.
- Performed lifespan and healthspan analyses to address the role of Sirt4 in aging and health.
- Used molecular biology and cell biology techniques to identify the role of Sirt4 in cell signaling and physiology.

Fellowships:

- VIB international PhD fellowship 2017-2021

International meetings:

- **4th YPI Crete conference on Genes: Cell biology, cancer and beyond**.
  Heraklion, Crete, 2-6 October 2018.

  Title of talk: Tumor cell fatty acid metabolism governs T-cell population in the tumour microenvironment.

- **Keystone Symposium: Tumor Metabolism and the Microenvironment**
  Online, 25-28 January 2021

  Attendance and participation only.

- **Joint 1st ILS Conference - 7th Lipidomics Forum**
  Regensburg, Germany, 5-8 October 2021

  Title of talk: Intra-cellular heterogeneity of lipid metabolism in glioblastoma

Publications:

Articles

1. Pu-Ste Liu, Xiaoyun Li, Pei-Chun Hsueh, Sheue-Fen Tzeng, **Sweta Parik**, Sarah-Maria Fend, Ping-Chih Ho, **2022**,CD40 signal rewires fatty acid and glutamine metabolism for stimulating macrophage anti-tumorigenic functions. *Under revision in Nature Immunology.*
2. **Sweta Parik**, Juan Fernández-García, Francesca Lodi5 Karen De Vlaminck, Marleen Derweduwe, Steven De Vleeschouwer, Raf Sciot, Wietse Geens, Linqian Weng, Francesca Maria Bosisio, Gabriele Bergers, Johnny Duerinck, Frederick De Smet, Diether Lambrechts, Jo A. Van Ginderachter and Sarah-Maria Fendt, **2022**, GBM tumors are heterogeneous in their fatty acid metabolism and modulating fatty acid metabolism sensitizes cancer cells derived from recurring GBM tumors to temozolomide. *Frontiers in Oncology*, p.4708.
3. Juan Fernández-García, Fabien Franco, **Sweta Parik**, Antonino A. Pane, Dorien Broekaert, Joke van Elsen, Ines Vermeire, Thomas van Brussel, Rogier Schepers, Elodie Modave, Tobias K. Karakach, Peter Carmeliet, Diether Lambrechts, Ping-Chih Ho, View ORCID ProfileSarah-Maria Fendt, **2022**. CD8+ T- Cell Metabolic Rewiring Defined by Single-Cell RNA-Sequencing Identifies a Critical Role of ASNS Expression Dynamics in T-Cell Differentiation. *Accepted for publication in cell reports.*
4. Matteo Rossi, Patricia Altea-Manzano, Margherita Demicco, Ginevra Doglioni, Laura Bornes, Marina Fukano, Anke Vandekeere, Alejandro M. Cuadros, Juan Fernández-García, Carla Riera-Domingo, Cristina Jauset, Mélanie Planque, H. Furkan Alkan, David Nittner, Dongmei Zuo, Lindsay A. Broadfield, **Sweta Parik**, Antonino Alejandro Pane, Francesca Rizzollo, Gianmarco Rinaldi, Tao Zhang, Shao Thing Teoh, Arin B. Aurora, Panagiotis Karras, Ines Vermeire, Dorien Broekaert, Joke Van Elsen, Maximilian M. L. Knott, Martin F. Orth, Sofie Demeyer, Guy Eelen, Lacey E. Dobrolecki, Ayse Bassez, Thomas Van Brussel, Karl Sotlar, Michael T. Lewis, Harald Bartsch, Manfred Wuhrer, Peter van Veelen, Peter Carmeliet, Jan Cools, Sean J. Morrison, Jean-Christophe Marine, Diether Lambrechts, Massimiliano Mazzone, Gregory J. Hannon, Sophia Y. Lunt, Thomas G. P. Grünewald, Morag Park, Jacco van Rheenen & Sarah-Maria Fendt, **2022**. PHGDH heterogeneity potentiates cancer cell dissemination and metastasis. *Nature*, *605*(7911), pp.747-753.
5. Kim Vriens*, Stefan Christen*, **Sweta Parik**, Dorien Broekaert, Kazuaki Yoshinaga, Ali Talebi, Jonas Dehairs, Carmen Escalona-Noguero, Roberta Schmieder, Thomas Cornfield, Catriona Charlton, Laura Romero-Pérez, Matteo Rossi, Gianmarco Rinaldi, Martin F. Orth, Ruben Boon, Axelle Kerstens, Suet Ying Kwan, Brandon Faubert, Andrés Méndez-Lucas, Charlotte C. Kopitz, Ting Chen, Juan Fernandez-Garcia, João A. G. Duarte, Arndt A. Schmitz, Patrick Steigemann, Mustapha Najimi, Andrea Hägebarth, Jo A. Van Ginderachter, Etienne Sokal, Naohiro Gotoh, Kwok-Kin

Wong, Catherine Verfaillie, Rita Derua, Sebastian Munck, Mariia Yuneva, Laura Beretta, Ralph J. DeBerardinis, Johannes V. Swinnen, Leanne Hodson, David Cassiman, Chris Verslype, Sven Christian, Sylvia Grünewald, Thomas G. P. Grünewald & Sarah-Maria Fendt, **2019**. Evidence for an alternative fatty acid desaturation pathway increasing cancer plasticity. *Nature*, *566*(7744), pp.403-406. * These authors contributed equally.

6. **Sweta Parik**, Sandipan Tewary, Champakali Ayyub and Ullas Kolthur-Seetharam, **2018**. Loss of mitochondrial SIRT4 shortens lifespan and leads to a decline in physical activity. *Journal of biosciences*, *43*(2), pp.243-247.

Review

7. Ginevra Doglioni*, **Sweta Parik*** and Sarah-Maria Fendt, **2019**. Interactions in the (pre) metastatic niche support metastasis formation. *Frontiers in oncology*, *9*, p.219. * These authors contributed equally.